國立臺灣大學生命科學院生化科學研究所

博士論文

Graduate Institute of biochemical sciences

College of Life Science

National Taiwan University

Doctoral Dissertation

金屬蛋白的小分子活化與感應

Small Molecule Activation and Sensing by Metalloproteins

洪木成

Mu-Cheng Hung

指導教授：俞聖法 博士

共同指導教授：王彥士 博士

Advisor: Steve Sheng-Fa Yu, Ph.D.

Co-Advisor:Yane-Shih Wang, Ph.D.

中華民國 108 年 7 月

July, 2019

doi:10.6342/NTU201903909

誌謝

能完成這篇論文，我要特別感謝我的指導教授俞聖法老師在我低潮的時刻能適時地扶我一把。同時也感謝陳長謙院士在我遇到困難的時候，不辭辛勞地給我可能的方向。雖然在實驗室的時間，並非總是如意，大多時候人事的糾紛對我是總相當大的挑戰，但還是要感謝實驗室的每一位成員對我的支持與鼓勵，在實驗討論上或是實驗設計上的合作，讓實驗不至於裹足不前。這篇論文，包括了與實驗室同仁，如學弟張晉碩一起進行蛋白質的突變工作與設計、與實驗室同仁 Terra 在同步輻射中心測量樣品的分工與合作、同時在一氧化氮相關的專題，感謝過去博士同仁羅鳳君以及助理林立偉在實驗室中建立一套完全避絕氧氣的實驗方法。而關於實驗室管理上替大家分擔不少管理工作的張廷安、徐偉軒都使得實驗室的運作與氣氛變得相當適合研究。雖然在這個實驗室停留的時間相當久，但在這樣的實驗條件下，不僅僅是我也希望日後大家的實驗工作能不斷替突破難關，不僅面對科學問題，包括人事的難題也能迎刃而解。

doi:10.6342/NTU201903909

中文摘要

金屬蛋白的小分子活化和感應在自然界中可以有效地控制烷烴氧化或是感應一氧化氮。在這裡，我將展示了兩種模型，一種是甲烷單氧化酵素（pMMO），另一種是延胡索酸鹽和硝酸鹽還原調節蛋白（FNR）。

在第 1 部分中，我將研究嗜甲烷菌 *Methylococcus capsulatus*(Bath) (*M. capsulatus*) 甲烷單氧化酵素的 B 次單元（PmoB）的銅輔因子的數量跟特性。該蛋白體次單元對一價銅有相當高的親和力。為了闡述其銅親和力，我們設計全長的 PmoB 次單元、以及 N 端截斷的設計，包括 PmoB$_{33-414}$和 PmoB$_{55-414}$，以及麥芽糖結合蛋白（MBP）標籤轉殖並在大腸桿菌中大量表現。除了以 N 端截斷的方式觀察一價銅親和力，此外 Y374F、Y374S 和 M300L 突變蛋白也被建構。在培養過程，當大腸桿菌在 1.0mM Cu^{II}溶液大量表達 PmoB，甲烷單氧化酵素的 B 次單元表現得跟在甲烷菌中一樣。 在本實驗中，我們進一步收集這些 B 次單元的蛋白質，測量銅的數量、以 Cu Kα 邊緣 X 射線吸收近邊光譜（XANES）證實所有 PmoB 重組體都是一價銅蛋白。並根據 Cu 延伸的 X 射線吸收邊緣精細結構（EXAFS）的分析，發現 PmoB 蛋白顯示出「雙銅中心」的證據。當我們測量這些重組膜結合的 PmoB 蛋白發現並沒有甲烷和丙烯氧化的特定活性。然而其中的 PmoB$_{33-414}$蛋白卻可觀察到過氧化氫的顯著產生。此雙銅中心與氧氣反應產生過氧化氫的現象，會更近一步導致位於 PmoB 亞基的 C 末端亞結構域的一價銅的氧化。

在第 2 部分中，由於 FNR 蛋白是含有四鐵四硫金屬簇的轉錄因子，它的金屬

doi:10.6342/NTU201903909

簇化學結構對於氧氣與一氧化氮非常敏感。在我的研究中，試圖觀察大腸桿菌生理狀態從有氧呼吸轉換為厭氧硝酸鹽呼吸，即大腸桿菌的發酵生長，FNR 蛋白在生理條件下四鐵四硫金屬簇的變化。當大腸桿菌 BL21DE（PLyS）與含有 fnr 基因的轉化質體 pET22b 在厭氧條件以含有硝酸鹽的 LB 培養液中生長時，我們發現從 SDS-Page 分析中積累了大量的重組 FNR。同時發現重組 FNR 的表現量可以通過 Ni-NTA 柱層析容易地純化。將這些純化的 FNR 進行 EPR 測量。我們觀察到在 $g_{av} = 2.03$ 處出現強烈的順磁信號，這表示在蛋白質內形成雙亞硝基鐵複合物。同時從含有硝酸鹽的厭氧生長中分離的單元重組 FNR 單體的鐵含量為 2.42 個鐵。再加上我們確保在大腸桿菌體內 FNR 蛋白亞硝基化後形成 Roussin Red Ester（RRE），並且以二硫亞磺酸鈉還原觀察陰離子 Roussin Red Ester EPR 特徵（$g_{\perp} = 2.005$, $g_{\parallel} = 1.97$）。 並綜合 FNR 的基因調控和隨後在大腸桿菌中的蛋白質表達譜進一步證明了此亞硝化型態在硝酸鹽厭氧呼吸下於大腸桿菌中讓 FNR 獲得新的功能，構成了它正向的基因自動調節。

關鍵字：甲烷單氧化酵素；雙銅金屬簇；延胡索酸與硝酸還原調控蛋白；一氧化氮；硝酸鹽呼吸

doi:10.6342/NTU201903909

ABSTRACT

Small molecule activation and sensing by metalloproteins play important roles in controlled alkane oxidation or nitric oxide sensing in nature. Here, I show two protien systems, one is particulate methane monooxygenase (pMMO), the other is the fumerate and nitrate reduction regulator (FNR).

In part 1, we describe efforts to clarify the role of the copper cofactors associated with subunit B (PmoB) of the pMMO from *Methylococcus capsulatus* (Bath) (*M. capsulatus*). This subunit exhibits strong affinity toward Cu^{I} ions. To elucidate the high copper affinity of the subunit, the full-length PmoB, and the N-terminal truncated mutants PmoB$_{33–414}$ and PmoB$_{55–414}$, each fused to the maltose-binding protein (MBP), are cloned and over-expressed into *Escherichia* coli(*E. coli*) K12 TB1 cells. The Y374F, Y374S and M300L mutants of these protein constructs are also studied. When this *E. coli* grown with the pmoB gene in 1.0 mM Cu^{II}, it behaves like *M. capsulatus* (Bath) cultured under high copper stress with abundant membrane accumulation and high Cu^{I} content. The recombinant PmoB proteins are verified by Western blotting of antibodies directed against the MBP sub-domain in each of the copper-enriched PmoB proteins. Cu K-edge X-ray absorption near edge spectroscopy (XANES) of the copper ions confirms that all the PmoB recombinants are Cu^{I} proteins. All the PmoB proteins show evidence of a "dicopper site" according to analysis of the Cu extended X-ray absorption edge fine structure (EXAFS) of the membranes. No specific activities toward methane and propene oxidation are observed with the recombinant membrane-bound PmoB proteins. However, significant production of hydrogen peroxide is observed in the case of the PmoB$_{33–414}$mutant. Reaction of the dicopper site with dioxygen produces hydrogen peroxide and leads to oxidation of the Cu^{I} ions residing in the C-terminal sub-domain of the PmoB subunit

In part 2, FNR protein is a transcriptional factor containing 4Fe-4S cluster, which is sensitive to the presence of dioxygen molecules and can switch the physiological status from aerobic respiration to anaerobic nitrate respiration, i.e., the fermentated growth of *E. coli*. When *E. coli* BL21DE (PLyS) grown with transformed plasmid pET22b containing *fnr* gene insert in anaerobic conditions by the presence of the nitrate salts in LB buffer, significant amounts of recombinant FNR are accumulated from the SDS-Page analysis. The recombinant FNR with poly-histidine can be easily purified through Ni-NTA column chromatography. The FNR is subjected for EPR measurement. A strong paramagnetic signal appeared at g_{av} = 2.03 indicates the formation of iron dinitrosylated complexes within the proteins. The iron contents of unit recombinant FNR monomer isolated from the anaerobic growth with the nitrate salts was 2.42. We ensure that there is formation of Roussin’s Red ester (RRE) after the nitrosylation of FNR protein *in vivo* with the further reduction mediated by dithionites for the observation of EPR characteristic ($g_{\perp}$ = 2.005, $g_{\parallel}$ = 1.97) of anionic Roussin’s Red ester. The gene regulation of FNR and subsequent protein expression profiling in *E. coli* have further indicated that nitrosylated FNR in *E. coli* under anaerobic respiratory are auto-regulated.

Keywords：Pmmo, dicopper cluster, FNR, nitric oxide, nitrate respiratory

CONTENTS

doi:10.6342/NTU201903909

doi:10.6342/NTU201903909

doi:10.6342/NTU201903909

LIST OF FIGURES

doi:10.6342/NTU201903909

LIST OF TABLES

doi:10.6342/NTU201903909

Chapter 1 Introduction

1.1 The importance of biological methane oxidation

The development of catalysts for efficient conversion of methane to methanol has been receiving increasing attention currently with the search for alternative fuels to replace the dwindling supply of petroleum.[1, 2] People want to find approaches to utilize methane well. The traditional way to form methanol usually comes from the syngas synthesis. The conventional way to form syngas depicted in reaction 1.[3] The syngas comes from the steam reforming of CH_4 (reaction 2). At this juncture, no method has been discovered to convert CH_4 into CH_3OH directly with dioxygen (O_2) on an industrial scale (reaction 3). The direct oxidation of CH_4 to CH_3OH without overoxidation is a though dream. The problems are both kinetic and thermodynamic. First, the C—H bonds of CH_4 are extremely inert because of their high bond dissociation energies (104 kcal mol^{-1}). Moreover, the ground state of O_2 is a triplet $^3\Sigma$ state, and the direct reaction of triplet O_2 with singlet CH_4 to form singlet CH_3OH is a spin-forbidden process. In the thermodynamic perspective , whereas reaction 3 proceeds with spontaneity and with a substantial release of heat, but the further oxidations of CH_3OH to formaldehyde (H_2CO), formic acid (HCOOH), and CO_2 are more exergonic and more exothermic (Fig.1). Thus, the product CH_3OH is prone to further oxidation to H_2CO and HCOOH. On the basis of these considerations, it follows that substantial energy input, for example, high temperatures, is required to activate the reaction and the selective oxidation of CH_4 to CH_3OH is difficult to control. Also, the pKa value of CH_4 is very high, precluding direct activation of the C—H bond by ionization through conventional acid–base chemistry under ambient

doi:10.6342/NTU201903909

conditions. With a negligible electron affinity and four strong C—H bonds, redox and radical reactions are also very difficult. Therefore, the oxygenation of CH_4 under ambient conditions has long been considered one of the holy grail of organic chemistry.[4]

$$CO(g) + 2H_2(g) \xrightarrow{Cu/ZnO/Al_2O_3} CH_3OH(g) \quad \Delta H_{298} = -21.7\ \text{kcal mol}^{-1} \tag{1}$$

$$CH_4(g) + H_2O(g) \overset{Ni}{\rightarrow} CO(g) + 3H_2(g) \quad \Delta H_{298} = 49.3\ \text{kcal mol}^{-1} \tag{2}$$

$$CH_4(g) + 1/2O_2(g) \rightarrow CH_3OH(l) \quad \Delta H_{298} = -39.2\ \text{kcal mol}^{-1} \tag{3}$$

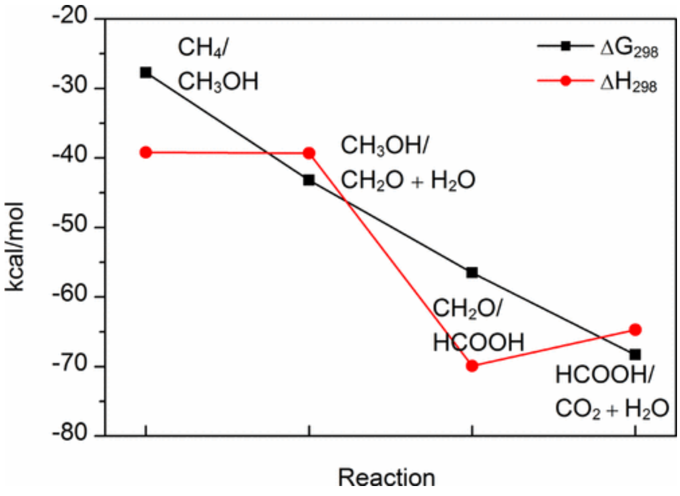

Fig. 1 Values of the free energy (ΔG) and the enthalpy (ΔH) for each step of the oxidation reactions of CH_4 to CO_2 by O_2. The values are given at a temperature of 298 K.[3]

Although the controlled oxidation of methane to methanol is challenging, the methane monooxygenases from methanotrophs, however designed by the nature, are known to mediate the facile conversion of methane to methanol with high efficiency under ambient temperature and pressures. There are two of these enzymes, the iron-containing soluble methane monooxygenase (sMMO) and the membrane-bound copper-containing particulate methane monooxygenase (pMMO).[5-8] With a turnover frequency approaching one methane molecule per second per enzyme in the cellular intra-cytoplasmic membranes, the pMMO is the most efficient methane oxidizer discovered to date. It is unique in its ability to mediate the oxidation of methane to methanol with unprecedented regio-specificity and stereo-selectivity.

Moreover, methane is a greenhouse gas; its global warming potential is more than 20 times that of carbon dioxide.[9] In nature, methanotrophs play a critical, ecological role in the global carbon cycle since they are the only biological methane sink.[9] Understanding the molecular mechanism of how these enzymes function, therefore, has been a fascinating and significant goal of many bio-chemists in searching for a new way to design "greener" catalysts to perform this important chemistry.[6, 10]

1.2 The particulate methane monooxygenase (pMMO): gene information

The oxidation of methane to methanol, the first step in the metabolic pathway of methanotrophs (**Fig.2**), is mediated by the methane monooxygenases (MMOs). The MMO enzyme systems utilize the reducing power of NADH to split the O-O bond of dioxygen and then transfer one oxygen atom to a hydrocarbon substrate while the other is reduced to H_2O.[6] In two types of MMOs, sMMO is produced in the water-soluble form but the pMMO is an intracytoplasmic transmembrane enzyme which is known as the better methane oxidizer.[5, 6] The substrate range of the two MMO systems is discrepant. pMMO only hydroxylates straight-chain hydrocarbons

doi:10.6342/NTU201903909

from C1-C5 and epoxidizes related alkenes, but not aromatic compounds, the alicyclic hydrocarbon cyclohexane or the branched aliphatic 2-methylpropane, all of which sMMO can harness.[11, 12] While the structure, biochemistry, and mechanism of sMMO are more understood,[13] the catalytic site and the mechanism of methane oxidation in pMMO are still under controversy.[6, 10, 14, 15]

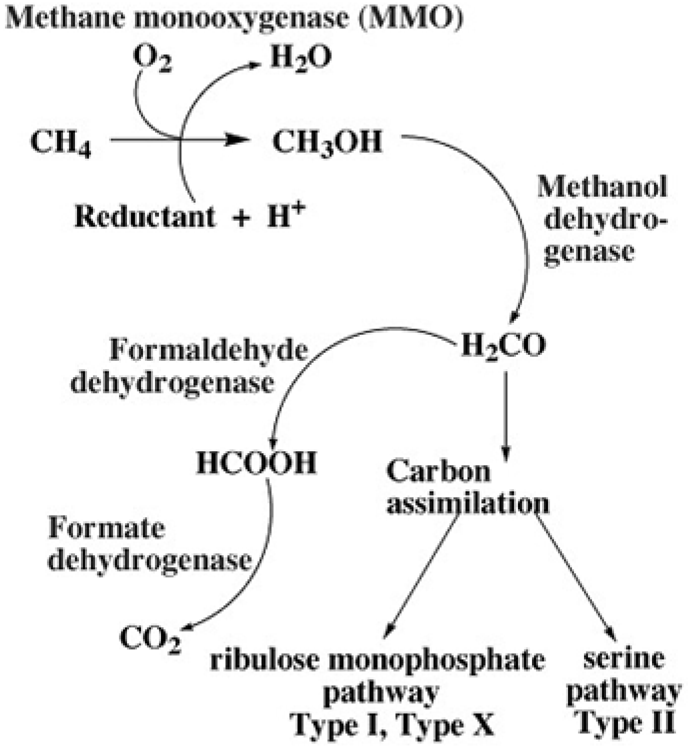

Fig. 2 The metabolic pathway of methanotrophs.[3]

The two proteins sMMO and pMMO are products of different genes. In more than 130 methanotrophs,[16] all produce pMMO but only seven of them are found to produce both sMMO/pMMO. Interestingly, the expression level of two enzymes is controlled and regulated by the concentration of copper ions in the growth environment. In *Methylococcus capsulatus* (Bath), for example, sMMO is exclusively produced when the copper concentration is limiting and the bacterium switches to overproduce pMMO at copper ion level in the growth medium $> 5\ \mu$M.[17, 18] A model for switching between expression of the sMMO and pMMO in *Methylosinus trichosporium* OB3[17] has been proposed as illustrated in **Fig.3**.

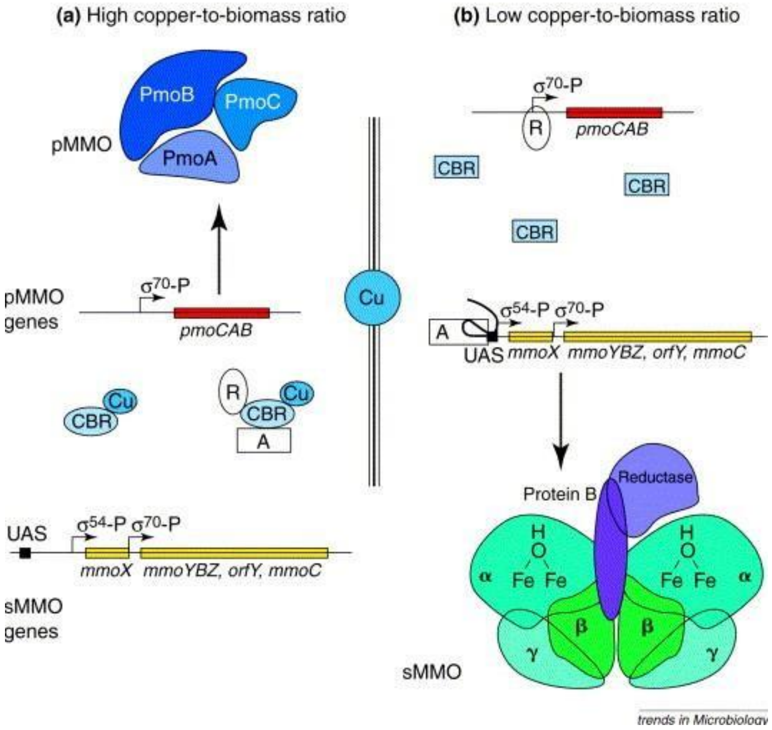

Fig. 3 Model for the reciprocal regulation of the genes encoding pMMO and sMMO in *Methylosinus trichosporium* OB3b.[17] **(a)** In cells growing under high copper-to-biomass ratios pMMO is derepressed and the hypothetical repressor molecule (R) is bound by a hypothetical copper-binding regulator (CBR). This CBR–Cu complex also binds to the hypothetical activator (A). **(b)** Under low copper-to-biomass conditions, the CBR does not bind copper and thus transcription of the *pmo* genes is repressed. The free activator protein (A) can then bind to the upstream activating sequence (UAS) of *mmoX*, enabling RNA polymerase to form an open complex and transcribe the sMMO-encoding genes.

The genes for pMMO are organized in the pmoCAB operon encoding for three distinct subunits pmoB or α (～ 46 kDa), pmoA or β (～ 28 kDa), and pmoC or γ (~29 kDa), respectively.[19, 20] In some bacteria such as *M. capsulatus* (Bath),[18] *M. trichosporium* OB3b, and *Methylocystis* sp. strain *M*,[21] there are two nearly identical copies of pmoCAB. A third copy of pmoC is only found in *M.capsulatus* (Bath)[22] and this sequence of this pmoC differs from those of the other two copies. The genes encoding ammonia monooxygenase (AMO)[23] are homologues to the pMMO's genes. Gene disruption experiments using *M.capsulatus* (Bath) have showed that the two pmoCAB genes are functional and necessary for the maximal activity of pMMO complex. The third pmoC gene has been suggested to be essential for the cell to grow on methane,[22] indicating its important role in the catalytic mechanism of methane oxidation.

1.3 Three dimensional structures of pMMO and their functional implications

The first crystal structure of pMMO complex was determined in 2005 at 2.8 Å resolution from M. *capsulatus* (Bath).[24] (**Fig.4**) Following this seminal work, there have appeared crystal structures of the M. *trichosporium* OB3b pMMO to 3.9 Å resolution,[25] the *Methylocystis* sp. strain M pMMO to 2.68 Å resolution,[26] and a revised structure of *M.capsulatus* (Bath) pMMO.[27] According to these studies, the pMMOs from all those three bacteria strains crystallize as a trimer of αβγ monomers with three identical copies each of the PmoB, PmoC, and PmoA subunits. Every monomer has a molecular weight of approximately 100 kDa. The PmoA and PmoC are primarily composed of transmembrane helices. The PmoB subunit consists of

doi:10.6342/NTU201903909

two water-soluble domains at both N-terminus and C-terminus connected by two transmembrane helices and a long linker region.

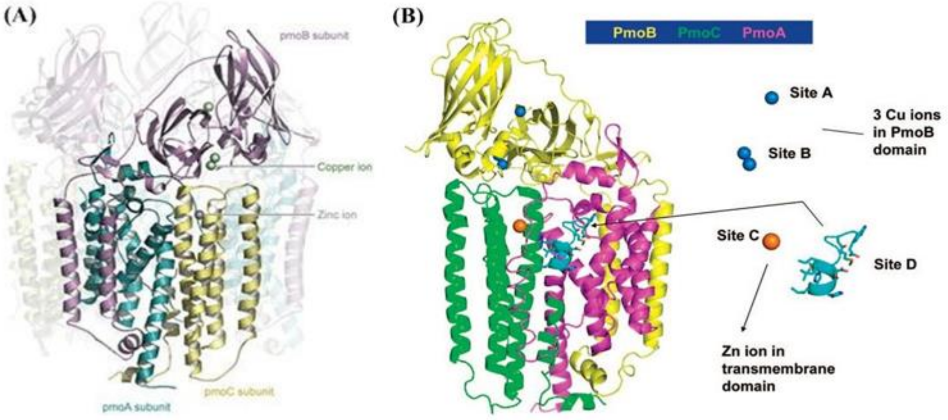

Fig. 4 (**A**) The first crystal structure of pMMO from *M.capsulatus* (Bath) [Protein Data Bank (PDB) code 1YEW] with one monomer highlighted[27]; and (**B**) Assignment of metal centers in the pMMO crystal structure according to their location[5].

Some metal centers have been observed from these crystal structures.[9] Based on the nature of metal ions and the number of metal ion(s) at each site, they are divided into three groups respectively as PmoB dicopper site, PmoB monocopper site, and PmoC “zinc” site. It is noted that these metal centers are not consistent between the crystal structures from the three bacteria strains, indicating the loss or exchange of metal ions during the purification and/or crystallization of pMMOs. In *M.capsulatus* (Bath) for example, the PmoB dicopper site is found in all three monomers while it is observed as monocopper in two monomers from the crystal structures of the *M. trichosporium* OB3b pMMO and the *Methylocystis* sp. strain M pMMO. The monocoper site in PmoB observed in *M.capsulatus* (Bath) pMMO does not contain any copper in the other two crystal structures. Besides, the “zinc” site is found in both pMMO crystal structures from *M. capsulatus* (Bath) and the *Methylocystis sp*. strain M but it is a “copper” site in the case of the *M. trichosporium* OB3b pMMO. Authors of these crystal structures have also admitted that there must be exchange of zinc for copper ions at the “zinc” site during crystallization process.[10] The crystals are obtained from purified pMMO suspended in concentrated $ZnSO_4$ buffers. Details on the comparison between the similarities and differences on these metal centers as well as ligands of each metal ion are cited from reference[10] as illustrated in **Fig.5**.

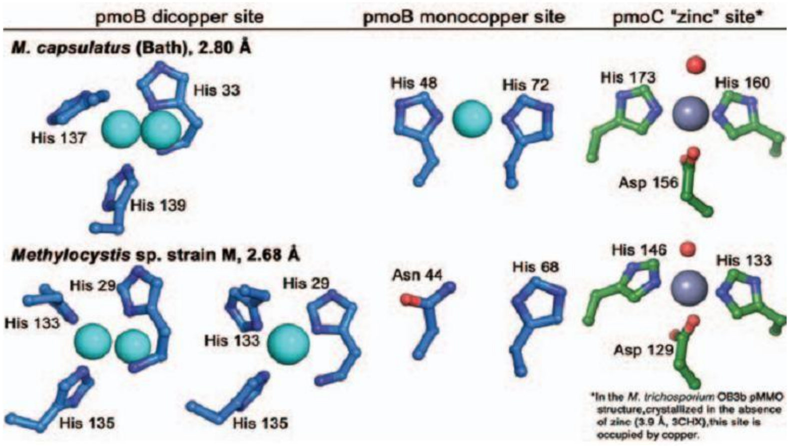

Fig. 5 Metal centers modeled in the pMMO crystal structures. [10] The PmoB site modeled as a dicopper center in the *M. capsulatus* (Bath) pMMO structure is modeled as a dicopper center in one protomer and monocopper in two protomers in the *Methylocystissp*. strain M pMMO structure. The monocopper site in PmoB from *M. capsulatus* (Bath) pMMO does not contain copper in the other pMMO structures. In both structures, zinc is found in the transmembrane site as a result of including zinc in the crystallization buffer. However, copper occupies this site in *M. trichosporium OB3b* pMMO.

doi:10.6342/NTU201903909

In addition to the observed metal centers in the crystal structures, there is a hydrophilic cluster of potential metal-ligating residues revealed by the structural information. This cluster, referred to as the D site in the protein (**Fig.4**), contains many hydrophilic amino acid residues including His38, Met42, Met45, Asp47, Trp48, Asp48, and Glu100 from PmoA and Glu154 from PmoC. Because the electrostatic energy of sustaining this cavity would be extremely high without counter-ions to balance the negative charge of these residues, the Chan group surmised that metal ions must be present at this site. During the harsh and aerobic conditions of the purification of the protein for crystallographic analysis, these metal ions must have been stripped away. Based on a series of studies, Chan and coworkers have proposed that the D site contains a tricopper cluster which serves as the catalytic site of the enzyme.[6]

1.4 The quest for the catalytic sites and mechanism of C-H bond activation in pMMO

The obtaining of crystal structures of pMMO is a significant step toward understanding the relationship between protein structure and function. Unfortunately, the accumulation of the structures seems to make the current assignment of metal centers in pMMO by the X-ray crystal structures increasingly ambiguous, if not confusing. As mentioned above in the previous section, the inconsistency in both the number of coppers in the PmoB dicopper site and PmoB monocopper site and the type of metal ion(s) at the PmoC “zinc” site from three crystal structures indicates that the observed metal centers does not reflect all the metal cofactors existing within the intact

doi:10.6342/NTU201903909

pMMO complex. In fact, the functional intact pMMO or the membrane-bound pMMO from *Methylococus capsulatus* (Bath) consists of 12-15 copper ions per 100 kDa monomer whereas there are just three of them remaining in the purified protein for crystallization.[6, 10, 24-31]. There is thus undoubtedly about the loss of copper cofactors during the purification and/or crystallization of the enzyme, particularly pMMO from *Methylococus capsulatus* (Bath). In other words, the X-ray crystal structures do not contain all the metal cofactors, one of which might be the catalytic site of the enzyme. In addition, a biomimetic inorganic complex based on a putative tricopper cluster in the pMMO has been recently shown to mediate the efficient oxidation of many hydrocarbons, including methane, at room temperature.[32-35] However, the location of the catalytic site of the enzyme as well as the mechanism of methane oxidation is still under controversy,[6, 10, 11, 14, 15, 35] despite almost 30 years of research and the availability of several crystal structures.[24-26]

Basically, three models have been proposed for the active site and the mechanism of methane oxidation at the catalytic site of pMMO. Interestingly, the contents of the proposed models are radically different, both in the location of the enzyme catalytic site and the nature and composition of the metal cofactor. Two models proposed by the Chan group and the Rosenzweig group conclude copper ions at the active site, whereas another research group believes in a nonheme di-iron center at the catalytic site. The iron model is proposed most recently in the year of 2007. On the basis of a Mössbauer study, the authors suggested a nonheme diiron center as the active site of *M.capsulatus* (Bath) pMMO.[14] According to this study, a diiron center similar to that in sMMO was proposed to be present in pMMO at the PmoC “zinc” site of pMMO crystal structures. They have also suggested that the purified pMMO might

doi:10.6342/NTU201903909

contain this diiron center with 10% occupancy. However, the content of Fe corresponds to the Cu/Fe content determined for the purified protein-detergent micelles reported from the Chan laboratory, for which the copper ions have been shown to support redox, dioxygen, and oxo-transfer chemistry. The turnover of the copper ions depends on the presence of hydrocarbon substrate, so a subset of the coppers must be involved in the oxidation of the substrate.[5] Factually, there is now a general consensus among most researchers that pMMO is a multicopper enzyme.[6, 8, 15]

On the basis of the crystal structures, it has been argued that the active site of the enzyme resides in PmoB. A soluble fragment of this subunit containing the dinuclear copper center at site B has been prepared and shown to be capable of oxidizing methane to methanol, albeit with low activity.[15, 25] This second model is proposed by the Rosenzweig research group from the Northwestern Univeristy, the author of the above crystal structures. According to this model, two copper ions in the active site are coordinated by His 33, His 137, and H139, all from the soluble part of PmoB subunit. EXAFS data for their purified pMMOs indicate the presence of a short Cu-Cu interaction at ~ 2.5Å and ~2.6Å upon chemical reduction.[10] However, the nuclearity of the dicopper site have not been established definitively due to the limited resolution in the crystal structures and quantum calculation.[10] The observations of monocopper occupancy at the dicopper site in some subunits of the *Methylocystis* sp. Strain pMMO[26] as well as the inconsistency in the copper stoichiometry between purified protein and crystallized protein[10] have also added confusion over the nuclearity. The only visible ligands, three histidine side chains and the amino terminus of PmoB, actually provide good evidence for the existence of the dicopper site. It is also leaving open the question of whether exogenous bridging or other

doi:10.6342/NTU201903909

terminal ligands might be present.

One key experiment, which has led to the suggestion that each active pMMO monomer contains just 2-3 coppers and the methane oxidation is mediated by the PmoB dicopper site, is the recovery of membrane-bound pMMO activity upon addition of 2-3 equivalents of copper to the cyanide-mediated metal removing protein. By contrast, iron addition has no effect on pMMO activity.[15] Assuming the experiment was conducted properly, this result thus conflicts with some measurements of the metal content in the same protein samples where 12-15 coppers are identified for each one 100 kDa pMMO promoter,[6, 10, 28, 29] especially including the data from the authors on pMMO from *M.capsulatus* (Bath) (**Table 1**).[10] It is also necessary to note that the membrane-bound pMMOs used for the activity recovering experiment were prepared aerobically, the condition prone for oxidation of the Cu ions and subsequent dissociation of the copper (II) ions from the protein. To pinpoint the catalytic site location or the ligands of the dicopper site, they have prepared constructs corresponding to the two soluble N-terminal and C-terminal domains of the *M.capsulatus* (Bath) PmoB subunit and evaluated the effects of some mutations on them. Three recombinant proteins spmoBd1 (PmoB N-terminus only), spmoBd2 (C-terminus only), and spmoB (in which the two terminal proteins are connected by a synthetic liker) have been overexpressed in E.*coli* cells as inclusion bodies. The methane oxidation and propylene epoxidation assays detected some activity with both spmoBd1 and spmoB, but not with spmoBd2. But the obtained methane oxidation activity is about 10% of that of intact membrane-bound pMMO,[15] which is in turn also just 10% of whole cell activity.[14] In addition, the activity assays performed on these recombinant proteins used very high concentrations of reducing reagent, at

doi:10.6342/NTU201903909

0.9-1.1 M duroquinol.[14] Although control experiments have been claimed to eliminate the effect of the free reducing power, it is not sure that whether the radicals that are formed easily under these conditions would introduce artifacts or not. Mutagenesis on the ligands of both the mono and dicopper sites of PmoB has also been done to examine their effects on the activity of spmoB and spmoBd1. The disruption of mononuclear site by smpoB_H48N mutation does not abolish the enzymatic activity. In contrast, methane activity is reduced significantly in variants (spmoB_H137, 139A or both spmoB_H48N and H137, 139A) that interferes with the dicopper site. Based on these mutagenesis studies, Rosenzweig and coworkers suggested that the active site of pMMO is the crystallographically modeled dicopper site.

Table 1 Copper content and enzyme activity of pMMOs and soluble PmoB fragments.[10]

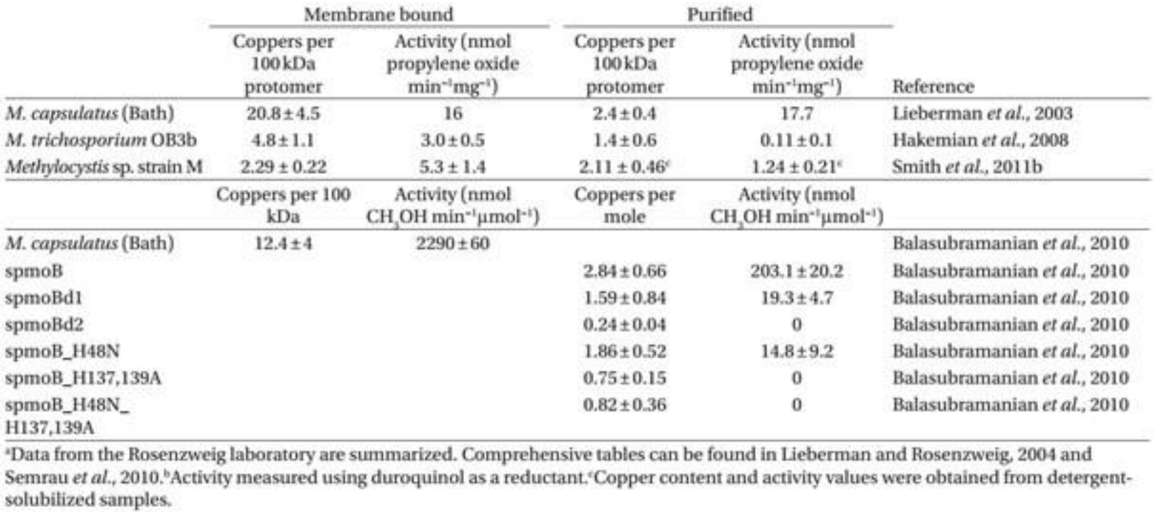

	Membrane bound		Purified		
	Coppers per 100 kDa protomer	Activity (nmol propylene oxide min^{-1}mg^{-1})	Coppers per 100 kDa protomer	Activity (nmol propylene oxide min^{-1}mg^{-1})	Reference
M. capsulatus (Bath)	20.8 ± 4.5	16	2.4 ± 0.4	17.7	Lieberman *et al.*, 2003
M. trichosporium OB3b	4.8 ± 1.1	3.0 ± 0.5	1.4 ± 0.6	0.11 ± 0.1	Hakemian *et al.*, 2008
Methylocystis sp. strain M	2.29 ± 0.22	5.3 ± 1.4	2.11 ± 0.46^{c}	1.24 ± 0.21^{c}	Smith *et al.*, 2011b
	Coppers per 100 kDa	Activity (nmol CH_3OH min^{-1}µmol^{-1})	Coppers per mole	Activity (nmol CH_3OH min^{-1}µmol^{-1})	
M. capsulatus (Bath)	12.4 ± 4	2290 ± 60			Balasubramanian *et al.*, 2010
spmoB			2.84 ± 0.66	203.1 ± 20.2	Balasubramanian *et al.*, 2010
spmoBd1			1.59 ± 0.84	19.3 ± 4.7	Balasubramanian *et al.*, 2010
spmoBd2			0.24 ± 0.04	0	Balasubramanian *et al.*, 2010
spmoB_H48N			1.86 ± 0.52	14.8 ± 9.2	Balasubramanian *et al.*, 2010
spmoB_H137,139A			0.75 ± 0.15	0	Balasubramanian *et al.*, 2010
spmoB_H48N_ H137,139A			0.82 ± 0.36	0	Balasubramanian *et al.*, 2010

[a] Data from the Rosenzweig laboratory are summarized. Comprehensive tables can be found in Lieberman and Rosenzweig, 2004 and Semrau *et al.*, 2010. [b] Activity measured using duroquinol as a reductant. [c] Copper content and activity values were obtained from detergent-solubilized samples.

More recently the research group has also suggested that they have observed O_2 binding at their proposed active site.[35] The binding of dioxygen to the PmoB dicopper center results in the formation of an optical feature at 345nm. In summary, on the basic of the crystal information and mutagenesis studies, Amy C. Rosenzweig and coauthors have suggested that the PmoB dicopper site is the catalytic site of pMMO. Unfortunately, all of their protein preparations have low methane oxidation activity. Moreover, many aspects of this model remain elusive such as the potential loss of metal cofactors, the nuclearity of the dicopper site, function of the other two transmembrane subunits in the enzymatic mechanism, and the interpretation of suicide substrate acetylene binding data in the context of the structural or other biochemical data.

The last model that I will summarize next is proposed by Chan and coworkers.[5, 10] According to the model, a tricopper cluster at the site D of pMMO (**Fig.4**) serves as the catalytic site, and reducing equivalents or electrons for enzymatic turnover are supplied from the C-terminal domain of PmoB through the dicopper center at site B. Beyond the two models discussed above, this laboratory has recently synthesized a series of catalysts inspired by their understanding of the pMMO’s catalytic site, in which some of the novel catalysts can indeed mediate the facile methane oxidation and propylene epoxidation under ambient conditions.[33] The proposal is also considered as the most complete one so far, the followings are its important milestones.

First, on the basis of electron magnetic resonance (EPR) spectroscopy, the existence of trinuclear copper centers in pMMO from *M. capsulatus* (Bath) was first suggested by Nguyen et al., 1996.[36] Although not observed in any crystal structures, repeated and increasing spectroscopic evidences have reinforced the idea for the presence of at least one tri-copper cluster in highly active pMMO, where it serves as the critical hydroxylation site.[6, 11, 37] Most obviously, the isotropic EPR signal attributed to the $Cu^{II}Cu^{II}Cu^{II}$ cluster was resolved from the type 2 copper signal by redox potentiometry EPR[37](**Fig.6**). For comparison, the essentially identical EPR signals have also been observed with the synthesized trinuclear CuIICuIICuII complexes,[38] especially with the tricopper peptide cluster derived from pMMO.[33]

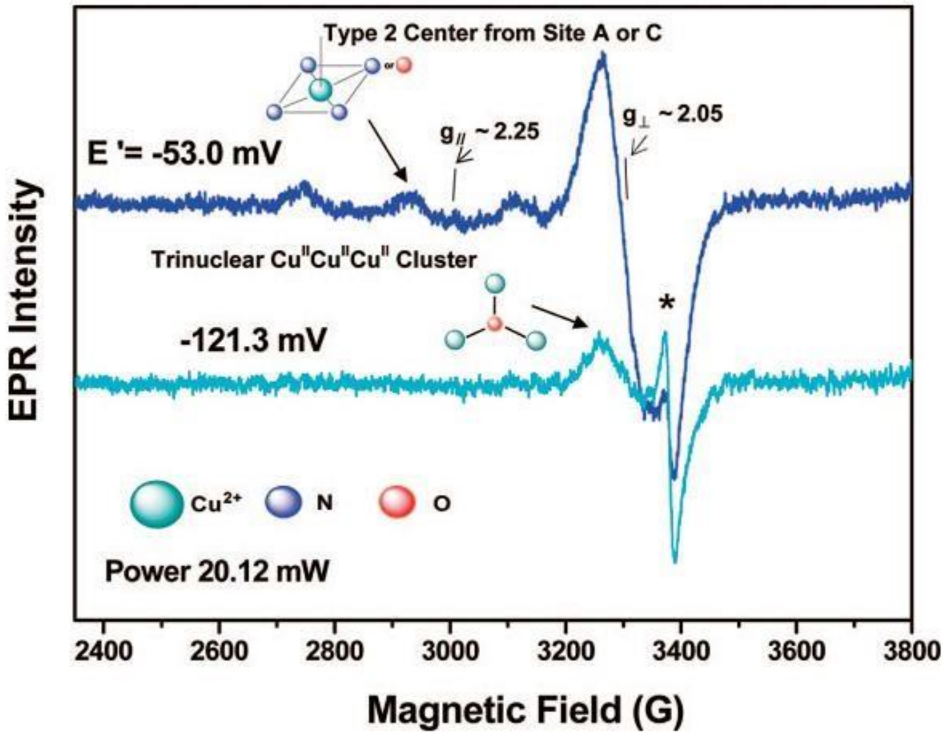

Fig. 6 Redox potentiometry EPR titration of the C-cluster copper ions.[38] Asterisks in the spectra at g≈2.002 denote signals originating from free radicals associated with the dithionite and the redox mediators.

Also on the basic of EPR studies, the Chan group has divided copper centers into two groups.[6] Out of 14-15 coppers, six of them that are readily oxidized by dioxygen in the absence of substrate have been referred as catalytic clusters (C-clusters). And a second group of *ca.* nine coppers that remain reduced (Cu(I)) under these conditions has been proposed to provide a reservoir of reducing equivalents to re-reduce the copper ions at the active site after the oxidative phase of the turnover, referred to as

E-clusters. In support for the existence of these Cu(I) clusters or E-clusters Yu *el al.*, have cloned and overexpressed both C-terminal and N-terminal domains of PmoB in E.*coli* and have observed the binding of about 10 Cu(I) ions to the purified C-terminal subdomain.[39] It is however noted that the Rosenzweig group could not repeat the experiment.[15] Returning to the six coppers in the C-cluster; it was originally proposed that they were organized into two trinuclear copper clusters[11, 36, 40] based on the observations of the spins within each triad copper cluster coupled ferromagnetically. Accordingly, a model was developed for the catalytic machinery of pMMO, wherein one tricopper cluster can support both dioxygen chemistry and substrate oxidation and the other dioxygen chemistry only[6] (**Fig.6**).

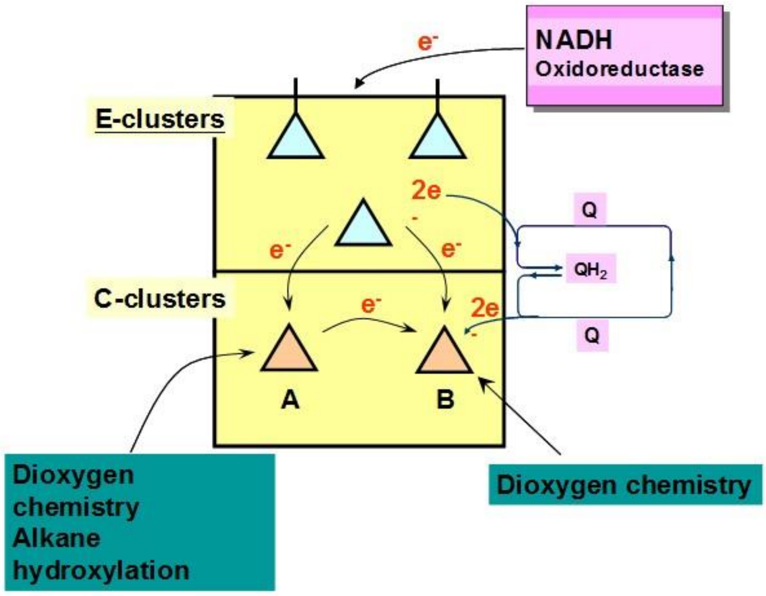

Fig. 7 Schematic of pMMO illustrating the two C-clusters and the three E-clusters, their locations vis-a`-vis the membrane, and their functions. Also shown are the putative electron input site(s) for NADH, and a possible site for electron input from plastoquinols, as well as the pathways of electron transfer within the enzyme.[11]

The second milestone in the development of the tricopper model is the identification of the location of the catalytic site in pMMO. In order to reconstruct three copper ions into the site D of the crystal structure[24] of *M. capsulatus* (Bath), Chan and coworkers used a computational approach. The modeling process of a trinuclear $Cu^{II}Cu^{II}Cu^{II}$ cluster into this site take into account favorable side-chain rotamers, potential hydrogen-bonding interactions, and the metal–ligand bond and the optimization of the geometry between the residues and metal ions of the modeled trinuclear copper site[37] (**Fig.8**). The coordinated ligands and the geometry of the cluster, including the Cu–Cu and Cu–O distances, are all reasonable and demonstrate the feasibility of the MMO protein to accommodate a trinuclear copper cluster. The trinuclear $Cu^{II}Cu^{II}Cu^{II}$ structure modeled here corresponds to that of the fully oxidized cluster after turnover by dioxygen in the absence of alkane.[11]

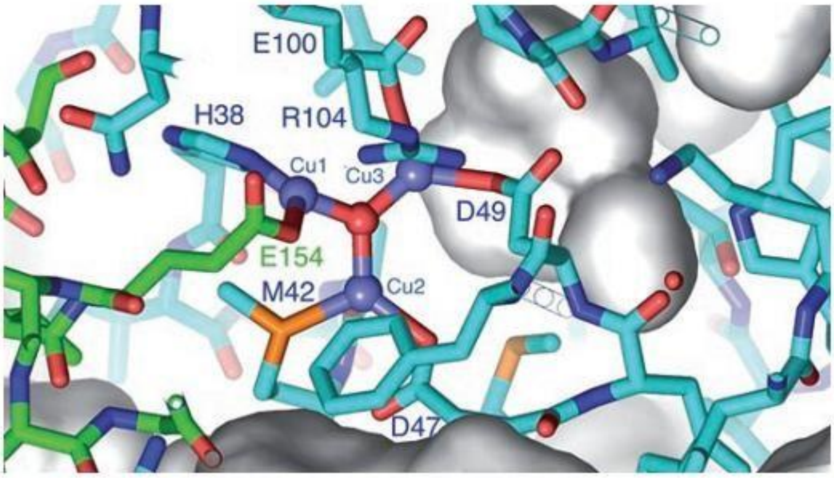

Fig. 8 Trinuclear copper site modeled into the putative cavity. The ligands to the copper atoms in this model are as follows: PmoC Glu154 and PmoA His38 for Cu1; PmoA Met42 and Asp47 for Cu2; and PmoA Asp49 and Glu100 for Cu3. The carbonyl group of PmoA Ala41 refines to a position where it can also bind Cu^{2+}. The carbon atoms of the PmoA subunit are colored in cyan, and those of the PmoC subunit are shown in green. The remaining atoms are colored in CPK. The putative methane-binding channel lies to the upper right.

In support for the catalytic site at the modeled tricopper site in pMMO, a substrate binding pocket and the hydroxylation chemistry at this site have been delineated accordingly.[41] In the sMMO system, experiments with chiral alkanes have provided insight into the catalytic mechanism at its active site.[42] Basically, the chiral alkane substrates were used as mechanistic probes to report on the radical or cationic nature of intermediates by affording different products for different mechanistic scenario. For the pMMO system, experiments on cryptically chiral ethanes and *d,l*-[2-$^{2}H_{1}$,3-$^{2}H_{1}$] butanes[43] has ruled out the a radical mechanism for the hydroxylation chemistry in pMMO. Instead, it has been proposed that the mechanism of O-atom transfer to both alkanes and alkenes is concerted oxenoid insertion.[41, 43, 44] No carbon kinetic isotope effect was observed for the oxidation of propane,[44] or butane oxidation[43] indicating little or no conformational change at the carbon center during transition state formation at the rate-limiting step. When propene and 1-butene were used as epoxidation substrates, the enantiomeric excess (ee) of the enzymatic products was only 18% and 37%, respectively.[45] However, studies on *trans*-2-butene revealed only the *d,l*-2,3-dimethyloxirane products and on *cis*-2-butene, only the *meso* product.[41] These latter observations indicate that the enzymatic epoxidation also proceeds *via* the concerted electrophilic *syn* addition (**Fig. 9**).

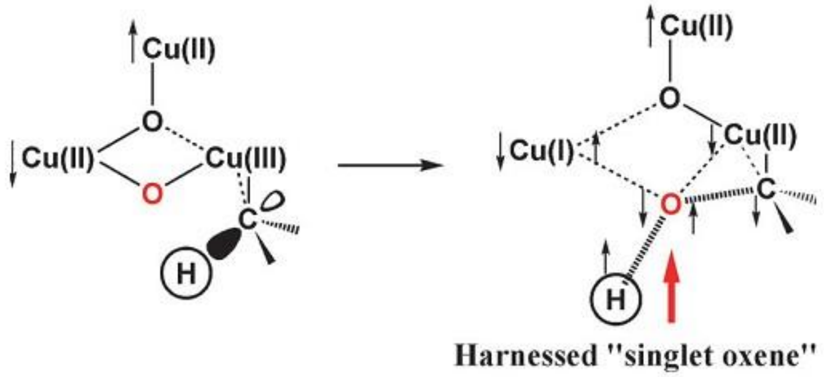

Fig. 9 Details of the adiabatic “singlet oxene” transfer from a dioxygen-activated trinuclear copper cluster to methane to form the transition state and denote the “up” and “down” directions of the unpaired electron spins.

Given that the oxidation of hydrocarbons mediated by pMMO involves a direct concerted O-atom insertion mechanism, there must be a binding pocket for the hydrocarbon substrate in close proximity to the catalytic site. The substrate-binding pocket should also include both copper and a hydrophobic cavity for the hydrocarbon substrates. Using pentane as the ligand, the search for its possible binding sites was carried out by the binding sites prediction program Dockligand (LigandFit) on Discovery Studio 1.7 (Accelrys Software Inc.) using the first published crystal structure. The most probable site was determined to be the hydrophobic pocket previously identified near site D in the structure adjacent to the tricopper cluster that had been modeled into the crystal structure (**Fig.8**).

The third milestone of the tricopper catalytic model is the recent development of catalysts for methane oxidation. Based on their understanding of the catalytic mechanism of pMMO, Chan and coworkers have synthesized a series of tricopper complexes that show their ability to mediate facile oxidation of many organic hydrocarbons including methane.[32-34, 38] Remarkably, they have successfully prepared a tri-copper peptide complex based on twelve amino acid residues from PmoA and PmoC of pMMO from the *Methylococus capsulatus* (Bath). It is noted that this peptide (HIHAMLTMGDWD) lines the empty hydrophobic cavity at the D site in the protein crystal structure.[24] Upon activation of the $Cu^ICu^ICu^I$-peptide complex by dioxygen in the presence of propylene or methane, they observed rapid oxidation of these substrates. The dioxygen-activated tricopper-peptide complex is capable of mediating facile epoxidation of propylene, as well as methane oxidation at room temperature. The efficiency of propylene epoxidation reaction is extremely high since only propylene oxide is produced, with over 50% of the expected product is formed within ten minutes. The yield of methane oxidation is slightly lower, about 12% based on the tricopper-peptide complexes encapsulated in the mesoporus carbon over the two-hour experiment. Because the $Cu^ICu^ICu^I$-peptide complex is not soluble in aqueous solutions, oxidation of the substrates was carried out with the peptide complex encapsulated in mesoporous carbon. Not mentioned is the difficulty of methane oxidation compared to propylene epoxidation and methane enrichment in mesoporous material, which may be the reason why the yield of obtained transformation is low. To improve the efficiency of methane oxidation by tricopper cluster, they have then synthesized a tricopper complex based on an organic framework. When this $Cu^ICu^ICu^I$ complex is activated by excess dioxygen in the presence of excess CH_4, the reaction is complete within 10 minutes. Under this condition, single turnover (turnover number, TON) of 0.92 is obtained. At the ambient temperature

doi:10.6342/NTU201903909

and pressure, pMMO, the most efficient methane oxidizer, has a turnover frequency of 1 s^{-1}. So the two tricopper complexes, derived from pMMO and a biomimetic model tri-copper cluster, are capable of facile conversion of methane to methanol as pMMO.

In summary, the exact identification of catalytic site and mechanism of methane oxidation in pMMO is a complicated and long-standing problem. The common consensus is that pMMO is a multi-copper enzyme. The two models proposing copper ions at the catalytic mechanism should be considered for further investigations. Each model has its own supporting evidences and limitations. New experimental evidences are in urgent need to distinguish between the two models in particular and to understand the working mechanism of pMMO at a whole.

1.5 The importance of biological nitric oxide sensing

Nitric oxide (NO) was long considered as a toxic, gaseous pollutant from the oxidation of ammonium and incomplete combustion of gasoline. However, in the 1980s NO was discovered to serve as a physiological regulator, a cellular secondary message in biological system.[46] Until now, NO has been known as more diverse physiological roles: it also regulates the transcription factors to affect gene expression,[47, 48] and is a cytotoxic killer in immune reactions.[49, 50] In the biological system, NO often tends to form nitrosyl metal complexes with metalloproteins, which further reacts with dioxygen or nucleic acid, amino acid side chain, and variety of amines and thiols.[51] Dinitrosyl iron complexes (DNIC) are one type of nitrosyl metal complexes, serving as a biological marker of NO-mediated [Fe-S] cluster degradation with characteristic EPR signal, g_{av} = 2.03. Although the ligands of DNIC mainly is mostly thought of as thiolates, they still contain a wide range

doi:10.6342/NTU201903909

of O/N/S ligation as observed in the protein studies.[52]

1.6 The chemistry of NO

The gaseous stable radical, NO, is usually involved in nitrosylation with thiol groups or metal irons such as ferrous ions or zinc ions. The labile reactivity of NO is result from the radical character. The molecular orbital diagram of NO (**Fig. 10**) shows that an unpaired electron in a π* molecular orbital. This electronic configuration elucidates the high reactivity of NO molecule, in particular, the ease of oxidation to the nitrosonium ion (NO^+), the probability of reduction to the nitroxide ion (NO^-), the facile attack by oxygen leading to formation of NO_2. NO is isoelectronic with the dioxygen monocation (O_2^+), and NO^+ is isoelectronic with CO and CN^-, while NO^- is isoelectronic with O_2, having a triplet ground state. The bond length of free NO is 1.154 Å, lying between that of a double (1.18 Å) and a triple (1.06 Å) bond. A bond order of 2.5 about free NO is also consist with the Molecular orbital diagram. In IR stretching frequencies, ν_{NO} decreases with increasing charge from 2377 (NO^+) through 1875 (NO) to 1470 cm^{-1} (NO^-).

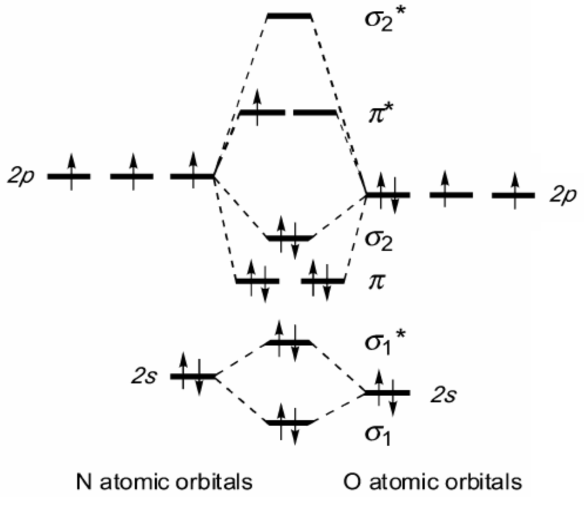

Fig. 10 Molecular orbital diagram of NO.

doi:10.6342/NTU201903909

1.7 The multiple electronic configurations of NO bound to the metal center

In a molecular orbital approach, the bonding of NO to a metal is thought of as having two components. **Fig. 11** displays that nitrosyl metal complexes are composed of several possible electron configurations. Metal-nitrosyl bonding involves donation of electron density from NO to the metal through a σ orbital on the N atom (Fig. 10 and Fig. 11. B) followed by the backdonation from metal d_π orbitals to the π^* orbitals of NO. The d_π-π^* interaction is shown in Fig. 11 B While NO binds to the metal center, there are three possible configurations of NO: (1) NO^+ (2) $NO^\cdot$ (3) NO^-. Therefore, the valence of the central metal can be determined only after understanding the electronic configurations of NO.

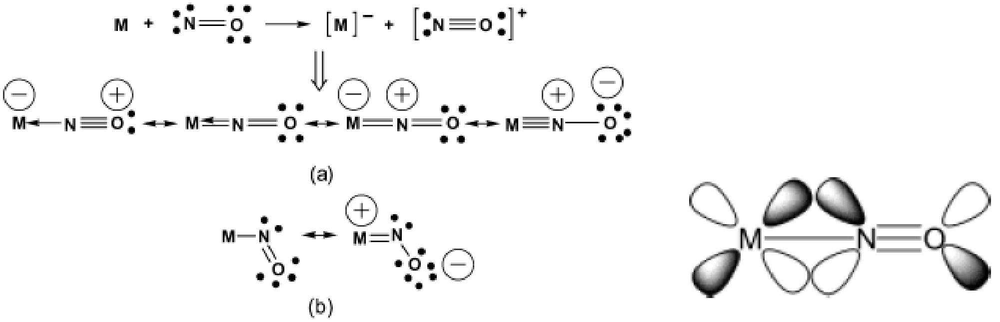

Fig. 11 A. The possibility of Metal-NO; B. d_π-π^* interaction of Metal-NO

In recognition of the covalent nature of the M-N-O interaction and the difficulty of assigning formal oxidation states to the metal and the NO in nitrosyl complexes, Enemark and Feltham proposed a formalism which treated the metal nitrosyl as a single entity. This was represented as $\{M(NO)_x\}^n$, in which n is the total number of electrons associated with the metal d_π and π^* (NO) orbitals. The number of d electrons is determined by the formal oxidation state of the metal atom, assuming no charge on the NO group.[53]

1.8 The origins and metabolism of nitric oxide in biology

NO is generally synthesized by NO synthase (NOS) via using L-arginine as a substrate biologically. NOS is a family including three isoforms which include neuronal NOS (nNOS), inducible NOS (iNOS) and endothelial NOS (eNOS). nNOS is relevant with the signal transmition, the memorial formation and learning in neurons; iNOS appears as a cytotoxic reagent target to pathogens in macrophage; eNOS is responsible for the vasodilation in the smooth muscle of blood vessel.[54]

After synthesis of NO, under the normal physiological condition, stepwise pathways involved in oxyhemoglobin (oxy Hb) help NO be oxidized to nitrite which is considered as a marker of constitutive nitric oxide synthase activity (NOS) and a circulating storage and delivery source of NO. Then nitrite is further endogenously oxidized to form nitrate in the similar to other mechanisms (**Fig. 12**).[55]

On the other hand, nitrite, the primary oxidative NO metabolite, can be reversed to form nitric oxide or NO-derivate compounds through catalysis of metal ions or enzymes. For example, recent studies suggest that xanthine oxidoreductase present abundantly in vascular endothelium, may reduce nitrite to NO.[56] (In plants, NO is ascribed from the reduction via nitrite reductase.) These cellular activities of nitrite, combined with its stability and abundance in vivo, suggest that this anion has a distinct and important signaling role in mammalian biology, perhaps by serving as an endocrine messenger and synchronizing agent.[57][58]

doi:10.6342/NTU201903909

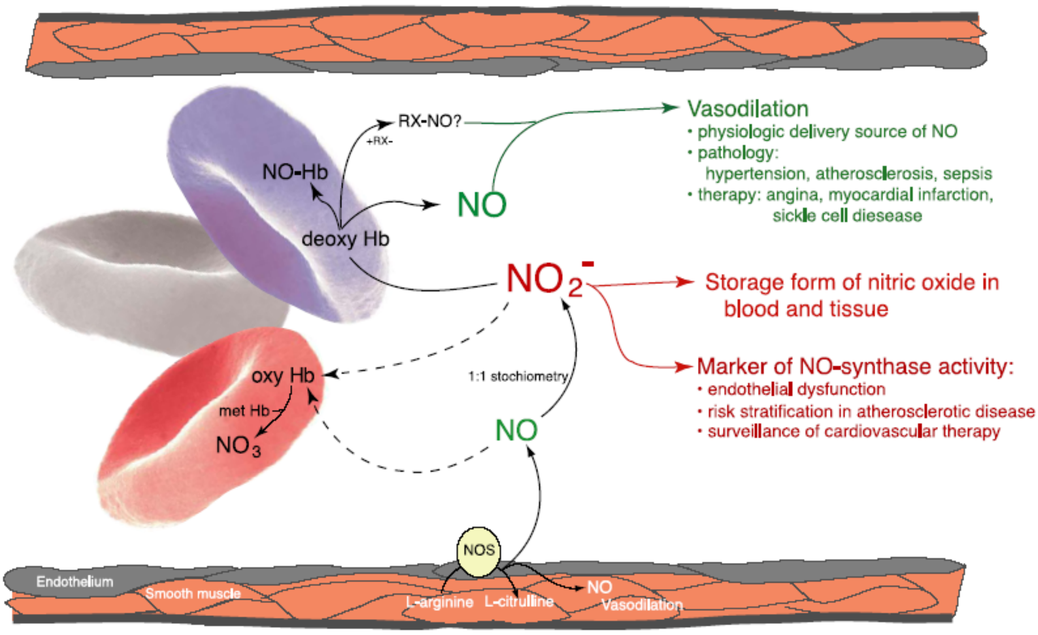

Fig. 12 Potential role of nitric oxide and nitrite in human biology. [58]

Furthermore, NO may trigger the nitrosative stress that leads to the formation of peroxynitrite (NO_3^-) and N_2O_3 which are the products of the reaction of nitric oxide with superoxide or disproportionation under hypoxia. These nitrogen reactive species (NRS) usually incorporate in the nitrosylation and nitrosamine formation[59, 60] or are reduced to nitric oxide, respectively. Whatever, the destiny of these NRS is to be finally oxidized to the form, nitrate, in liver and kidney, excreting it into the urine.[59]

In the biological system, NO often tends to form nitrosyl metal complexes with metalloproteins, which further reacts with dioxygen or nucleic acid, amino acid side chain, and variety of amines and thiols. Dinitrosyl iron complexes (DNIC) are one type of nitrosyl metal complexes, serving as a biological marker of NO-mediated [Fe-S] cluster degradation with characteristic EPR signal, g_{av} = 2.03. Although the ligands of DNIC mainly is mostly thought of as thiolates, they still contain a wide range of O/N/S ligation as observed in the protein studies.[46, 61-64]

1.9 The FNR (fumurate and nitrate respiratory protein): gene regulation

For the FNR family of transcription factors, direct contacts with RNAP are necessary for transcription activation.[65, 66] FNR contains three individual activating regions (ARs) that mediate contacts with RNAP (**Fig. 13A**). These include AR1, AR2, and AR3, predicted to recognize the a-CTD, the a-N-terminal domain, and r70, respectively.[67] Furthermore, the influence of each AR on transcription activation appears to depend on promoter architecture (**Fig. 13B**). At class I promoters in which the FNR recognition site is centered at -61.5 bp or further upstream of the +1 transcription start site (TSS), AR1–a-CTD interactions are required for transcription activation.[68-71] However, the mode of RNAP recognition differs for class II promoters, which constitute the most frequently occurring FNR-dependent promoters and contain the FNR target site *41.5 bp upstream of the TSS. At class II promoters, all three ARs have the potential to make contacts with RNAP, with AR1 and AR3 having predominant roles and AR2 making only a minor contribution.[70-73] Consistent with this notion, the structure demonstrates that AR3 forms a surface exposed loop that is poised to make interactions with r70 as previously predicted by alanine mutagenesis.[68] Usually FNR AR1 accelerates RNAP isomerization from a closed to an open complex at an FNR dependent synthetic class II promoter.[73] Although further work is needed to solve the FNR–RNAP cocrystal structure to elevate our understanding of the protein–protein.

doi:10.6342/NTU201903909

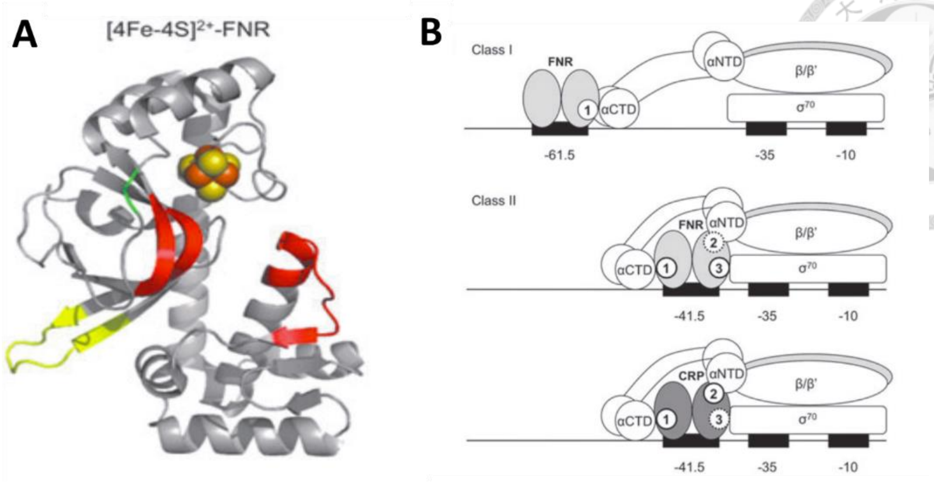

Fig. 13 **(A)**The ARs within FNR that are involved in interacting with RNAP. Shown are the monomeric crystal structures for [4Fe-4S]-FNR [PDB code 5E44] in cartoon representation with their respective cofactors shown as spheres and ARs highlighted: AR1 (red), AR2 (green), AR3 (yellow). **(B)** Promoters that are activated by FNR can be categorized into two main classes. At a class I promoter, the FNR binding site is centered *61.5 bases or further upstream of the transcriptional start site (+1), allowing FNR to make contacts with RNAP through AR1 in the downstream subunit. At a class II promoter, the FNR binding site is centered *41.5 bases upstream of the +1, and FNR is poised to make multiple contacts with RNAP through AR1 in the upstream subunit and AR2 and AR3 in the downstream subunit, although AR2 plays only a minor role.[74]

1.10 Three dimensional structures of FNR and their implications

FNR is the protein switch that controls the transition between anaerobic and aerobic respiration in *Escherichia coli* (*Ec*) and related facultative anaerobes.[75]

FNR is a member of the CRP [cyclic adenosine monophosphate (cAMP) receptor protein] superfamily of homodimeric transcription factors.[76] Proteins belonging to this superfamily consist of a C-terminal DNA binding domain that recognizes specific sequences within numerous promoters, an extensive helical coiled-coil dimer interface, and an N-terminal sensory domain.[77] In FNR, the N-terminal residues of Cys20, Cys23, and Cys29, which, along with Cys122 (*E. coli* numbering), can coordinate an iron-sulfur cluster. In the absence of O_2, FNR coordinates a $[4Fe\text{-}4S]^{2+}$ center, forms a dimer, and specifically binds to DNA.[78, 79] Conversely, in the presence of O_2, the cluster is rapidly degraded in a second-order reaction to a $[3Fe\text{-}4S]^{+}$ intermediate and then spontaneously to a $[2Fe\text{-}2S]^{2+}$ center, causing FNR monomerization.[80] Monomeric FNR does not bind DNA and consequently is unable to interact with RNA polymerase and regulate gene expression.[81] After prolonged O_2 exposure, FNR completely loses its iron-sulfur cluster. [82] Transcriptional control through an iron-sulfur cluster-modulated monomer-dimer transition is unique to the FNR family of regulators and has been the subject of intense scrutiny.[75, 83-85] Accordingly, the numerous site-directed mutagenesis studies and their interpretation have been based on homology models built from the known CRP structure.[85] Recently, the 2.65 Å resolution dimeric structure of [4Fe-4S]–containing FNR from the marine bacterium *Aliivibrio fischeri* (*Af*) has been reported.[86, 87] *Af*FNR has the same length as *Ec*FNR and shares 84% of amino acid sequence identity with it, which complement an *fnr*$^{-}$ *E. coli* mutant,[86] and behaves very much like the *E. coli* regulator.

doi:10.6342/NTU201903909

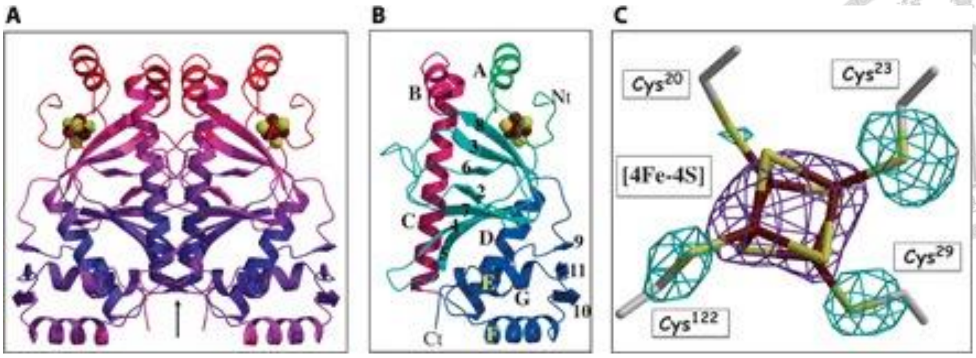

Fig. 14 Structure of holo-AfFNR [PDB code 5E44]. **(A)** Ribbon depiction of the AfFNR dimer color-coded according to increasing temperature factor values (blue to red). The arrow represents the twofold axis of the AfFNR dimer. **(B)** The AfFNR monomer domains; crimson, dimerization α-C helix; blue, C-terminal (Ct) DNA binding domain; light blue, β-roll domain; green, N-terminal (Nt) iron-sulfur cluster-binding domain. Helices are sequentially named with letters as in other CRP superfamily members; β-strands are denoted with numbers. **(C)** Composite electron density at the AfFNR [4Fe-4S] cluster; purple, 2.65 Å resolution anomalous scattering peak from the data collected at the iron edge and contoured at 7σ; light blue, (Fobs − Fcalc) map with the sulfur atoms of Cys20, Cys23, Cys29, and Cys122 omitted from the calculated structure factors and phases (3.6σ).[87]

1.11 The quest for the sensing mechanism of NO in FNR

Since NO is ubiquitous and reactive, it is no surprise that bacteria have tailored complex and specific transcriptional responses to it. Rodionov et al.[88] performed a useful bioinformatic analysis of all the known dedicated NO-responsive transcription factors and their DNA-binding sites throughout the genomes of proteobacteria. The *E.*

coli FNR [4Fe4S] cluster reacts not only with O_2 but also with NO.[78-81] Reaction with NO is extremely rapid, multiphasic and results in the formation of a protein-bound nitrosylated iron sulfur cluster that resembles a pair of Roussin's red esters.[83] Reaction directly with NO inhibits FNR DNA-binding activity in vitro and FNR-dependent transcription in vivo.[83] The inactivation of FNR by NO seems one-end road for nitric oxide sensing. However, [4Fe4S] cluster with nitric oxide shows different products under chemistry investigation. DNIC is not only product. FNR was suggested to be a final safeguard against NO toxicity by switching off transcription of genes involved in nitrate and nitrite respiration, thereby minimizing endogenous NO production when the dedicated NO-responsive regulators and detoxification systems are overwhelmed, however, no direct investigation was applied to observe its behaviors.

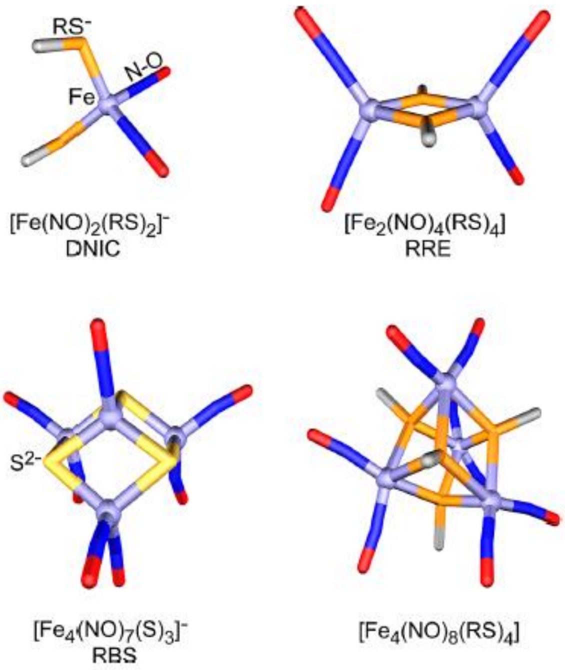

Fig. 15 Structures of iron-nitrosyl species.[84] Structures of (mononuclear iron) dinitrosyl iron complex (DNIC), Roussin's red ester (RRE), Roussin's black salt (RBS),

and a putative tetranuclear iron octanitrosyl cluster species. Iron, sulfide, thiol, and NO are indicated. All products were observed in the reaction of [4Fe4S] with nitric oxide.

1.12 Basic theory of X-ray absorption spectroscopy (XAS)

X-ray absorption spectroscopy (XAS) has been used to study a variety of metal sites in biological system. It is one of the premier tools for investigating the local structural environment of metal ions. Structural characterization of metal complexes has played a crucial role in the development of coordination chemistry. Despite the tremendous advances that have taken place in spectroscopic methods for structure elucidation, X-ray crystallography remains the method of choice for definitive determination of the structure of a new coordination complex. Unfortunately, X-ray crystallography cannot always be used. Some samples simply cannot be crystallized in diffraction quality crystals. X-ray crystallography is unable to provide a complete structural description. In contrast, for all of these cases, X-ray absorption spectroscopy (XAS) can provide unique structural information.

XAS can be divided into X-ray absorption near edge structure (XANES), which provides information primarily about geometry and oxidation state, and extended X-ray absorption fine structure (EXAFS) that provides information about metal site ligation. The two methods give complementary structural information. The development of

doi:10.6342/NTU201903909

X-ray absorption spectroscopy as a practical tool has been concurrent with a major development of intense synchrotron radiation X-ray source that permit the study of samples which are dilute in the element of interest, which is often the case with biological sample.

1.13 The physical basis of X-ray absorption spectrocopy

X-ray energies are sufficiently high to eject, via the photoelectric effect, one or more core electrons from an atom. Each core electron has a well-defined binding energy, and when the energy of the incident X-ray is scanned across one of these energies, there is an abrupt increase in the absorption coefficient. This is the so-called 'absorption edge' of the element. The importance of XAS derives from the fact that there is fine structure superimposed on the absorption edge. This fine structure is often divided into extended X-ray absorption fine structure (EXAFS), referring to structure well above the absorption edge, and X-ray absorption near edge structure (XANES), for structure in the immediate vicinity of the edge.

doi:10.6342/NTU201903909

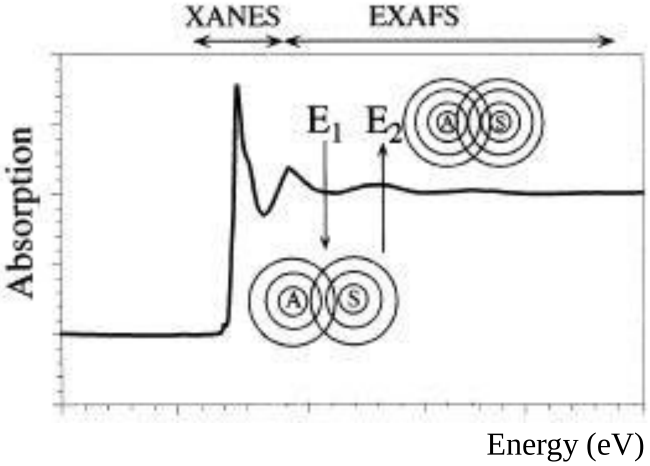

Fig. 16 Schematic illustration of an X-ray absorption spectrum. In the inset, **A** and **S** refer to the absorbing and scattering atoms, respectively. The concentric circles around **A** and **S** represent the maxima in the photoelectron wave that describes the propagation of the X-ray excited photoelectron.

X-ray absorption spectrum of any matrial, whether atomic or molecular in nature, is characterized by sharp increases in absorption at specific X-ray photon energies, which are characteristic of the absorbing element. These sudden increases in absorption are call absorption edges and correspond to the energy required to eject a core electron into the continuum, thus producing a photoelectron.

The absorption discontinuity is known as the K-edge when the photoelectron originates from a 1s core level, and it is call the L-edge when the ionization is from a 2s or 2p electron. **Fig.16** shows a typical energy level diagram.

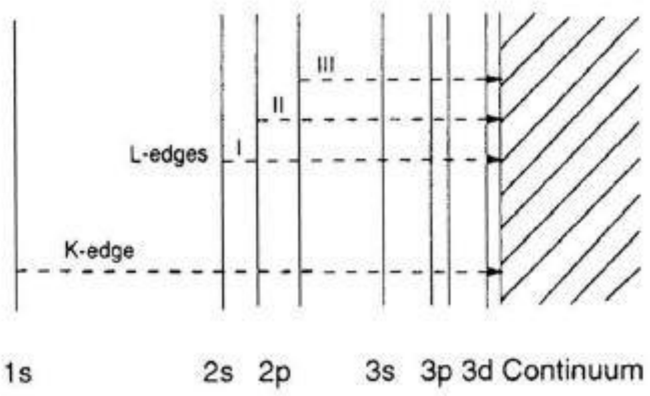

Fig. 17 X-ray absorption energy level diagram showing the K-edge and L_I, L_{II}, and L_{III} edges for a typical first row transition metal.

The major application of XAS in biology has been in the study of the structure of the metal site in metalloproteins and metalloenzymes. The advantage of XAS is being made in the field of bioinorganic chemistry, where important questions of correlation between structure and function of the metal site in metalloprotein are often recised and are amenable to XAS study.

1.14 Extended X-ray absorption fine structure (EXAFS)

The photo-excitation cross section is modulated by the interference between the out-going and the back-scattered photoelectron waves. This is illustrated schematically in the insets to **Fig.17**. This results in a decreasing photoelectron wavelength, and thus, in alternating destructive interference and constructive

doi:10.6342/NTU201903909

interference. The physical origin of EXAFS is thus electron scattering. For a single absorber–scatterer pair, this alternating interference will give rise to sinusoidal oscillations in the absorption coefficient if the energy is given in units proportional to the inverse photoelectron wavelength (the photoelectron wavevector, or k, defined as in Eq. (1)). In Eq. (1), the threshold energy, Eo, is the binding energy of the photoelectron.

$$k = \sqrt{2m_e(E-E_0)/h^2} \qquad (1)$$

In XAS analyses, it is typical to define the EXAFS, $\chi(k)$, as the fractional modulation in the X-ray absorption coefficient. The observed oscillations can be described by an equation similar to Eq. (2).

$$x(k) = \sum_j N_j S_j(k) F_j(k) e^{(-2\sigma^2{}_j k^2)} e^{(-2r_j/\lambda(k))} \frac{\sin(2kr_j + \phi_{ij}(k))}{kr_j^2} \qquad (2)$$

In Eq. (2), the parameters that are of principal interest to the chemist are the number of scattering atoms (N_j) and the absorber–scatterer distance (r_j). To a first approximation, these can be related to the depth of modulation and the frequency of the modulations, respectively. However, a variety of other parameters that must either be determined or be defined in order to extract the chemically relevant information. Principal among these are $F_j(k)$ and $f_{ij}(k)$. These represent, respectively, the energy dependence of the photoelectron scattering, and the phase shift that the photoelectron wave undergoes when passing through the potential of the absorbing and scattering atoms. These amplitude and phase parameters contain the information necessary to identify the scattering atom.

The main consequence of this damping is that the EXAFS information is limited to atoms in the near vicinity, typically within 10 Å, of the absorber. There are three additional damping terms in Eq. (2). The S_0 term is introduced to allow for inelastic loss processes and is typically not refined in EXAFS analyses. The first exponential term is a damping factor that arises from the mean free path of the photoelectron ($\lambda(k)$). This serves to limit further the distance range that can be sampled by EXAFS. The second exponential term is the so-called "Debye-Waller" factor. This damping reflects the fact that if there is more than one absorber–scatterer distance, each distance will contribute EXAFS oscillations of a slightly different frequency. The destructive interference between these different frequencies leads to damping in the EXAFS amplitude. The Debye-Waller factor, s_{ij}, is the root-mean-square deviation in absorber-scatterer distance. This damping is always present due to zero-point thermal

doi:10.6342/NTU201903909

motion, and may, for polyatomic systems, also occur as a consequence of structural disorder.

The summation in Eq.(2) reflects the fact that all absorber-scatterer pairs contribute to the observed oscillations. However, it is not realistic to refine all of the different absorber-scatterer interactions. Consequently it is necessary to group absorber-scatterer interactions into “shells”. A shell is a group of similar scatterers at approximately the same distance from the absorber. Although Eq.(2) provides a complete description of the EXAFS oscillations.

1.15 X-ray absorption near edge spectroscopy (XANES)

X-ray absorption spectroscopy (XAS) has become a prominent tool for the element-specific analysis of transition metals at the catalytic center of metalloenzymes. In a typical *K*-edge X-ray absorption spectrum of a transition metal complex, the first onset of absorption coincides with transitions of the 1s core electron to d-orbital. Occurrence of p-d mixing may result in a dramatic increase of the transition probability of these otherwise dipole-forbidden transitions and, thus, appearance of a resolvable pre-edge peak. The structure in the spectra observed within about 40 eV from the onset of absorption, the X-ray absorption near-edge structure (XANES), is determined by transitions to bound states, quasi-bound states, and (partially) localized continuum states with p-orbital symmetry. In molecular systems, the XANES states are closely

doi:10.6342/NTU201903909

related to unoccupied molecular orbitals. XANES analysis has been used for numerous metalloenzymes to obtain insights into the metal-oxidation state and its coordination geometry. It has proved to be the ideal method to ascertain the oxidation states of copper ions since it provides a direct spectroscopic probe of Cu^I ions. The absorption feature at 8984 eV in the Cu K-edge X-ray absorption spectra has been shown to be associated quantitatively with reduced copper.[89] This has been attributed to the 1s to 4p electric dipole-allowed transition in Cu^I ions of various coordination environments according to ligand field analysis. This diagnostic signature of Cu^I ions has been observed in all of the Cu K-edge X-ray absorption spectra of the as-isolated pMMO membranes obtained to date, albeit with varying degrees of intensity, hence indicative of different levels of reduction. Fe foil was always measured simultaneously with the sample and the first inflection point at 7112.0 eV of the Fe foil spectrum was used for energy calibration for FNR. This diagnostic signature of Fe^{II} ions has been observed in all of the Fe K-edge X-ray absorption spectra of the as-isolated FNR obtained to date, albeit with varying degrees of intensity, hence indicative of different levels of reduction.

1.16 Advantages and limitations of XAS

The principal advantage of XAS as a structural probe is that it is a local structure probe. None of the discussion above requires the presence of long-range order. This means that XAS can be used to study non-crystalline samples or to compare solution structure with solid state structure. In ideal circumstances (see below for some of the

doi:10.6342/NTU201903909

limitations), EXAFS data can be analyzed to determine the absorber-scatterer distance with an accuracy of ca. 0.02 Å, and a precision that is substantially better (0.004 Å, and perhaps even better under carefully controlled conditions).[90] Coordination numbers can be determined with an accuracy of ca. 25% and scatterer identity can typically be defined to the nearest row of the periodic table.[91]

In comparison with small molecule crystallography, the information available from XAS is relatively limited. However, for non-crystalline systems, XAS may provide the only available structural information. Even for crystalline systems, there are cases in which EXAFS can provide a different, and perhaps better, structural description than is available from crystallography. Several examples of this are discussed below. Finally, XAS has, through XANES transitions, the ability to provide oxidation state and spin-state information that can be difficult or impossible to extract from crystallographic measurements.

In comparison with other spectroscopic methods, XAS has the decided advantage that it is always detectable, without the need for specific spin states or isotopic substitution, and that it is element specific. Every element has at least one unique absorption edge, although for the very light elements, this edge energy may actually be in the UV, not in the X-ray region. For elements heavier than about phosphorous, measurement of the X-ray absorption spectrum is relatively straightforward using

doi:10.6342/NTU201903909

modern synchrotron X-ray sources, and even the lighter elements are studied frequently. The universal detectability of XAS is, of course, a mixed blessing since it means that XAS is a bulk technique sensitive to all of the forms of an element that are present in a sample. If the element of interest occurs in multiple environments only the average structure can be determined.

1.17 Basic theory of EPR spectroscopy

Electron resonance is a branch of absorption spectroscopy in which radiation of microwave frequency is absorbed by molecules possessing electrons with unpaired spins. Electron paramagnetic resonance (EPR) spectroscopy has provided detailed structure information on a variety of paramagnetic organic and inorganic systems. Most of the knowledge on the structure of molecules has been obtained from the analysis of molecular absorption spectra. EPR can be applied to paramagnetic metalloenzymes and other paramagnetic metalloproteins, as well as to free radical intermediates in biochemical reactions, to probe protein conformational changes, the structure and reactivity of enzyme intermediates, the geometry of ligand binding sites, and redox changes in electron transfer components.

Electromagnetic radiation may be regarded as coupled electric and magnetic fields. Their field oscillations are perpendicular to one another and to the propagating

doi:10.6342/NTU201903909

direction of electromagnetic radiation. Electromagnetic radiation in the microwave region will interact with molecules that have a permanent electric dipole moment. When the energy of a quantum of incident radiation matches the energy level separation, the absorption will occur. In the absence of a magnetic field, the energy levels are coincident. Magnetic dipoles attributable to electrons arise from net spin or net orbital angular momentum or from a combination of these. Resonant absorption of radiation in a static magnetic field by such systems is invariably referred to as electron paramagnetic resonance (EPR) or electron spin resonance (ESR). Electron paramagnetic resonance spectroscopy is a technique that is applicable only to systems with net electron spin or orbital angular momentum.

1.18 Energy of magnetic dipoles in a magnetic field

An analog of an orbital magnetic dipole is a particle of mass m and charge $-e$, rotating with velocity u in a circle of radius r in the xy plane. Associated with a circulating current i will be a magnetic a point magnetic dipole. Such a dipole has a component of magnetic moment $\mu_z = iA$ ($A=\pi r^2$) normal to the plane. So, the magnetic moment is given by

$$\mu_z = iA = \frac{-e\upsilon}{2\pi r}\pi r^2 = \frac{-e}{2m} m\upsilon r = \frac{-e}{2m} L_z \qquad (3)$$

If its instantaneous velocity is *u*, the particle has the angular momentum *L* = *mur*

According to quantum mechanism, it has an associated deBroglie wavelength λ = *h* /*p*. The square of the amplitude of this wave at any point around the ring is a measure of the probability of finding the particle at that point. For this probability to be time-independent, the wavefunction must be single-valued. Therefore, the wave must not interfere destructively with itself in propagating about the ring. This restriction requires the circumference to be an integral number M_l of deBroglie wavelengths. That is,

$$2\pi r = M_l \lambda = M_l \frac{h}{p} \tag{4}$$

Hence,

$$L_z = pr = M_l \frac{h}{2\pi} = M_l \eta \tag{5}$$

Finally, the magnetic moment is

$$\mu_z = \frac{-e}{2m} L_z = \gamma M_l \eta \qquad M_l = 0, \quad \pm 1, \quad \pm 2, \ldots. \tag{6}$$

The proportionality constant $g = -e/2m$ is called the magnetogyric ratio. Positive values of m_l correspond to rotation in a clockwise sense around the *z*-axis and negative values correspond to counter clockwise rotation around the *z*-axis.

Magnetic moment and angular momentum are proportional, both in classical and in quantum mechanics. In other words, the spin magnetic moment of an electron is proportional to its angular momentum. The component of electron spin magnetic moment m_z along the direction of the magnetic field H is

$$\mu_z = \gamma_e M_s \eta = -g\beta M_s \tag{7}$$

The negative sign appears because of the negative charge of the electron. The constant $b = e\eta/2m$ is called the Bohr magneton ($b = 9.2741\times10^{-21} erg\ /\ gauss$). The extra factor g is called the g-factor of the electron (2.0023). Thus one may expect that the magnetic moment operator μ_z should be proportional to the spin operator

$\hat{S}_Z$ That is,

$$\hat{\mu}_z = \gamma \hat{S}_z \eta = -g\beta \hat{S}_z \tag{8}$$

The energy of a magnetic moment in a magnetic field H is $E =-m_zH$. Hence, the spin Hamiltonian operator is given by

$$\hat{E} = g\beta H \hat{S}_z \tag{9}$$

In other words, in the presence of a magnetic field, the energy of an electron in a state

doi:10.6342/NTU201903909

M_s is

$$E = g\beta HM_s \tag{10}$$

1.19 The Zeeman effect

The energy separation is predominately due to the interaction of unpaired electrons with applied magnetic field. This effect is called the Zeeman Effect. Because the electron has a magnetic moment, it acts like a bar magnet when it is in a magnetic field. It will have a lowest energy state when the magnetic moment of electron is aligned with the magnetic field and a highest energy state that the moment of electron is aligned against the magnetic field. The allowed values of M_s range in unit increments from $-S$ up to $+S$, giving $2S+1$ components along an arbitrary direction. For the single electron, the spin angular momentum vectors and their projected components are $S = -1/2$ and $S = 1/2$. From quantum mechanics, the two possible values of E are $\pm\, gbH/2$. Therefore, the transition between the two Zeeman levels can be induced by an electromagnetic field of the appropriate frequency v, if the photon energy hv matches the energy-level separation ΔE.

Then,

$$\Delta E = h\nu = g\beta H_r \tag{11}$$

v

is expressed in hertz (Hz), and H_r is the magnetic field at which the resonance condition.

1.20 Thermal equilibrium and spin-lattice relaxation

The application of a magnetic field to a system of unpaired electrons results in a splitting of the Zeeman levels into two components. A simple notation uses the symbols α and β for states with Ms = +1/2 and –1/2, respectively.

The n_{α} and nβ are the populations of the upper and lower levels, respectively at thermal equilibrium. Additionally, the P↑ and P↓ correspond to the respective upward and downward lattice-induced transition probabilities. These are called lattice-induced transitions because it is assumed that the spin system is coupled in some way to the bulk sample or lattice. When the spins are in thermal equilibrium, it is energetically more favorable for a spin to be in the lower energy level. Not all spins will be in the lower state since the thermal energy will be sufficient to excite them into the higher level. The ratio of the number of spins in the Zeeman levels depends on the relative values of the average thermal energy (kT) and the energy gap (gbH) between states. This is given by the Boltzmann distribution.

$$\frac{n_{\alpha}}{n_{\beta}} = e^{-\Delta E / \kappa T} = e^{-g\beta H / \kappa T} \tag{12}$$

In fact, the energy splitting *gbH* is so small that this ratio is almost unity at room temperature. However, when the system is excited by electromagnetic radiation at resonance, it is no longer necessarily in thermal equilibrium. The populations in Zeeman levels can become equalized, unless the excess spins in the upper state are able to lose energy and drop down into the lower state to maintain the thermal equilibrium according to Boltzmann distribution.

The process that the spins in the upper state can lose energy is known as spin-lattice relation. The timescale of the process is characterized by the spin-lattice relaxation time (T_1). The spin-lattice relaxation time depends on the molecular environment. Relaxation times are short in solids or systems with paramagnetic ions (fast relaxation), but relatively long in liquids (slow relaxation). On the one hand, if the spin-lattice relaxation time is too short, the lines may be broadened out so much as to become undetectable. On the other hand, if it is too long, the signal may become saturated. That is because the radiation-induced transitions take place too quickly for the relaxation process to be effective.

Consider the Heisenberg Uncertainty Principle, written in terms of uncertainties in the energy and in the time:

$$\Delta E \Delta t \geq \frac{h}{2\pi} \tag{13}$$

doi:10.6342/NTU201903909

If T_1 is used as an estimate of Δt, then a small T_1 value will lead to a large ΔE.

Therefore, there will be a broadening of the lines observed in the EPR spectrum.

1.21 *g*-values

The *g* value is a universal constant. In free radicals, the unpaired electron is often delocalized over the whole molecule. Here, the g-value of the free radical approaches very closely to the theoretical value for a free electron of $g_e = 2.0023$. The transition metal ions have g-values which differ significantly from $g_e = 2.0023$. One of the reasons is that there is a well-defined orbital motion associated with the transition metal ion wavefunction. Thus, the *g* value can be considered as a quantity characteristic of the molecule in which the unpaired electrons are located.

The Zeeman interaction is independent of field direction only in isotropic systems, where it can be represented by a single value. In other words, if x, y, and z are equivalent, the g value will $g_{xx} = g_{yy} = g_{zz}$. In anisotropic systems, the Zeeman interaction becomes orientation dependent. If the molecule contains axial symmetry, (x and y are equivalent) then $g_{xx} = g_{yy} \neq g_{zz}$. It is common in such cases to designate the g values as $g_{//}$, the g value parallel to the symmetry axis ($g_{//} = g_{zz}$), and $g_\perp$ for the g value perpendicular to this axis ($g_\perp = g_{xx} = g_{yy}$).

doi:10.6342/NTU201903909

1.22 Hyperfine interactions

The nuclei of atoms in a molecule or complex often have a magnetic moment, which produces a local magnetic field at the electron. The interaction between the electron and the nuclei is called the hyperfine interaction.

In other words, the lines in an EPR spectrum can be split by interaction of the paramagnetic electron with the magnetic moments of neighboring nuclei. These splittings are called hyperfine splittings that arise from the magnetic field associated with the nuclear moments. But not all atoms have nuclei that have magnetic moments.

The Hamiltonian operator for the hyperfine interaction is

$$\hat{E}_{iso} = hA_0 \hat{S}_z \hat{I}_z \tag{14}$$

Hence, the spin Hamiltonian operator for hydrogen atom is obtained by Eqs. (8) and (12).

$$\hat{E} = g\beta H \hat{S}_z + hA_0 \hat{S}_z \hat{I}_z \tag{15}$$

In other words, the energies of these states are Ea_ea_n, Ea_eb_n, Eb_eb_n, and Eb_ea_n.

$$E_{\alpha_e\alpha_n} = +\frac{1}{2}g\beta H + \frac{1}{4}hA_0$$

$$E_{\alpha_e\beta_n} = +\frac{1}{2}g\beta H - \frac{1}{4}hA_0$$

$$E_{\beta_e\beta_n} = -\frac{1}{2}g\beta H + \frac{1}{4}hA_0$$

$$E_{\beta_e\alpha_n} = -\frac{1}{2}g\beta H - \frac{1}{4}hA_0$$

For transition metal ions, the hyperfine splitting comes from the nucleus of the paramagnetic ion, and smaller superhyperfine structure is due to the ligand. In general, a spin nucleus splits the spectrum into $2I + 1$ hyperfine lines of equal intensity.

Chapter 2 Methods and Experiments

2.1 Bacterial strains, plasmids, and growth conditions

E. coli strains DH5α (Yeastern Biotech), K12 TB1 (New England Biolabs), BL21 PLys (Novagen) and plasmids pET 21b (Novagen), pET 22b (Novagen) and pMAL™-p2X (New England Biolabs) were used for DNA manipulations and protein overexpressions. They were grown in Lucia-Bertani medium (LB medium) in the presence of ampicillin (50 μg/mL). The growth of M. capsulatus (Bath) (ATCC 33009) was carried out following the procedures established by Chan et al. on nitrate mineral salts medium (NMS buffer, ATCC buffer).

2.2 Methods for DNA manipulation, mutagenesis studies, recombinant protein expression and purification of pMal-pmob containing membrane fraction

2.2.1 Construction of the expression plasmids pMAL-p2X(pmob) and pMALp2X(deSPpmob1 & deSPpmob2)

The genomic DNA of *M. capsulatus* (Bath) was obtained by following published procedures. The sequences of *pmob* (coding for amino acid residues 1−414), *deSPpmob1* (coding for amino acid residues 33−414, namely, without the signal sequence 1−32), and *deSPpmob2* (coding for amino acid residues 55−414, namely, without the signal sequence and with further truncation of the *N*-terminal domain) were

doi:10.6342/NTU201903909

amplified from the corresponding extracted *M. capsulatus* (Bath) genomic DNA. The twelve primers for *pmob*, *deSPpmob1*, and *deSPpmob2* are:

pmob-f1: 5´AATTCATGAAAACAATAAAGGACCGGA3´;
pmob-f2: 5´CATGAAAACAATAAAGGACCGGATTG 3´;
pmob-r1: 5´TTTACATGAACGACGGGATCAG3´;
pmob-r2: 5´AGCTTTTACATGAACGACGGGAT3´;
deSPpmob1-f1:
5´CGCGGATCCCACGGTGAGAAATCGCAGGCCGCGTT3´;
deSPpmob1-f2: 5´GGATCCCACGGTGAGAAATCGCAGGCC3´;
deSPpmob1-r1: 5´TTTACATGAACGACGGGATCAG 3´;
deSPpmob1-r2: 5´AGCTTTTACATGAACGACGGGAT 3´;
deSPpmob2-f1: 5´AATTCTGGTCGAAAGAGAAAGTCAAG 3´;
deSPpmob2-f2: 5´CTGGTCGAAAGAGAAAGTCAAG 3´;
deSPpmob2-r1: 5´TTTACATGAACGACGGGATCAG 3´; and
deSPpmob2-r2: 5´AGCTTTTACATGAACGACGGGAT 3´.

These primers, together with *pfu* turbo DNA polymerase (Stratagene), were used in the polymerase chain reactions. pMAL^{TM}-p2X was digested by *EcoR* I and *Hind* III (New England Biolabs, Inc.) and ligated with the PCR products by T4 DNA ligase. The three resultant recombinant plasmids, pMAL-p2X(*deSPpmob1* & *deSPpmob2*) and pMAL-p2X(*pmob*), were amplified by *E. coli* DH5α and established by sequence analysis. Since each of the target genes is fused to the 3´-end of the maltose-binding protein (MBP) gene by an intervening linker coding for the 24 amino-acid sequence NSSSNNNNNNNNNNLGIEGRISEF, which includes the Factor Xa cutting site

doi:10.6342/NTU201903909

(IEGR), the MBP tag can be excised from each of the PmoB proteins in various experiments, including the preparation of antibodies.

2.2.2 Mutagenesis of the expression plasmids pMAL-p2X(pmob) and pMALp2X(deSPpmob1 & deSPpmob2)

In addition to the *pmob* genes coding for the full-length PmoB, PmoB$_{33–414}$, and PmoB$_{55–414}$ proteins, we have cloned the genes encoding the full-length PmoB Y374F mutant, the *N*-terminal truncated PmoB$_{33–414}$Y374F mutant, and the Y374F, Y374S and M300L mutants of the PmoB$_{55–414}$ protein. To generate the Y374F, Y374S, and M300L mutant proteins, the corresponding *pmob* target genes were site-directed mutated in the recombinant plasmids pMAL-p2x(*pmob*, *deSPpmob1* or *deSPpmob2*). The six primers for Y374F, Y374S, and M300L are:

Y374F-f1: 5'GCGGCGTGGGAAGTGTTCCGTCTGTC3';
Y374F-r1: 5'GACAGACGGAACACTTCCCACGCCGC3';
Y374S-f1: 5'CGGCGTGGGAAGTGAGCCGTCTGTCCGACA3';
Y374S-r1: 5'TGTCGGACAGACGGCTCACTTCCCACGCCG3';
M300L-f1: 5'CCGCGCCATGCGGTTGAAGCTGACCAT3'; and
M300L-r1: 5'ATGGTCAGCTTCAACCGCATGGCGCGG 3’.

Otherwise, the same procedures were used to produce the site-directed *pmob* mutant plasmids as described earlier.

A list of the target PmoB proteins is shown in Table 1. The protein construct for the full-length PmoB fused to the MBP is illustrated in Scheme 2.

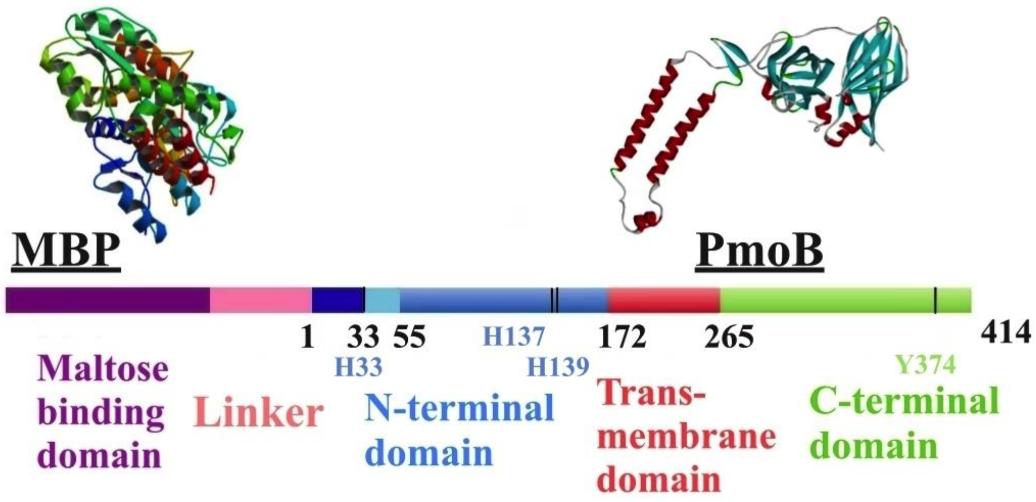

Fig. 18 the protein construct for the full-length PmoB fused to MBP. The *N*-terminus and *C*-terminus of the PmoB are highlighted in *blue* and *green*, respectively, with the signal peptide (residues 1 - 32) colored in *deep blue*, and the transmembrane domain from residues 172 to 265 depicted in *red*. The linker between the MBP and the PmoB containing the site of cleavage by Factor Xa is shown in *magenta*.

Table 2 List of the target PmoB proteins.

PmoB mutants	**Description**
PmoB	The full length PmoB protein
PmoB Y374F	The full length PmoB mutant with Tyr374→Phe
PmoB$_{33–414}$	*N*-truncated PmoB mutant w/o residues 1−32
PmoB$_{33–414}$ Y374F	*N*-truncated PmoB mutant w/o residues 1−32 and Tyr 374→Phe
PmoB$_{55–414}$	*N*-truncated PmoB mutant w/o residues 1−54
PmoB$_{55–414}$ Y374F	*N*-truncated PmoB mutant w/o residues 1−54 and Tyr374→Phe

PmoB$_{55–414}$ Y374S	*N*-truncated PmoB mutant w/o residues 1−54 and Tyr374→Ser
PmoB$_{55–414}$ M300L	*N*-truncated PmoB mutant w/o residues 1−54 and Met300→Leu

2.2.3 Purification and characterization of the expressed MBP-PmoB$_{55–414}$ fusion protein and the target PmoB$_{55–414}$ protein

The *E. coli* K12 TB1 cells were grown in LB buffer with or without supplemented 1.0 mM CuCl$_2$. The concentration of copper ions in the LB broth medium without adding CuCl$_2$ is about 10 μM. Following 3.0 h induction mediated by isopropyl-β-D-thiogalactopyranoside (IPTG), the corresponding 600 ml cell growth (OD$_{600}$ = 0.80 −1.0) was harvested by centrifugation at 8,000 × *g*, 4°C for 20 min. The cells obtained were re-suspended in 20 ml Tris-HCl buffer (20 mM, pH 7.0) with or without the addition of 10 mM sodium ascorbate containing 10 μM DNase I, 100 μM phenylmethylsulfonyl fluoride (PMSF).

To obtain the periplasmic fraction of the *E. coli* cells, the osmotic shock protocol was used to remove the spheroplasts.[99] These *E. coli* cells were grown without supplemented CuCl$_2$. We began with suspension of the cell pellets thoroughly in a 30 ml solution of 30 mM Tris-HCl, 20% sucrose, at pH 8.0, and then added 60 μl EDTA (0.50 M, pH 8.0). After collecting the cells by centrifugation at 4^{o}C for 10 min at 10,000 × *g*, we re-suspended the pellets in ice-cold MgSO$_4$ solution (5.0 mM, 30 ml) by slowly stirring for 10 min on ice. The shocked cells were centrifuged at 4^{o} C at 10,000 × *g* for another 10 min. We separated the pellets (the spheroplasts) and collected the supernatant (periplasmic fraction) for SDS-PAGE analysis.

The *E. coli* cells were lysed by passing them through a French® Pressure Cell Press (SIM-AMINCO, Spectronic Instruments) two to three times at 20,000 lb/in^2, or were disrupted by sonication (XL-2020, Misonix, Inc.). Unbroken cells and cell debris were removed by centrifugation at 27,000 × *g* for 30 min at 4°C. The supernatant was then ultra-centrifuged at 220,000 × *g* for 60 min at 4°C to separate the membrane fraction. After ultra-centrifugation, the supernatant was regarded as the cytosolic/periplasmic fraction.

The pellet was composed of the membrane parts of the cells. The membranes were washed with Tris-HCl buffer in 1:1 ratio (v/v) using a Dounce homogenizer, and re-suspended in 20 mM Tris buffer (5.0 ml) again. This process was repeated once again to remove most of the soluble proteins. The cellular membranes and its associated proteins remained in the pellet. All the buffer solutions for protein purification were degassed and bubbled with Ar (99.99% purity) for three times.

2.3 Methods for DNA manipulation, recombinant protein expression and purification of FNR

E. coli BL21 PLys (DE3), transformed with the expression vector pET22bFNR, was grown at 37°C in LB medium containing 100 mg L^{-1} ampicillin. Until the optical density of growth medium at 600 nm reached 0.7, transcription was induced with

doi:10.6342/NTU201903909

isopropyl-1-thio-β-D-galactopyranoside (IPTG, 0.5 mM) for 3 h, and the cells were pelleted by centrifugation at 8,000 g for 30 min. The cell pellets were further re-suspended with M9 medium containing 100 mM KNO_3. The cell media were subsequently transferred into a 2-liter duran bottle, filled with medium 9 with nitrate salt and incubated for 24 h at 4^{o}C. The cells were again collected by centrifuge at 8,000 g for 30 min. The obtained pellets were frozen in liquid nitrogen and stored at -80^{o}C.

Protein purification was carried out under strictly anaerobic conditions in a vinyl anaerobic chamber (Coy Product). Typically, it was operated at <1.00 ppm O_2 by volume, and all buffers were sparged with oxygen-free nitrogen gas for at least 2.0 h. Cells pellets were resuspended in 10 ml buffer A (20 mM imidazole, 400 mM NaCl, 50 mM sodium phosphate, PH 8.0) per liter of culture, and proper DNase I powder and 0.10 mM PMSF were added before cell lysis by passage through a French pressure cell three times at 12,500 psi/cm^2. Cell debris was removed by centrifugation and the resultant supernatant was then filtered through 0.22 μm syringe filter. To isolate FNR from extract, the supernatant was applied to a His Trap HP column (5-mL, GE Healthcare). The washed buffer, buffer B (50 mM imidazole, 400mM NaCl, 50mM sodium phosphate, PH 8.0) was used for removing non-binding proteins. The elution buffer C (250 mM imidazole, 400 mM NaCl, 50 mM sodium phosphate, PH 8.0) was applied to obtain the yellow-brown fractions that contain His$_6$-FNR. Finally, these fractions were passed through a desalting column (GE Healthcare) to remove the imidazole. The proteins were then analyzed by sodium dodecyl sulfate (SDS) polyacrylamide gel electrophoresis (PAGE) (Mini PROTEAN_3 cell, Bio-Rad) and mass spectrometry (API QSTAR, Applied Biosystems, MA, USA). The purified proteins were quantified by the Bradford method (Bio-Rad) using bovine serum albumin (BSA) as the standard. Another alternative procedure of expression and

doi:10.6342/NTU201903909

purification was also chosen. Non-nitrate-incubated cells were collected and followed with the same protocol but by the employment of buffers A, B and C, respectively, containing 100 mM $NaNO_3$.

2.4 Material

Chemicals	**Source**
Acetic acid/CH_3COOH	Merck
Acrylamide 40% $CH_2CH{=}CONH_2$	Bios
Ampicillin	Genemark
Agarose I	Amresco
Ammonium persulfate $(NH_4)_2S_2O_8$	Amresco
Baco agar	BD
N,N'-Methylene-bisacrylamide/ $C_7H_{10}N_2O_2$	Plusone
Boric Acid/H_3BO_3	RDH
Calcium chloride $CaCl_2 \cdot 2H_2O$	Merck
Chloroform:isoamyl Alcohol (24:1)	Amresco
Coomassie brilliant blue R-250 $C_{45}H_{44}N_3O_7S_2Na$	Amresco
Copper(II) chloride	RDH
Cyanocobalamin/ $C_{63}H_{88}CoN_{14}O_{14}P$	Sigma

d-Biotin/$C_{10}H_{16}N_2O_3S$	Sigma
(DNase I) Deoxyribonuclease I	Sigma
di-Sodium hydrogen phosphate/Na_2HPO_4	J.T.Baker
Dithiothreitol/$C_4H_{10}O_2S_2$	Sigma
(DTT) DL-dithiotheifol	Sigma
Ethanol/C_2H_5OH	Merck
[Ethylenedinitrilo]-tetraacetic acid disodium salt $C_{10}H_{14}O_8N_2Na_2 \cdot 2H_2O$	Mallinckrodt
Ethidium bromide/$C_{21}H_{20}BrN_3$	Amresco
Folic acid/$C_{19}H_{19}N_7O_6$	Sigma
Glycerol/$C_3H_8O_3$	Amresco
Glycine/NH_2CH_2COOH	J.T.Baker
Guanidine	Mallinckrodt
Hydrochloric acid/HCl	RDH
Imidazole/$C_3H_4N_2$	Fluka
Iron(II) sulfate $FeSO_4 \cdot 7H_2O$	Aldrich
Iso-Propanol/C_3H_8O	Mallinckrodt
(IPTG) Isopropylthio-β-D-galactoside/$C_9H_{18}O_5S$	Amresco
LB-Broth powder	Bio-basic
Lysozyme	Sigma
Manganese(II) chloride $MnCl_2 \cdot 4H_2O$	RDH
Mangnesium sulfate $MgSO_4 \cdot 7H_2O$	J.T.Baker
Methanol/CH_3OH	Merck
Nickel chloride/$NiCl_2 \cdot 6H_2O$	RDH
Nicotinamide/$C_6H_6N_2O$	Sigma
Nitric acid/HNO_3	Merck
D-Pantothenic acid hemicalcium salt/$C_9H_{16}NO_5 \cdot 1/2Ca$	Sigma
Phenol:chloroform:isoamyl Alcohol (25:24:1)	Amresco
Phenylmethylsulfonyl fluoride/$C_7H_7FO_2S$	Sigma
Potassium dihydrogen phosphate/KH_2PO_4	Aldrich
Potassium nitrate/KNO_3	Merck
Protease K	Amresco
Riboflavin/$C_{17}H_{20}N_4O_6$	Sigma
Sodium acetate/$Na_2(CH_3COO)$	J.T.Baker
Sodium chloride/NaCl	RDH
Sodium dodecyl sulfate	Amresco

$C_{12}H_{25}NaO_4S$	
Sodium hydroxide/NaOH	RDH
Sodium Nitrate	RDH
Sodium molybdate $Na_2MoO_4 \cdot 2H_2O$	Mallinckrodt
Sulfuric acid/H_2SO_4	Aldrich
N,N,N’,N’-tetramethylethyldiamine/$C_6H_{12}N_2$	Plusone
Thiamine hydrochloride $C_{12}H_{17}ClN_4OS \cdot HCl$	Sigma
Tris/$C_4H_{11}NO_3$	Amresco
Zinc sulfate/$ZnSO_4 \cdot 7H_2O$	RDH

2.5 Instrumentations

General. All chemicals were regent grade purchased from commercial sources and used as received unless stated otherwise. UV-visible spectra were recorded on a HP 8453 diode array spectrometer or Beckman Coulter DU-800. HR-ESI (Waters LCT Premier XE) mass spectra were obtained using dual ionization source options and limitation is m/z<1500. Gas chromatography was performed by using an Aglient HP6890 plus instrument equipped with either a flame ionization detector (FID) or a 5971 EI-MS detector and separated by a HP-1 or HP-5 capillary column (60m x 0.25 mm x 0.25 μm film thickness). The analysis conditions were as follows unless stated otherwise: carrier gas, nitrogen, 1.0-2.1 ml min^{-1}; oven temperature, 100°C; injection port, 280°C with a splitless ratio.

UV/Vis Spectroscopy

A Hwelett-Packkad 8453 and Beckman Coulter Du-800 UV-visible was used for analysis with 1.0 cm quartz cuvettes and PMMA disposable cuvettes.

Gas chromatography

Aglient HP6890 plus instrument equipped with either a flame ionization detector (FID) or a 5971 EI-MS detector and separated by a HP-1 or HP-5 capillary column (60m x 0.25 mm x 0.25 μm film thickness). The analysis conditions were as follows unless stated otherwise: carrier gas, nitrogen, 1.0-2.1 ml min^{-1}; oven temperature, $100^{o}C$; injection port, $280^{o}C$ with a splitless ratio.

Orbital Shaker Incubator

FIRSTEK SCIENTIFIC S300R was used to culture the *E. coli*.

Laminar Flow

NUAIRA Biological Safety Cabinets, Class II TYPE A/B3, a Laminar Flow cabinet, is a carefully enclosed bench designed to prevent contamination of biological samples, or any particle sensitive device. Laminar flow cabinets may have a UV-C germicidal lamp was used to sterilize the shell and content when not in use.

Centrifuge

SORCALL RC-5 PLUS was usd equipped as following, Rotor, SLA-300 aluminum fixed, Max 12,000 rpm, SS-34 aluminum fixed-ANG, MAX 20,000 rpm. Centrifuge can increase the effective gravitational force on a test tube so as to more rapidly and completely cause the precipitate (pellet) to gather on the bottom of the tube. The remaining solution is supernatant. The supernatant liquid is the quickly decanted from the tube without disturbing the precipitate, or withdraw with a Pasteur pipette.

Ultra Centrufuge

Beckman, Coulter Optima L-90K Ultracentrifuge was employed. Rotor: 7-Ti, MAX

doi:10.6342/NTU201903909

70,000 rpm, 90Ti, MAX 90,000 rpm.

PCR machine

A Perkin Elner Gene-Amp PCR system 2400 was used to amplify target gene form *Methylococuss capsulats* and *E.coli K12* with forward and reverse primers for polymerase chain reactions.

Real time PCR machine

Applied Biosystems 7300 Real-Time PCR System was used to relatively quantify and analyze the target gene mRNA products in the designed microbes with forward and reverse primes.

Anaerobic Chamber

Coy Vinyl Anaerobic chambers are constructed of flexible PVC with padded base, efficient vacuum airlock, and aluminum support frame. The air-sensitive samples were operated in the chamber. The anaerobic condition was maintained under less than 1 ppm of Oxygen concentration.

X-ray absorption spectroscopy

X-ray absorption data was collected at Synchrotron Radiation Research Center in Hsin-Chu (Beamline Wiggler 17C) using a Si(111) double crystal monochromator in the region of the K-edge for Cu (8,979 eV and for Fe (7113.0 eV). Under such a low flux, we can reduce photo damage of the sample significantly by performing the measurements at ca. 4°C and using the sleeping mode (i.e., without shining X-ray on the sample) for 4−18 sec after every 6−36 sec X-ray irradiation during data collection. The cooling of the sample was accomplished with a cold air device. Membrane samples were loaded on to either a sample holder (1.4 cm x 1.4 cm x 0.2 cm) covered with sheets of kapton or sealed in a polyethylene bag. The samples studied were sufficiently thin to allow total penetration of the incident X-ray beam. The absorption spectra were collected in fluorescence mode with a Lytle detector, and the photon energy for copper ions was scanned using 5-eV steps in the pre-edge regions (8,759−8,959 eV), 0.40-eV steps in the edge regions (8,959−9,034 eV), and 0.07-Å−1 increments in the EXAFS region (to k = 12 Å−1), integrating from 2 to 36 sec in a k3-weighted manner for a total scan length of approximately 60 min. For iron smaple, the photon energy was scanned from 6.912 to 8.012 keV. Under these conditions, the edge jump could be regarded as a measure of the content of the corresponding absorbing element in the sample. No photoreduction or -damage was evident from comparison of the first and last spectra collected for a given sample. A reference Cu foil was always measured simultaneously with the sample with the first inflection point of the Cu foil spectrum at 8979.0 eV. Energies were calibrated using an internal Fe foil stardard, assigning the first inflection point to 7111.3 eV

Electron paramagnetic resonance spectroscopy, EPR

EPR spectra were recorded at the X band (9.5 GHz) by using a Bruker X-band E500CW spectrometer (Bruker Biospin). The sample temperature for the purified proteins and their nitroxylated complexes was maintained at 77 K by immersion of the EPR sample tube into a liquid nitrogen Cold Finger Dewar. For in vivo whole-cell measurements, the temperature was maintained at 77 K. Typical EPR measurement conditions were as follows: microwave frequency, 9.5 GHz; microwave power, 2 mW; modulation frequency, 100 kHz; modulation amplitude, 0.5 m Tesla; receiver gain, 6.32 x10^3 . Spin concentrations were measured by double integration of the first-derivative EPR spectra and comparison with the corresponding intensities of known standards.

Circular Dichroism (CD) spectroscopy

The CD spectrum of nitrosylated FNR protein was determined on π* CD spectrometer (AP). The CD spectrum of the sample was record in 1-mm cell from 190-600 cm^{-1}, respectively, at room temperature. A scan interval of 1 nm with an integration of 100,000 points was employed. The spectrum of Buffer A was also collected and subtracted automatically.

ICP-OES

The Agilent technologies ICP-OES 720S was used for the digested samples. The protein samples were dissolved in saturated 65% HNO_3 solution (5.0 mL) (suprapure grade, Merck). The samples were digested at 180°C 800W in a MARS5 microwave digestion system (CEM Inc.). The temperature was altered from room temperature to 180°C in 15 min, and maintained at 180°C for another 15 min. The digested samples were then diluted with the addition of 20 ml doubly distilled water (Millipore) prior to iron analysis. The iron concentrations of the samples were determined by a standard linear plot of series concentrations of standard $Fe(NO_3)_2$ solution in 0.10 N HNO_3. A solution of 0.10 N HNO_3 in distilled water was used as the iron-free control.

Fluorescence spectrophotometer

Sealed florescence cuvettes (Hellma) were prepared anaerobically. Fluorescence

doi:10.6342/NTU201903909

anisotropy was measured in a HITACHI F-4500 fluorescence spectrophotometer at 27.4°C using an excitation of 483 nm and detecting emission at 517 nm.

Chapter 3 The PmoB Subunit of Particulate Methane Monooxygenase (pMMO) in Methylococcus capsulatus (Bath): The Cu^{I} Sponge and its Function

Published in *Journal of Inorganic Biochemistry 196* (2019) 110691,

DOI: 10.1016/j.jinorgbio.2019.04.005.

Yu-Jhang Lu,[a,b,†] Mu-Cheng Hung,[a,c,d,†] Brian T.-A. Chang,[a,e] Tsu-Lin Lee,[a,f] Zhi-Han Lin,[a] I-Kuen Tsai,[a,g] Yao-Sheng Chen,[a] Chin-Shuo Chang,[a] Yi-Fang Tsai,[a] Kelvin H.-C. Chen,[g] Sunney I. Chan,[a,h*] and Steve S.-F. Yu[a,b,c,i*]

From the [a]Institute of Chemistry, Academia Sinica, Taipei 11529, Taiwan
[b]Genetics and Genomics Ph.D. Graduate Program, Academia Sinica and National Chung Hsing University, Taichung 40227, Taiwan
[c]Chemical Biology and Molecular Biophysics Program, Taiwan International Graduate Program (TIGP), Academia Sinica, Taipei 11529, Taiwan
[d]Institute of Biochemical Sciences, National Taiwan University, Taipei 10617, Taiwan
[e]Department of Chemistry, National Tsing-Hua University, Hsinchu 30013, Taiwan
[f]Graduate Institute of Applied Science and Technology, National Taiwan University of Science and Technology, Taipei 10607, Taiwan
[g]Department of Applied Chemistry, National Pingtung University, Pingtung 90003, Taiwan
[h]Division of Chemistry and Chemical Engineering, California Institute of Technology, Pasadena, CA 91125, USA
[i]Department of Chemistry, National Cheng Kung University, Tainan 70101, Taiwan

The contributions of the coauthors to this article are: Y.-J.L., Z.-H.L., T.-L.L. and Y.-S.C. constructed and designed the expression vectors for protein expression; M.-C.H., C.-S.C. and Y.-S.C. conducted the mutagenesis study; Y.-J.L., M.-C.H., B.T.-A.C. and C.-S.C. carried out the specific activity measurements on the recombinant PmoB; B.T.-A.C. purified the MBP-PmoB$_{55-414}$; Y.-J.L., B.T.-A.C., T.-F.T. and S.S.-F.Y. conducted the EPR and/or XAS experiments; M.-C.H., B.T.-A.C., Z.-H.L., I.-K.T., C.-S.C. and Y.-S.C. performed the quantification of the copper contents in the proteins, and the protein quantification using antibodies; B.T.-A.C., Z.-H. L., I.-K.T. and C.-S.C. grew the *E. coli* cells for the biochemical and biophysical characterization of the recombinant proteins; K.H.-C.C., S.S.-F.Y. and S.I.C. designed the research; S.S.-F.Y. and S.I.C. wrote the paper. † These authors contribute equally to this work.

Supplementary material such as Table S1-3, FigS1-S5 are attached in the Appendix.

3.1 Background

It has been known for some years that the pMMO from *M. capsulatus* (Bath) contains as many as 12-15 copper ions if the protein is purified under anaerobic conditions.[12, 27, 28, 37, 39] When the Cu^I enzyme solubilized in detergent is purified by chromatography in air, some of the copper ions become oxidized and can be stripped off from the protein.[12, 36, 37] Surprisingly, the bulk of the copper ions of the enzyme are associated with the PmoB subunit.[36, 37, 39] Clearly, with so many copper centers distributed among the three protein subunits, the study of this membrane system is extremely challenging. A strategy has been developed to dissect the problem into functional domains. As effectiveness of this strategy, we have recently identified and studied a hydrophilic construct embodying a tricopper cluster site sequestered within the transmembrane domain of the PmoA and PmoC subunits and demonstrated that a tricopper peptide complex prepared from the amino acid residues of this peptide is capable of mediating facile methane oxidation as well as propene epoxidation when the $Cu^ICu^ICu^I$ tricopper cluster is activated by O_2 under ambient conditions.

Using this same approach, we have cloned and over-expressed the water-soluble *apo* *N*-terminal and *C*-terminal domains of the PmoB subunit individually in *Escherichia coli* (*E. coli*) and showed that the *C*-terminal domain is a Cu^I-sponge, sequestering as many as 10 Cu^I ions.[39] The binding of the Cu^I ions was found to be cooperative. Interestingly, Cu^{II} ions exhibit very low affinity for this domain, suggesting that it is necessary to involve copper transport/trafficking proteins (or copper chaperones) to

doi:10.6342/NTU201903909

incorporate these copper ions into this region of the PmoB subunit for proper assembly of the native protein fold.[12] In our earlier work, the *N*-terminal domain was expressed only as an inclusion body. It was subsequently expressed with a glutathione S-transferase tag and the solubilized protein was shown to be capable of binding 3－4 copper ions, either Cu^{II} or Cu^{I} (data not published). Thus, there is no question that many copper ions of pMMO are associated with the PmoB subunit.

On the other hand, following a similar strategy, Rosenzweig *et al*.[15] have reported a recombinant variant spmoB of the PmoB *N*-terminal soluble fragment (residues 33－172) containing both the **A** and **B** sites tethered to the *C*-terminal fragment (residues 265－414) by a Gly-Lys-Gly-Gly-Gly (GKGGG) linker. This PmoB recombinant variant was demonstrated to coordinate a total of three copper ions. To obtain the *holo* spmoB, these researchers added $CuSO_4$ to the *apo* form of the recombinant protein to obtain the three-copper spmoB after purification accordingly. To clarify the differences between these results and our earlier findings, we have now cloned and over-expressed the full-length PmoB and two *N*-truncated PmoB subunits, as well as several of their mutants in a copper tolerant strain of *E. coli*, under conditions in which copper transport/trafficking proteins are available to ensure insertion of these copper ions during biosynthesis and proper assembly and folding of the membrane-bound PmoB proteins.[92-94] Indeed, we find that many Cu^{I} ions are associated with the PmoB proteins expressed in these *E. coli* membranes. Here, we describe biophysical characterization of these copper ions in the various PmoB constructs to clarify the number of copper ions, their redox state(s), and their reactivity toward O_2 and ferricyanide ($[Fe(CN)_6]^{3-}$). Armed with these results, and together with

doi:10.6342/NTU201903909

our recent finding that the catalytic site is most likely buried at the interface between the PmoA and PmoC subunits in the transmembrane domain of the protein complex[6, 33, 95] we can begin to understand the role played by these copper ions of the PmoB subunit in the catalytic cycle of the *holo* enzyme.

3.2 Results

3.2.1 Expression of the MBP-PmoB fusion proteins in the *E. coli* membranes

Following standard procedures, we clone the fusion genes of the target PmoB proteins with MBP in plasmids and express the MBP-PmoB proteins in *E. coli* K12 TB1 n of tcells. To help with the identificatiohe expressed target PmoB proteins and to determine the levels of expression of these proteins, we have resorted to Western blotting using anti-MBP monoclonal antibody/HRP conjugates. Expression of the MBP-PmoB fusion proteins is detected only in the membranes. There is no indication of any protein expression in the periplasm.

In addition, we have prepared antibodies to the recombinant PmoB$_{55\text{-}414}$ with the bound Cu^{I} ions. These antibodies allow us to identify the PmoB$_{55\text{-}414}$ domain of the expressed PmoB proteins within the bacterial cells or by SDS-PAGE *via* the Western blotting technique **(Fig. 19)**. To obtain the desired antibodies, we first remove the MBP fusion tag from the MBP-PmoB$_{55\text{-}414}$ protein purified from *E. coli* K12 TB1 cells by cleavage with factor Xa. Antiserum is then obtained by injection of the PmoB$_{55\text{-}414}$ (copper content 5.12 ± 0.45 per unit protein (*vide infra*)) into the rabbit. In Western

doi:10.6342/NTU201903909

blotting experiments, we find that the polyclonal antibodies obtained exhibit high affinity toward the PmoB domain in the recombinant MBP-PmoB$_{55\text{-}414}$ protein grown from the host *E. coli* K12 TB1 cells as well as in a control consisting of the purified pMMO protein with the PmoABC from *M. capsulatus* (Bath). The PmoB subunits from the pMMO and the recombinant MBP-PmoB$_{55\text{-}414}$ proteins are clearly spotted on SDS-PAGE gels with molecular masses at *ca*. 45 and 100 kDa, respectively (**Fig. 19**).

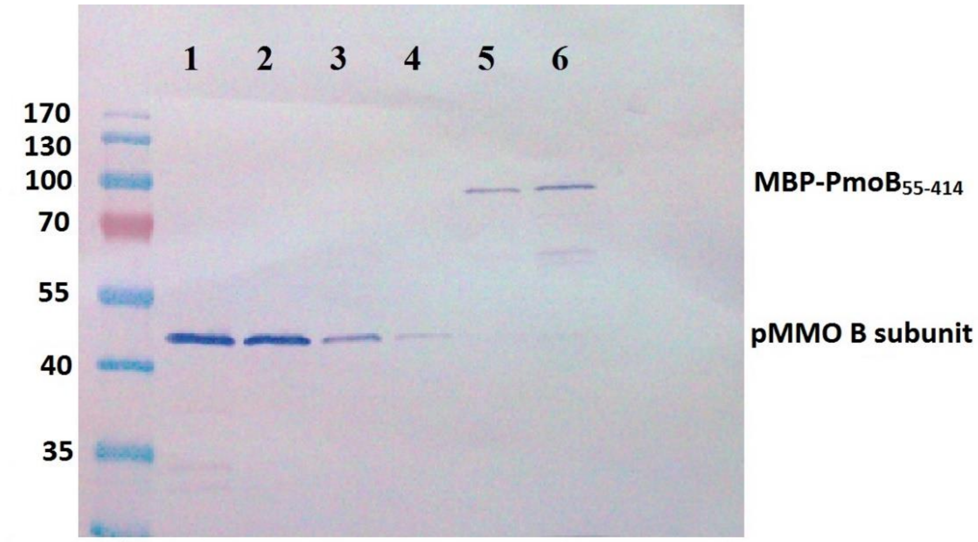

Fig. 19 SDS-PAGE/Western blotting visualization of the recombinant MBP-PmoB$_{55\text{-}414}$ from *E. coli* K12 TB1 cells and of the purified pMMO from *M. capsulatus* (Bath) using the rabbit antibodies raised against the copper-PmoB$_{55\text{-}414}$ protein (amino acid residues 55－414). The reader is referred to **Methods and experiments** section *2.2.3* for specifics on the Western blotting. Pre-stained protein markers are shown on the lane to the extreme left of the PmoB protein gels.

1. The whole cell protein extract of *M. capsulatus* (Bath) (grown in NMS buffer containing 30 μM copper ions).
2. pMMO-enriched membranes from *M. capsulatus* (Bath).

doi:10.6342/NTU201903909

3. pMMO-enriched membranes solubilized by DDM detergent.
4. purified pMMO complex.
5. The lysates of *E. coli* K12 TB1 cells obtained by the induction of MBP-PmoB$_{55\text{-}414}$ by IPTG (grown in the presence of 1.0 mM $CuCl_2$).
6. The membrane portion (the pellets after ultracentrifugation) of *E. coli* K12 TB1 cells obtained by the induction of MBP-PmoB$_{55\text{-}414}$ by IPTG (grown in the presence of 1.0 mM $CuCl_2$.

3.2.2 Purification of the MBP-PmoB$_{55\text{-}414}$ protein and determination of the copper content

Only the MBP-PmoB$_{55\text{-}414}$ protein is sufficiently stable outside of the membranes for detergent solubilization and column chromatography. Both the full-length MBP-PmoB and MBP-PmoB$_{33\text{-}414}$ proteins aggregate when subjected to this treatment.

After detergent solubilization into DDM, the MBP-PmoB$_{55\text{-}414}$ protein can be purified to homogeneity through a MBP affinity column and its copper content determined. We quantify the PmoB-protein content by Western blotting using anti-MBP monoclonal antibody/HRP conjugates and the level of copper ions by ICP-OES. The number of coppers bound to the purified MBP-PmoB$_{55\text{-}414}$ is determined to be 6.22 ± 1.03. After removal of the MBP tag by factor Xa, the corresponding number of copper ions is 5.12 ± 0.45.

3.2.3 Quantification of the MBP-PmoB proteins and the levels of copper ions in the membranes: Estimation of the copper contents of the

doi:10.6342/NTU201903909

various MBP-PmoB constructs

Although the MBP-PmoB proteins are over-expressed in the membranes, they account for only approximately 2% of the total proteins in the membranes. However, the bulk of the copper ions in the membranes are associated with the PmoB proteins. To demonstrate this, we have compared the X-ray absorption near edge spectra (XANES) in the Cu K-edge of the purified membranes of the *E. coli* K12 TB1 cells expressing the MBP-PmoB$_{55-414}$ protein with and without IPTG induction. Under the growth of *E. coli* cells without the induction of the PmoB expression, only a small Cu K-edge signal is observed for the isolated cell membranes (**Fig. 20(a)**). In the presence of IPTG, however, the Cu K-edge is significantly stronger for the membranes derived from the cells expressing the MBP-PmoB$_{55-414}$ protein. The edge jump observed for the latter is shown in **Fig. 20(b)**. From a comparison of the edge-jumps of the Cu K-edges from the membranes with and without induction of expression of the MBP-PmoB$_{55-414}$ (ratio 7/1), we conclude that the MBP-PmoB$_{55-414}$ protein accounts for at least 86% of the Cu ions in these membranes. Since some basil level of MBP-PmoB$_{55-414}$ is expressed in the absence of IPTG, this percentage represents a lower limit. Only several other membrane-bound copper proteins (cytochrome *bo* oxidase, NADH dehydrogenase-2, the copper trafficking protein CopA) are known based on a genomic search,[96] and these proteins contribute to these *E. coli* membranes at relatively lower levels.[97]

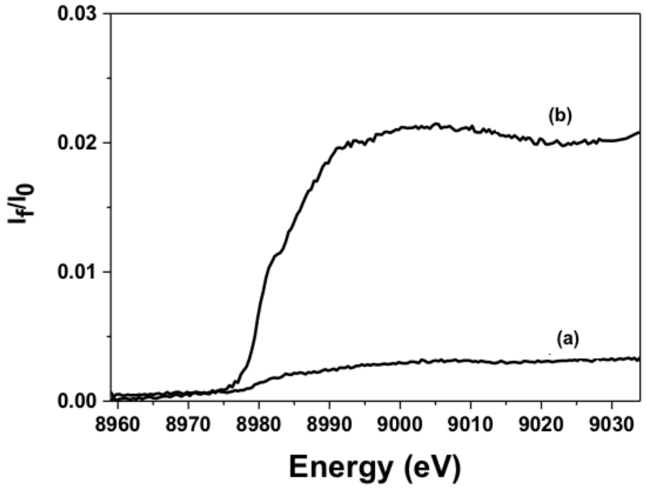

Fig. 20 The relative edge jumps of the Cu K_α near edge spectra of the cellular membranes from *E. coli* K12 TB1 strain containing the pMAL-p2X(*deSPpmob2*) plasmid without (**a**) and with (**b**) IPTG induction. The bacteria were grown with the addition of $CuCl_2$ (1.0 mM).

To quantify the MBP-PmoB protein levels within the membranes of the *E. coli* cells expressing these proteins, we have measured the PmoB-protein contents by Western blotting using anti-MBP monoclonal antibody/HRP conjugates as described earlier. Similarly, we determine the levels of copper ions in the membranes by ICP-OES. If the bulk of the copper ions in the membranes are indeed associated with the PmoB proteins, the copper contents of the various MBP-PmoB protein constructs could be assessed in this manner. These estimates provide upper limits of the copper contents since the contribution from the other copper-containing proteins in the membrane has not been accounted for. However, for a PmoB protein containing 10 copper ions, this correction would amount to no more than 1−2 copper ions, which is just outside the 10% uncertainty in the ICP-OES measurements. To illustrate, for the membranes expressing the MBP-PmoB$_{55\text{-}414}$, we obtain 9.03 ± 2.05 for the ratio of the total copper

doi:10.6342/NTU201903909

in the membranes to the PmoB protein content. After correcting for the contribution from other copper proteins, we predict a stoichiometry of 8 ± 2 copper ions per protein, which is in essential agreement with the copper content of 6.22 ± 1.03 determined for the purified MBP-PmoB$_{55\text{-}414}$ protein, considering that 1−2 copper ions on the average have been stripped off from the protein during detergent solubilization and column chromatography.

The copper contents determined in this manner for the *E. coli* membranes expressing the various target MBP-PmoB proteins are given in Table 2. From these data, it is clear that there are as many as 9−10 copper ions associated with the full-length MBP-PmoB protein when it is expressed in *E. coli* K12 TB1 cells. As expected, *N*-truncation of the PmoB subunit results in loss of copper ions, one copper ion on the average in the case of the MBP-PmoB$_{33\text{–}414}$ protein, and possibly, an additional copper ion in the case of the MBP-PmoB$_{55\text{–}414}$ protein. In the X-ray crystal structure of pMMO from *M. capsulatus* (Bath), His48, His72 and Gln404 are ligands to the mononuclear copper at the **A** site, while His33, His137 and His139 are associated with the dicopper center at the **B** site. Thus, some loss of copper ions is anticipated upon *N*-truncation of the PmoB protein, especially in the case of the MBP-PmoB$_{55\text{–}414}$ protein with the deletion of His33 and His48. Interestingly, replacement of Tyr374 by Phe or Ser results in the loss of a total of three copper ions, suggesting the importance of Y374 in stabilizing the structure of the dicopper copper-binding domain in this mutant.[98] In any case, these Cu contents are close to the numbers of Cu ions (6–9) suggested for the E-clusters in the *intact* pMMO protein isolated from *M. capsulatus* (Bath) [11, 36] or determined for the *C*-terminal water-exposed sub-domain of the pMMO B subunit (*ca.* 10),[39] especially when we make allowance for the three copper ions occupying the **A** and **B** sites, which we normally associate with the *N*-terminal domain and have referred to as a “C-cluster”.

Table 3 Copper contents of the purified PmoB$_{55-414}$ protein and of the membranes of the *E. coli* cells expressing the various MBP-PmoB proteins as quantified by ICP/OES and Western blotting.

Purified PmoB	Cu ions per protein	MBP-PmoB variants	Membrane Cu ions per protein
MBP-PmoB$_{55-414}$	6.22±1.03	PmoB$_{1-414}$	10.95±0.61
PmoB$_{55-414}$ (w/o MBP tag)	5.12±0.45	PmoB$_{33-414}$	9.54±1.00
		PmoB$_{55-414}$	9.03±2.05
		PmoB$_{55-414}$ Y374F	6.14±0.62
		PmoB$_{55-414}$ Y374S	5.93±0.57
		PmoB$_{55-414}$ M300L	8.20±0.31

3.2.4 The bulk of the copper ions in the membranes are Cu^{I}

We ascertain that the bulk of the copper ions accumulated within the membranes of the full-length MBP-PmoB as well as the *N*-truncated MBP-PmoB$_{33\text{-}414}$ and MBP-PmoB$_{55\text{-}414}$ proteins are Cu^{I}. The level of reduced copper ions is determined in each case on membranes (30 mg per 100 μl) suspended in Tris-HCl buffer (pH 7.0, 20 mM) using the BCA spectrophotometric method following the procedure of Yu *et al.*[39] These Cu^{I} contents of the purified membranes are given in **Table 4**. When we attempt to reduce any remaining copper ions in the membranes by the addition of ascorbate (final concentration 10 mM), the levels of Cu^{I} in the membranes change by less than 10%.

It is difficult to oxidize the Cu^{I} ions by O$_2$. This property of the reduced copper ions in the *E. coli* membranes is similar to that reported earlier for the recombinant *C*-terminal sub-domain of the PmoB in *E. coli*.[39]

Table 4 The redox state of the copper ions in the recombinant full-length MBP-PmoB protein and the *N*-truncated MBP-PmoB$_{33–414}$ and MBP-PmoB$_{55–414}$ variants in their purified membranes.

MBP-PmoB proteins	**Cu^{I}/Total copper**
PmoB$_{1–414}$	91.1%
PmoB$_{33–414}$ (freshly prepared)	90.2%
PmoB$_{33–414}$ (incubated in air for 2 days at 4°C after preparation)	39%
PmoB$_{55–414}$	92.5%

3.2.5 The MBP-PmoB fusion proteins expressed in the *E. coli* membranes are Cu^{I}- proteins based on X-ray absorption edge

measurements

We have compared the XANES in the Cu K-edge spectra of the various MBP-PmoB variants in the purified membranes of the *E. coli* K12 TB1 cells. In all cases, strong edge jumps are observed at 8,984 eV (**Fig. 21**, **S1–S3** in **APPENDIX**). Comparison of the edge shifts against $CuCl_2$ indicates that the bulk of the copper ions associated with the isolated membranes must be Cu^I for all the MBP-PmoB fusion proteins, the same conclusion derived from spectrophotometric BCA determination of the Cu^I in the purified membranes. With the large number of copper ions associated with each protein, the effect of one Cu^{II} ion out of ~10 Cu^I on the Cu K-edge would be discernible (a slight shift of ~0.1 eV). There is no apparent effect of replacing Tyr374 by Phe on the Cu K-edge in any of the Y374F mutants (**Fig. S2** in APPENDIX).

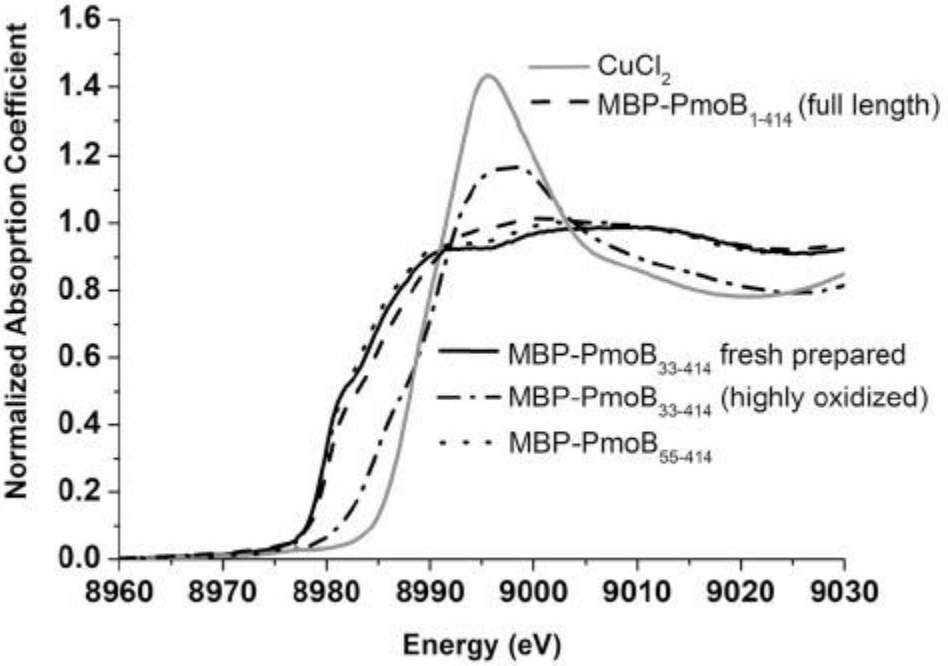

Fig. 21 Comparison of the X-ray absorption spectra of Cu K-edges observed for the copper ions in the membrane enriched with the full-length MBP-PmoB (*black dash),*), MBP-PmoB$_{33-414}$ (*black solid)*) and MBP-PmoB$_{55–414}$ (*black dot*) proteins, respectively.

After exposure to air for 18-24 h at 4°C, the MBP-PmoB$_{33\text{-}414}$ protein can become almost fully oxidized (with *ca.* 20% of the Cu^{I} remaining) (in *in black dash dot*).

3.2.6 Effects of exposure of the MBP-PmoB proteins to air on the copper ions

The copper ions of the full-length MBP-PmoB and the MBP-PmoB$_{55\text{-}414}$ proteins are stable even after exposure to air for 48 h at 4°C. The copper ions in the membranes with these proteins stay Cu^{I} over the duration of this experiment according to the Cu K-edge measurements. However, this is not the case with the *N*-truncated MBP-PmoB$_{33\text{-}414}$ protein. As shown in **Fig. 22**, the Cu K-edge shifts to higher energy by 2 or 3 eV, corresponding to the oxidation of about 70-80% of the copper ions in the protein. (We find that it is hard to maintain the *E. coli* membranes at *room temperature* for more than 12 h as the membranes begin to deteriorate.)

Since the bulk of the copper ions in the *E. coli* membranes with the various expressed MBP-PmoB proteins are Cu^{I}, these membranes should be EPR silent. Indeed, only very weak EPR signals ($d\chi''/dH$) can be elicited from these membranes as isolated. Also, no new EPR signals are detected for the full-length MBP-PmoB and MBP-PmoB$_{55\text{-}414}$ proteins even after prolonged exposure to air for 24 h at 4°C. However, under a similar exposure to air, a strong EPR spectrum corresponding to 4.5 Cu^{II} ions could be discerned for the membranes of the *N*-truncated PmoB$_{33\text{-}414}$ variant (**Fig. 22**, *upper panel*). The number of EPR visible copper ions is consistent with the shift observed in the XANES of the Cu K-edge mentioned earlier.

3.2.7 Ferricyanide treatments of the MBP-PmoB fusion proteins in the

purified membranes of the *E. coli* K12 TB1 cells

The EPR spectrum recorded for the membranes of the *N*-truncated $\mathrm{PmoB}_{33\text{-}414}$ variant after prolonged exposure to air for 24 h at 4°C is a superposition of signals from different copper sites and is typical of a nearly axial square planar $\mathrm{Cu^{II}}$ coordination with slight rhombic distortion. Upon treatment of these oxidized copper species with 1 equiv. of $\mathrm{Fe(CN)_6}^{3-}$ (1 equiv. = 1 protein), we see a dramatic change in the spectrum with loss of Cu nuclear hyperfine splittings in the $g_{\parallel}$ region with apparent concomitant loss of intensity corresponding to *ca.* one copper ion (**Fig. 22**, *upper panel*). The new signal can be assigned to the formation of a mixture of $[\mathrm{Fe(CN)_6}^{3-}](\mathrm{Cu}^{2+})_n$ (n = 1–4) adducts.[11, 36] With further additions of $\mathrm{Fe(CN)_6}^{3-}$ up to 10 equiv., we see additional EPR intensity corresponding to one to two additional $\mathrm{Cu^{II}}$ ion, suggesting oxidation of one or two $\mathrm{Cu^{I}}$ ions in the MBP-$\mathrm{PmoB}_{33\text{-}414}$ to form the $[\mathrm{Fe(CN)_6}^{4-}](\mathrm{Cu}^{2+})$ adduct[11, 36, 40] (**Fig. 22**, *lower panel*).These observations indicate that some of the $\mathrm{Cu^{II}}$ ions in the MBP-$\mathrm{PmoB}_{33\text{-}414}$ protein are solvent exposed. In contrast, none of these observations are noted for membranes of the full-length MBP-PmoB and the MBP-$\mathrm{PmoB}_{55\text{-}414}$ proteins. Only a very low level of $\mathrm{Cu^{II}}$ (significantly less than one $\mathrm{Cu^{II}}$ ion) is detected for membranes of the full-length MBP-PmoB and the MBP-$\mathrm{PmoB}_{55\text{-}414}$ proteins. This difference in behavior of the PmoB variants towards oxidation by $\mathrm{O_2}$ or $\mathrm{Fe(CN)_6}^{3-}$ is dramatic. (The EPR intensities obtained from double integration of the EPR spectra are summarized in Table S1 in Supplementary information.)

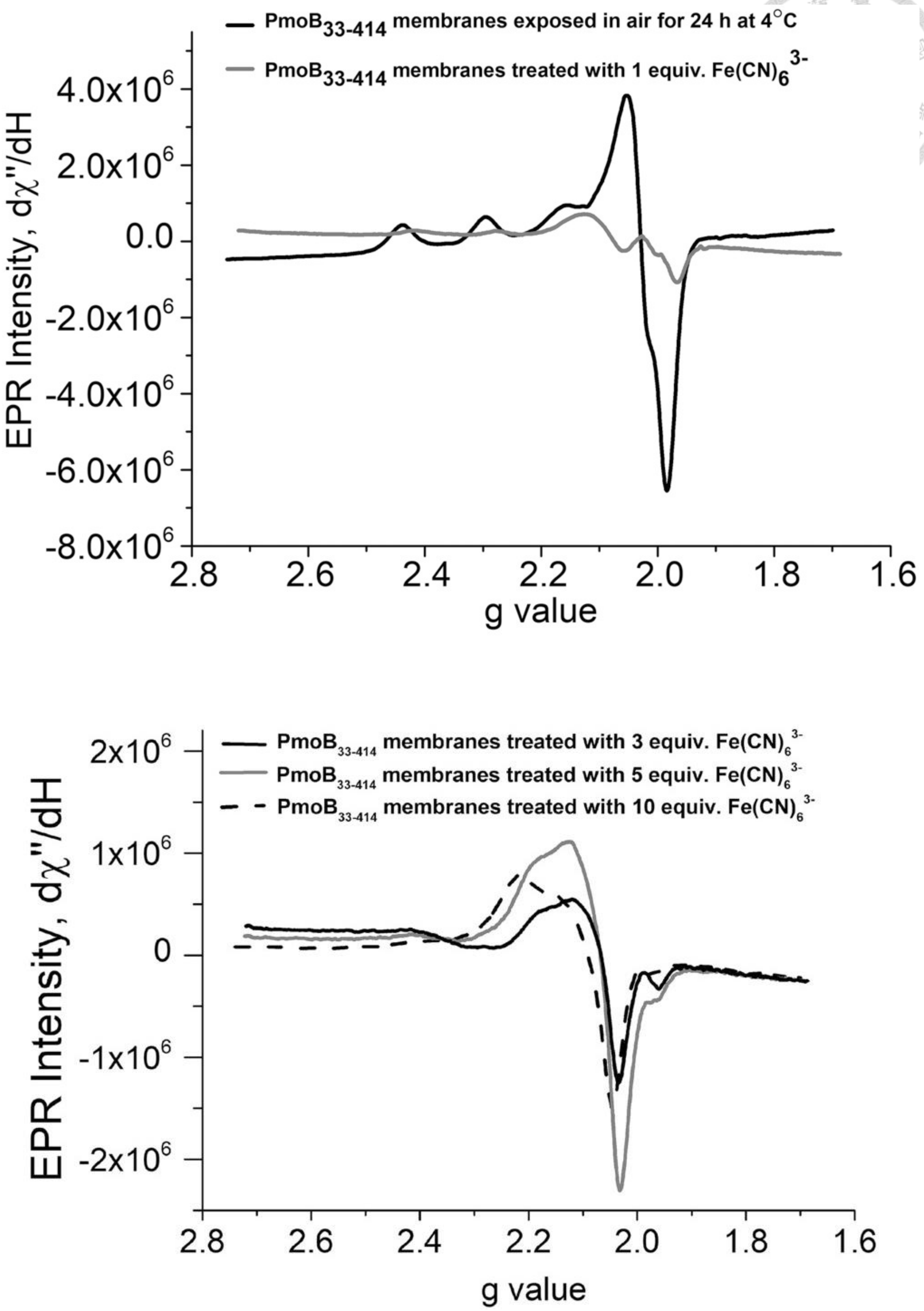

Fig. 22 EPR spectra of the purified PmoB$_{33\text{-}414}$ membranes and effects from $Fe(CN)_6^{3-}$ treatment. *Upper panel:* Comparison of the EPR spectrum obtained after the

addition of 1 equiv. of $Fe(CN)_6^{3-}$ (*gray*) with that of the membranes that have been exposed to air for 24 h at 4°C (*black*). *Lower panel:* EPR spectra recorded after the addition of 3, 5, and 10 equiv. of $Fe(CN)_6^{3-}$.

3.2.8 Determination of the copper contents in the *E. coli* membranes of the MBP-PmoB fusion proteins by ICP-OES

Aliquots (0.2 ml) of protein samples were dissolved in 4.8 ml of saturated 65% HNO_3 solution (suprapure grade, Merck). The samples were digested in a MARS5 microwave digestion system (CEM Inc.). The temperature was stepped up incrementally from room temperature to 180°C in 15 min, and maintained at 180°C for another 15 min. The process of nitrate digestion was then terminated as the temperature was gradually lowered down to room temperature.

The digested samples were then diluted with 20 ml doubly distilled water (Millipore) prior to copper analysis. The copper contents of the digested samples were determined by Inductively Coupled Plasma-Optical Emission Spectrometry (ICP-OES) on a Varian 720-ES (Agilent Technology). The copper concentrations of the samples were determined by interpolating a linear plot of a series standard solutions of $Cu(NO_3)_2$ in 0.10 N HNO_3. A solution of 0.10 N HNO_3 in distilled water was used as the copper-free control.

3.2.9 Quantification of the level of Cu^I in the *E. coli* membranes of the N-truncated MBP-$PmoB_{55-414}$ fusion protein

doi:10.6342/NTU201903909

Cu^I concentrations were determined spectrophotometrically using bicinchoninic acid (disodium salt, Sigma Inc.) (BCA).[99] A large amount of BCA (20 mM) was added to the protein sample in order to shift the Cu^I binding equilibrium from the expressed protein to BCA. Under these conditions, all the Cu^I bound to the protein would be stripped off and become bound to the dye. The absorbance of the Cu^I-BCA complex obtained by ascorbate reduction of copper sulfate in the presence of BCA was used as a standard and shown to follow a linear correlation with Cu^I concentration in accordance with the Beer-Lambert's law in the range 10-100 μM Cu^I at the wavelength of 562 nm ($r^2 = 0.99$). No chromophoric absorption was observed in the presence of Cu^{II}, or in the absence of metal ions, upon the addition of BCA.

3.2.10 Purification and characterization of the expressed MBP-$PmoB_{55–414}$ fusion protein and the target $PmoB_{55–414}$ protein

The membrane pellets obtained for the *E. coli* cells grown with the recombinant plasmid pMAL-p2X*deSPpmob2* were re-suspended in TBS buffer (Tris buffer saline composed of 20 mM Tris-HCl, pH 7.4 and 200 mM NaCl) containing 10 mM sodium ascorbate and 0.5% *n*-dodecyl-β-D-maltoside (DDM) for 30 min at 4°C. The membrane solution was ultra-centrifuged (100,000 × *g*, 60 min, 4°C) again, and then was collected and filtrated through 0.45 μm filter. The target fusion proteins were absorbed on to an amylose resin column (New England Bioslabs®, Inc.) in TBS buffer containing 10 mM sodium ascorbate and 0.05% DDM, and were subsequently eluted with the same buffer containing 10 mM maltose.

To remove the MBP tag in the MBP-$PmoB_{55–414}$ protein, a 49 μl purified

doi:10.6342/NTU201903909

recombinant protein MBP-PmoB$_{55–414}$ (1 mg/ml) was mixed with 1.0 μl Factor Xa (1 mg/ml, New England BioLab) and incubated overnight at 4°C. The obtained PmoB$_{55–414}$ was eluted through an amylose resin column (New England Bioslabs®, Inc.) by TBS buffer containing 10 mM sodium ascorbate and 0.05% DDM.

The amount of the purified recombinant MBP-PmoB$_{55–414}$ fusion protein was identified by the detergent-compatible DC Protein Assay (Bio-Rad). The copper content of the purified PmoB$_{55–414}$ protein was determined by ICP-OES in exactly the same manner as for the purified *E. coli* membranes of the various MBP-PmoB fusion proteins, as described earlier.

3.2.11 EXAFS of the copper ions in the various MBP-PmoB fusion proteins expressed in the membranes of the *E. coli* cells

EXAFS analysis of the copper ions associated with the MBP-PmoB fusion proteins can be used to develop a preliminary glimpse of the average Cu-site structure, including possible ligand types, coordination number, and average Cu-ligand distances.

For direct comparison with results reported earlier on the spmoB protein,[15] we first describe our analysis on the MBP-PmoB$_{55–414}$ protein. This analysis is performed on the X-ray absorption data shown in **Fig. 23** for purified membranes of the MBP-PmoB$_{55–414}$ protein. The latter contains about 8 Cu^{I} ions. Best fitting of the EXAFS data suggests an average copper ion coordinated with 3 N/O at 2.11 Å, or 3 N/O at ~2.03 Å and 1 S at ~2.37 Å, when Cu−Cu scattering is not included in the analysis. (Fits 7 and 8 in **Table S3** and **Fig. S4**(e) and (f) in APPENDIX) When we include the Cu−Cu scattering, we obtain a better goodness-of-fit factor (R_{fit} value of

0.24%) with a disorder contribution to the Debye-Waller factor corresponding to the mean-squared displacement σ^2 (Å^2)= 0.005 (**Fig. 23**(c) and Fit 10 in **Table S3** in APPENDIX). Best fitting of the EXAFS data with this model suggests an average copper ion coordinated with 3 N/O at 2.04 Å, 1 S at 2.37 Å, and 0.15 Cu at 2.73 Å. According to this analysis, we surmise that only 1.2 copper ions are sensing Cu···Cu back-scattering in the PmoB protein containing a total of 8 copper ions. In other words, the occupancy of the dinuclear site (the **B** site) is about 60%. The Cu···Cu distance of 2.73 Å is substantially longer than the distance of 2.53 Å reported for the dicopper site in the spmoB protein.

Two or three copper ions with a ligand structure consisting of 3 or 4 N/O coordinated at 1.95 Å and 0.25 Cu at 2.53 Å have been inferred from analysis of the EXAFS data on the spmoB protein.[15] In this earlier work, there is no evidence of a strong Cu–S scattering. The E-cluster copper ions are not part of the spmoB protein, so there are many fewer copper ions contributing to the Cu K-edge absorption. The difference between the two preparations is that our PmoB proteins are over-expressed in the membranes of *E. coli* with Cu^{I} introduced endogenously, presumably with the assistance of the copper trafficking protein and copper metal chaperone(s) associated with the *E. coli* membranes,[93, 94] whereas in the case of the spmoB, the protein is heterologously expressed in *E. coli* and the copper ions are added as Cu^{II} exogenously.[15] Evidently, many of the Cu^{I} sites are not assembled with the latter construct.

(a) EXAFS Fit 3, PmoB$_{1\text{-}414}$ (including 0.3 Cu-Cu)

doi:10.6342/NTU201903909

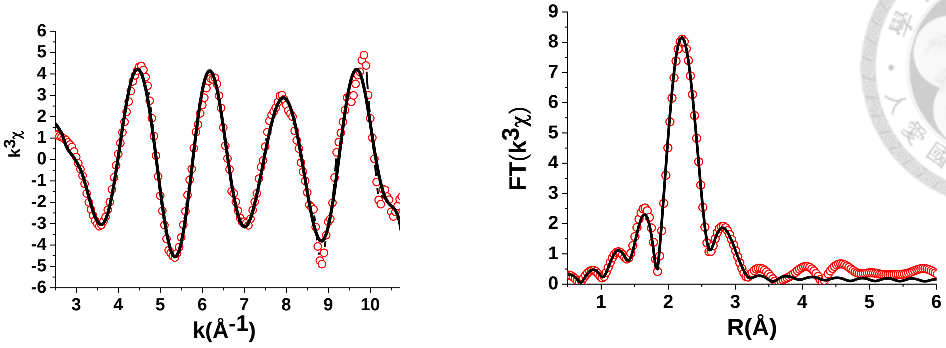

(b) EXAFS Fit 6, PmoB$_{33\text{-}414}$ (fully reduced) (including 0.4 Cu-Cu)

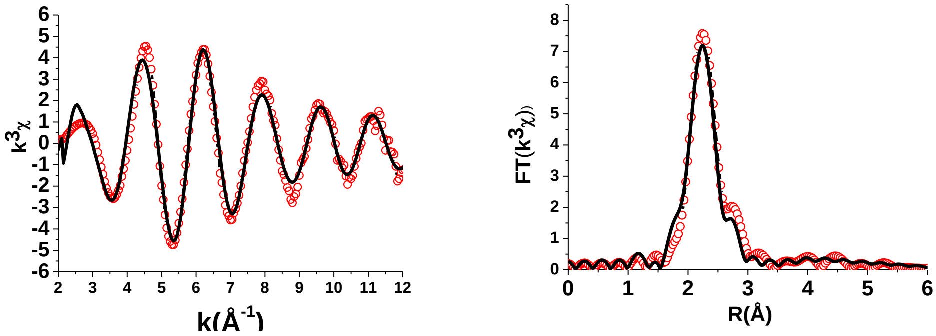

(c) EXAFS Fit 10, PmoB$_{55\text{-}414}$ (including 0.15 Cu-Cu)

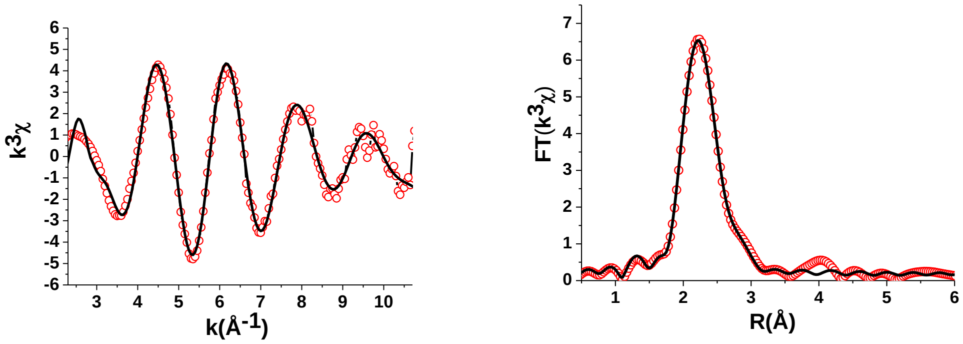

(d) EXAFS Fit 13, PmoB$_{33\text{-}414}$ Y374F Fit 3 (including 0.3 Cu-Cu)

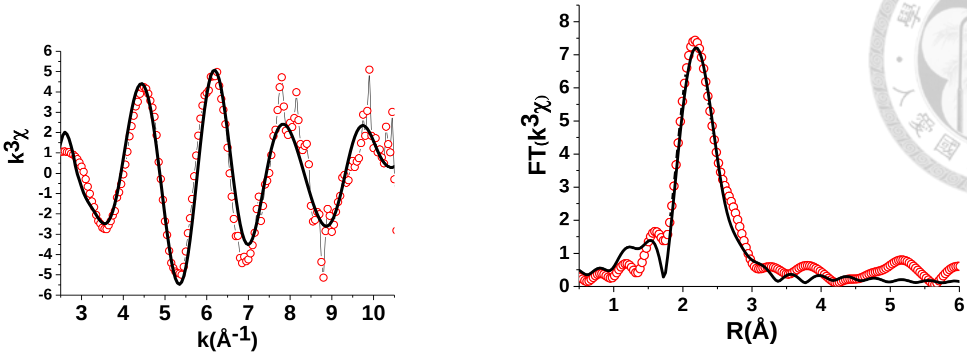

Fig. 23 The Cu EXAFS and their Fourier transforms of the MBP-PmoB proteins enriched in the cytoplasmic membranes of *E. coli* K12 TB1 cells: (**a**) the full length MBP-PmoB$_{1\text{-}414}$; (**b**) the fully reduced PmoB$_{33\text{-}414}$; (**c**) PmoB$_{55\text{-}414}$; and (**d**) PmoB$_{33\text{-}414}$ Y374F. *Left*: Cu EXAFS (*red* circles) and the corresponding best fits (*black* solid lines); *Right*: Phase shift corrected Fourier transforms of the Cu EXAFS (*red* circles) and the corresponding best fits *(black* solid lines).

In the present study, similar results are obtained for the membranes enriched with the full-length MBP-PmoB protein, the fully reduced MBP-PmoB$_{33\text{–}414}$ protein in the presence of ascorbate, and the MBP-PmoB$_{33\text{–}414}$ Y374F protein. The copper ions in these protein constructs are typically fully reduced. For these proteins, the first shell data (2.0 Å < R < 3.0 Å) in the Fourier transforms of $k^3\chi$ mainly arises from the back-scattering from ~3 ligated N/O atoms with the average distance of 2.09–2.11 Å. (**Fig. S4** and **Table S3** in APPENDIX). Including one additional Cu–S back-scattering at a distance of 2.31–2.37 Å can significantly improve the quality of the data fitting, lowering R_{fit} below 2%, the threshold of the confidence level. The Cu–O/N back-scatters distances are then shortened to 2.03–2.05 Å.((**Fig. S4** and **Table S3** in

doi:10.6342/NTU201903909

APPENDIX) When we include Cu−Cu scattering, we obtain an even much better goodness-of-fit, except in the case of PmoB$_{33\text{-}414}$ Y374F. (**Table S3**). The contribution of the Cu$\cdots$Cu scattering to the EXAFS varies from system to system, with coordination numbers of 0.3–0.4 and Cu$\cdots$Cu distances in the range 2.64−2.95 Å (**Fig. 24**, and **Table S3** in **APPENDIX**). The Cu$\cdots$Cu scattering contribution to the EXAFS decreases from 100% occupancy of the dicopper site in the membranes of the full-length MBP-PmoB$_{1\text{–}414}$ protein to *ca.* 60% in the case of the MBP-PmoB$_{55\text{–}414}$ protein.

Interestingly, upon exposure of the MBP-PmoB$_{33\text{–}414}$ membranes to air for 24 h at 4°C, we can fit the EXAFS data using the mononuclear and dinuclear copper core with the histidine coordination (**A** and **B** sites) inferred from the X-ray crystal structure of pMMO of *M. capsulatus* (Bath) [15, 24, 25, 100] as a structural model for these three copper ions. The best fit of the first shell fitting (1.9 Å < R < 3.0 Å) to the Cu EXAFS data yields an average copper ion with a ligand structure of 3−4 O/N atom (1.95−1.97 Å) and 1 S atom (2.26-2.49 Å) (**Fig. 24**, **Fig. S5** and **Table S4** in APPENDIX). The distances for the Cu−O/N scattering are shorter, and the distance corresponding to the Cu−S scattering has been lengthened significantly, a geometry that is more consistent with a typical Cu^{II} ion. A strong Cu$\cdots$Cu back-scattering feature with a contribution from two coppers at 2.79−3.13 Å also develops in the Fourier transformed amplitudes FT[$k^3\chi(k)$] in this system (**Fig. 24**, **S5** and **Table S4** in APPENDIX). This Cu$\cdots$Cu scattering is different from that noted earlier for the fully reduced MBP-PmoB$_{33\text{–}414}$ or the full-length protein. It is also not evident in the case of the MBP-PmoB$_{33\text{–}414}$ Y374F mutant. However, it is likely that the latter protein has lost one of the copper ions from the *N*-terminal domain, presumably the copper that is coordinated to H33 (or stabilized by Y374). With additional second, third and fourth shell back-scattering from His atoms

(2.0 Å < R < 4.0 Å) included in the analysis for each of the copper ions occupying the **A** and **B** sites (2–3 × 2.30–3.21 Å for Cu–C_{α} and 3 × 3.91–3 Å for Cu–C/N), the fitting range in *R* space can reach to 1.2–4.7 Å with an excellent R_{fit} (< 0.50%).

(a)EXAFS Fit 15

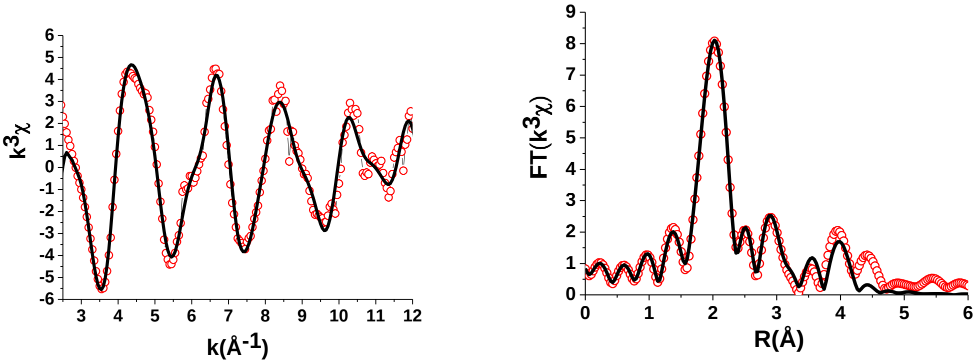

(b)EXAFS Fit 17

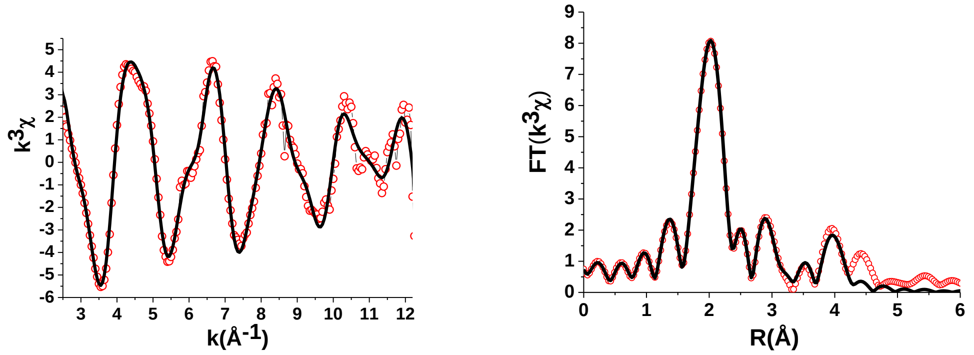

(c)EXAFS Fit 18

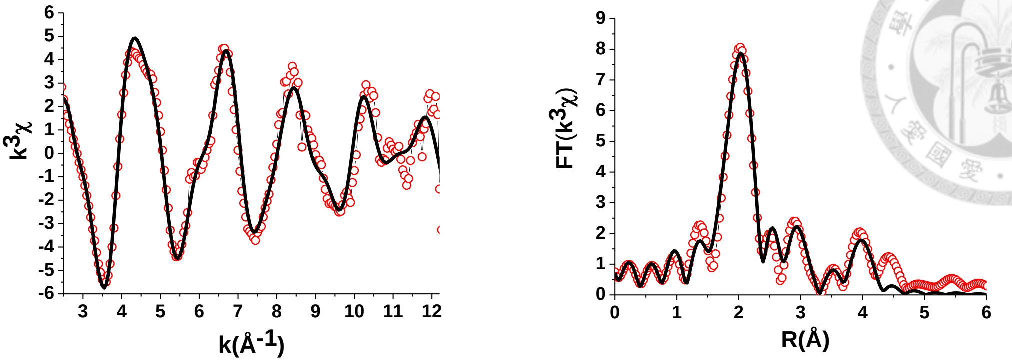

Fig. 24 The Cu EXAFS and their Fourier transforms of the MBP-PmoB$_{33\text{-}414}$ protein enriched in the cytoplasmic membranes of *E. coli* K12 TB1 cells after exposure to air for 24 h at 4°C. *Left*: Cu EXAFS (*red* circles) and the corresponding best fits (*black* solid lines); *Right*: Phase shift corrected Fourier transforms of the Cu EXAFS *(red* circles) and the corresponding best fits (*black* solid lines). (**a**) – (**c**) denote the three different better fits among the models used to fit the data, with the inclusion of Cu–S (Met), Cu–C$_{\alpha}$ (His), Cu–Cu and/or Cu–C/N (His) back-scatterings. All the parameters used in the data fitting are provided in Table S4 in APPENDIX.

With 9–10 copper ions, it would not be possible to obtain unambiguous information on the ligand structure of the individual copper cofactors. Nonetheless, certain general conclusions are evident from analysis of the EXAFS data. First, the copper ions in the reduced MBP-PmoB variants display ligand structures consisting of 2–3 N/O coordinated at 2.03–2.11 Å and 0.15–0.40 Cu coordinated at 2.64–2.95 Å (**Fig. 23, 8**, **S4** and **Table S3** in Supplementary information). When the MBP-PmoB$_{33\text{-}414}$ becomes oxidized by air, the Cu–N/O distances are shortened to 1.95–1.97 Å (**Fig. 24**, **S5** and **Table S4** in **APPENDIX**). Taken together, these data are consistent with an earlier EXAFS study on a preparation of pMMO containing only 2–3 copper ions per protein, which also showed a lengthening of the average Cu–N/O bond lengths upon reduction of the copper ions, concomitant with the increase of the Cu–Cu distance from 2.51 to 2.65 Å.[100] A more recent Cu EXAFS study of the as-isolated pMMO has revealed also primary coordination of 2 N/O ligands at 2.09 Å and 0.3 Cu coordinated at 2.66 Å.[15] We offer these comparisons here to lend support to the presumption that the Cu^I ions observed in the present study of the recombinant membrane-bound PmoB variants are indeed related to the PmoB subunit in the intact pMMO. Second, many of the copper ions must have a ligand coordination consisting of 2–3 N/O and 1 S, with the latter coming from a Met S given the Cu-S distance of ~2.36 Å and the high redox potential of these copper ions. The PmoB subunit is unique with its propensity of Met residues, as well as the abundant number of Glu and Asp residues.(**Table S2** in **APPENDIX**) Third, there are a pair of copper ions that are in sufficiently close proximity for Cu···Cu back-scattering in the Cu EXAFS, with a Cu···Cu distance of ~2.7 Å in the reduced state and the capability to form a well-defined μ-(η^2:η^2)-peroxo dicopper (II) or a bis-(μ-oxo)-dicopper(III) structure, presumably with a Cu···Cu distance >3.0 Å,[101-104][1] upon reaction with O_2, as observed upon exposure of the MBP-$PmoB_{33–414}$ membranes to air. One of these copper ions are presumably associated with His33 in the *N*-terminal domain, though the involvement or participation of Y374 from the *C*-terminal domain cannot be ruled out (**Fig. 25**).[98] In any case, we see oxidation of copper ions only in the case of the MBP-$PmoB_{33–414}$, not for the full length MBP-PmoB protein, even though there is evidence for Cu···Cu back-scattering in the Cu K-edge EXAFS spectrum of the full-length MBP-PmoB membranes, with an average coordination number of 0.30 and a Cu···Cu distance of 2.70 (R_{fit} = 0.11%), or a total occupancy of two copper ions (Fit 3 in **Table S3** and **Fig. 23(b)**). Evidently, the details of the dicopper site must be dependent on whether or not

doi:10.6342/NTU201903909

the leader sequence is part of the *N*-terminal domain, whether or not the Y374 plays a role in this structure, and any O_2 chemistry is associated with the site.

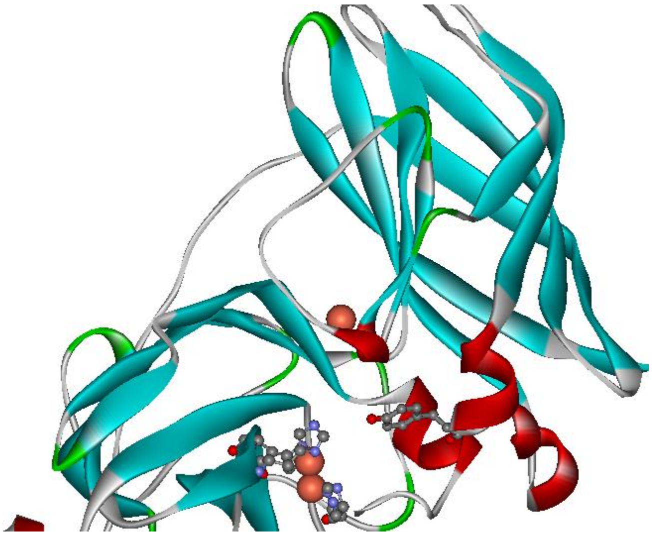

Fig. 25 The two coppers located at the **B** site of the PmoB subunit according to the X-ray crystal structure of pMMO reported by R. L. Lieberman, A. C. Rosenzweig [7], with His33, His137, His139, and Tyr374 highlighted. The single copper ion occupying the mononuclear **A** site is also shown at the top.

3.2.12 Measurements of specific activities toward hydrocarbon oxidation mediated by the MBP-PmoB fusion proteins expressed in the *E. coli* membranes

We have examined the specific activities of our *E. coli* membranes with the various expressed MBP-PmoB proteins for their abilities to hydroxylate methane to methanol and epoxidize propene to propylene oxide at 45°C. No activity is observed for methane oxidation mediated by the *E. coli* membranes with either the expressed MBP-PmoB$_{33-414}$ or the MBP-PmoB$_{55-414}$ proteins, regardless of whether duroquinol

doi:10.6342/NTU201903909

(0.35 M) or NADH (5 mM) is used as the reductant to drive the catalytic turnover. No chemical conversion of propene is detected with NADH (5 mM) as well. However, we find that propene is converted to acrolein quite efficiently both in the cases of MBP-PmoB$_{33\text{-}414}$ and MBP-PmoB$_{55\text{-}414}$ enriched membranes when the catalytic turnover is driven by 0.35 M duroquinol.(**Table S5** in APPENDIX.) However, these specific activities do not correspond with the copper contents of the recombinant PmoB variants. We surmise that the production of acrolein from propene is mediated by varying amounts of Cu_2O[105] that might be sequestered by the lipid headgroups of the *E. coli* membranes.

3.2.13 Production of H_2O_2 by the *E. coli* membranes enriched with the MBP-PmoB proteins

Interestingly, we observe significant production of H_2O_2 with the MBP-PmoB$_{33\text{-}414}$ membranes, the *N*-truncated PmoB mutant that reacts with O_2 or air (**Fig. 26**). We incubate these membrane suspensions in air at 4°C and measure the amounts of H_2O_2 released at hourly intervals by QUANTOFIX Peroxide 25 test strips. (The H_2O_2 production is quite facile under physiological conditions. Accordingly, we have monitored the production of H_2O_2 at 4°C in order to examine the process more deliberately.) The amounts of H_2O_2 detected peak after 6 h of incubation and correspond to 5−10 mg l^{-1}; when the incubation is continued for another 2 h, the amounts of H_2O_2 detected drop to *ca*. 2−2.5 mg l^{-1}, indicating decomposition of the H_2O_2 produced with time, as expected. Based on the amounts of the recombinant MBP-PmoB$_{33\text{-}414}$ protein in the membranes, the H_2O_2 detected after 6 h incubation

doi:10.6342/NTU201903909

corresponds to 2.8 molecules per $PmoB_{33\text{-}414}$, which would require draining *ca*. 6 reducing equivalents from the PmoB protein. Minor production of H_2O_2 is detected in the case of the $MBP\text{-}PmoB_{55\text{-}414}$ protein only when these membranes are incubated up to 25 h. We do not observe any H_2O_2 generated by the membranes enriched with the full-length MBP-PmoB protein.

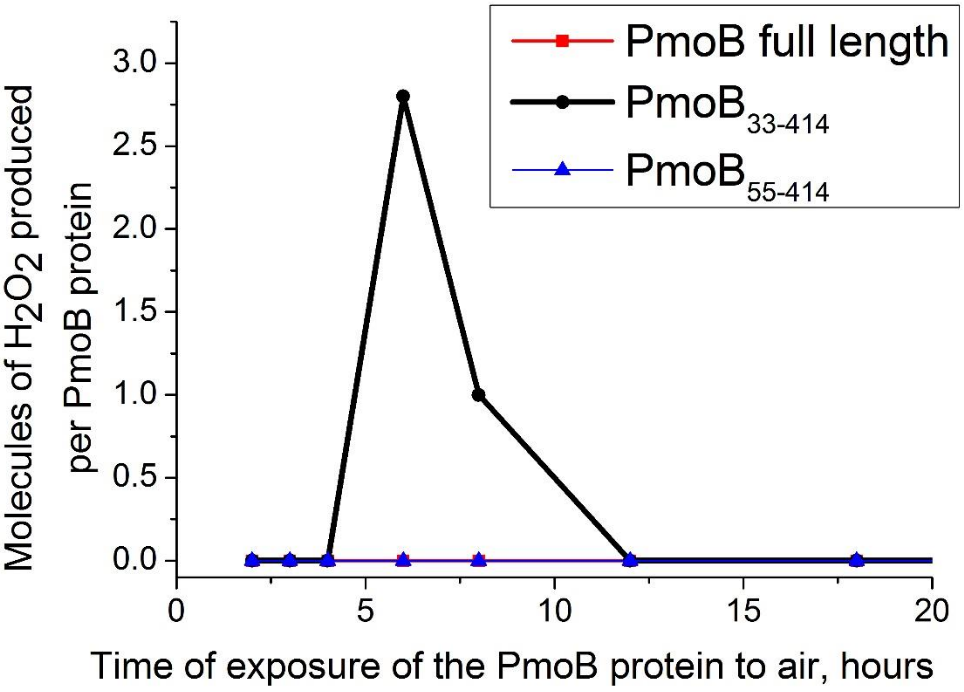

Fig. 26 Time course of the production of H_2O_2 from the MBP-PmoB enriched membranes upon incubation of the membrane suspensions in air at 4°C.

3.3 Discussion

The structure of pMMO is enormously complex. Although crystal structures of the pMMO from several species have been known for some years, we have, at this juncture, only the protein fold with 3 copper ions in the PmoB subunit and a Zn^{2+}/Cu^{2+} site in the

doi:10.6342/NTU201903909

PmoC subunit.[24, 35, 106] After years of debate, it is becoming increasingly evident that the catalytic site of the enzyme is a unique tricopper cluster embedded within the transmembrane domain sequestered by residues from the other two subunits, namely, PmoA and PmoC.[33, 95] The three copper ions forming the tricopper cluster were harshly lost during the purification of the protein for crystallization and X-ray analysis.[6, 10, 12] In addition to the three copper ions that form the **A** and **B** sites, there are still many copper ions associated with the PmoB subunit.[12, 28, 36, 39]

In this study, we have developed a strategy that is capable of expressing and assembling the PmoB subunit with all the copper ions in the membranes of a bacterial host cell. This approach has allowed us to undertake a more in-depth scrutiny of the different copper centers: the mononuclear copper (**A** site), the copper ions that form the dicopper center (**B** site) as well as the remaining copper ions that have been implicated in the *C*-terminal domain of the PmoB subunit. To accomplish this, we have cloned and over-expressed in the membranes of *E. coli* K12 TB1 cells, the full-length PmoB protein, two *N*-truncated PmoB proteins, and several of their mutants, as fusion proteins to the maltose binding protein. As a copper tolerant strain, the *E. coli* K12 TB1 cells might be equipped with the copper trafficking protein Cop A to insert Cu^I ions into a membrane-bound protein subunit, [39, 92, 107] if these Cu^I ions were intended to be part of the protein-structure design with a specific function in mind.

Indeed, one of the most significant findings that have emerged from the present work is that the PmoB subunit is a Cu^I protein with many copper-binding sites. This is the case for all the MBP-PmoB proteins expressed in the membranes. Second, the functioning PmoB protein contains as many as 9−10 copper ions, as previously reported for the PmoB subunit in the *holo* pMMO. [11, 27, 28, 36, 37] In addition to the three total copper ions occupying the **A** and **B** sites in the *N*-terminal domain, there are *ca.*

doi:10.6342/NTU201903909

6−7 Cu^{I} associated with the *C*-terminal domain of the PmoB subunit.

It has been reported that the recombinant spmoB protein with the dinuclear copper site (the **B** site) is capable of oxidizing methane to methanol and propene to propylene oxide in the presence of O_2. In the activity assays, a high dose of duroquinol (1.0 M) is supplemented to provide the reducing equivalents for the chemical transformation. However, a high dose of duroquinol would form a sol-gel mixture to form the wandering protein conformation actually. The N-terminal and C-terminal sub-domains are anchored in the membrane and the A and B site copper ions are constrained to facilitate ligation of the CuI at the A site with Gln404 from the C-terminal sub-domain. In the case of the spmoB construct, the N- and C-terminal domains are linked by only a short Gly-Lys-Gly-Gly-Gly (GKGGG) linker and the coordination of the Cu^{I} at the A site with Gln404 is disrupted.

Interestingly, the copper ions that form the **B** site in the MBP-PmoB$_{33–414}$ protein can be oxidized to Cu^{II} and produce H_2O_2 after exposure of these purified membranes to air overnight at 4°C. Concomitant with the oxidation of these copper ions, we detect Cu···Cu back-scattering in the Cu EXAFS of the MBP-PmoB$_{33–414}$ protein, just as has been reported for the spmoB protein by the Northwestern group.[15] Almost all the E-cluster copper ions are also oxidized by this treatment, releasing 2.8 molecules of H_2O_2 per PmoB protein.

Although it is apparent that the copper ions occupying the **A** and **B** sites in the full length MBP-PmoB$_{1–414}$ protein cannot be oxidized in the presence of air, we do observe a weak Cu···Cu backscattering contribution, corresponding to total occupancy of a dicopper site to the Cu EXAFS in the fully reduced full-length MBP-PmoB protein. Similarly, the MBP-PmoB$_{55-414}$ protein remains fully reduced upon exposure to air **(Fig. 21**), but the Cu EXAFS for these membranes are well fitted with a Cu···Cu

doi:10.6342/NTU201903909

back-scattering contribution corresponding to 60% occupancy of the dicopper site **(Fig. 23(c)**). In fact, regardless of whether the PmoB subunits are expressed with the amino acid residues 14−14, 33−414, or 55−414, Cu···Cu back-scattering is observed for the recombinant as-isolated MBP-PmoBs in the *E. coli* membranes, all comparable to the recent EXAFS data reported on pMMO in its reduced and as-isolated forms.[15, 106] Thus, it is evident that the various variants of the PmoB subunit fused with MBP that we have heterologously over-expressed in the *E. coli* membranes can serve as a functional model for the study of the PmoB subunit in pMMO. If so, the **B** site is indeed a dicopper center and not a mononuclear site as recently proposed.[106]

The MBP-PmoB$_{33-414}$ protein differs from the full-length MBP-PmoB protein in that the *N*-terminal leader sequence is not included in the *N*-truncated sequence. As a leader sequence, these amino acids should not be part of the functional pMMO, and in fact, this part of the PmoB sequence does not appear in the X-ray structures of the pMMO proteins reported to date.[24-26] Given the different reactivity between the MBP-PmoB$_{33-414}$ and full-length MBP-PmoB proteins towards O_2, there must be a structural basis for the dramatic difference in the biochemistry. In the case of MBP-PmoB$_{33-414}$ construct, and for the spmoB protein as well,[15] the peptide nitrogen and the imidazole ring nitrogen of H33 are simultaneously coordinating one of the copper ions occupying the **B** site to form the histidine brace together with the unusual dicopper site with the short Cu···Cu distance (*ca.* 2.5–2.7 Å). Since the dicopper site must open up before it can react with O_2, it is evident that excision of the leader sequence introduces structural flexibility to this part of the protein. In other words, the dicopper site could be part of a conformational switch that responds to O_2. As further evidence of this structural flexibility, with further truncation of the *N*-terminal domain to delete residues 33 to 54 to form the MBP-PmoB$_{55-414}$ construct, it is apparent that the

Y374 stabilizes the protein structure in this region by substituting for His33. Interestingly, the MBP-PmoB$_{55\text{-}414}$ variant shares more or less the same number of copper ions as the MBP-PmoB$_{33\text{-}414}$ protein even when H33 is no longer part of the construct (see **Table 2**). Thus, we surmise that Y374 stabilizes the copper normally associated with H33 and transforms the “binuclear” site into two uncoupled mononuclear centers so that the two coppers occupying the **B** site are now too constrained to react with O_2. We would expect the loss of this copper ion (possibly together with the other copper ion at the **B** site and the mononuclear copper at the **A** site) when Y374 is replaced by phenylalanine or serine. Indeed, we observe the loss of a total of *ca*. 3 coppers from the full-length MBP-PmoB protein in the corresponding MBP-PmoB$_{55\text{-}414}$ Y374F and Y374S mutants.

The remaining Cu^I ions of the PmoB subunit, *ca*. 6 or 7 in number, have very high redox potentials and cannot be oxidized directly by O_2. However, in a scenario in which the copper ions associated with the **B** site can react with O_2, as in the case of the membranes of the MBP-PmoB$_{33\text{-}414}$ protein, it is evident that these reducing equivalents can be gradually drained away from the E-cluster Cu^I ions. We surmise that the reaction of O_2 with the dicopper site can gate the flow of reducing equivalents from these Cu^I ions to produce the H_2O_2 observed.

Thus the PmoB subunit of pMMO might not only be a Cu^I sponge, namely just a reservoir of reducing equivalents for the turnover of the pMMO enzyme. The PmoB subunit can also be mechanically malleable. Examination of the PmoB amino acid sequence shows that the subunit is extremely rich in Met, Asp, and Glu (**Table S2** in **APPENDIX**), with many of these related residues even only one or two residues apart. With the large number of these hard ligands and the spatial distribution of these amino acids within the protein fold, it is possible to vary the ligand structures of the 6 or 7

doi:10.6342/NTU201903909

copper ions with a small expenditure of conformational energy. If so, it might be possible to exploit conformational linkage between the PmoB *N*-terminus and the transmembrane domain, including both the PmoA and PmoC subunits, to activate the dinuclear cluster for O_2 binding at the **B** site during turnover of the enzyme. The subsequent O_2 chemistry at the dicopper site can then change the conformation of the PmoB subunit and tune the redox potentials of the copper ions by a simple replacement of ligands, *e.g.*, substituting the Met by N/O of Asp or Glu. In this manner, the enzyme can gate the flow of electrons from the PmoB subunit to the catalytic site embedded within the transmembrane domain during turnover. The Cu EXAFS structural differences that we have observed between the fully reduced full-length MBP-PmoB protein and the “fully oxidized” MBP-PmoB$_{33-414}$ protein clearly indicates that this scenario is plausible. If so, the PmoB subunit can behave as a free energy transducer, the free energy for the mechanical-electrical transduction deriving from the free energy of O_2 binding to the two copper ions at the **B** site as well as the O_2 chemistry, augmented by interactions of the PmoB subunit with the PmoA/PmoC subunits. Although at this juncture we have no data that bears on the role of the mononuclear Cu^I at the **A** site in the overall function of the enzyme, it is conceivable that this copper ion can participate, at least in part, in the allosteric linkage between the *N*- and *C*-terminal sub-domains of the PmoB subunit to accomplish the mechanical-electrical transduction elicited by the dioxygen chemistry at the **B** site mentioned above. Interestingly, the ligands of this Cu^I ion are associated with amino acid residues from both the *N*- and C-terminal water soluble sub-domains (His38, His72 and Gln404) of the PmoB subunit.[24]

doi:10.6342/NTU201903909

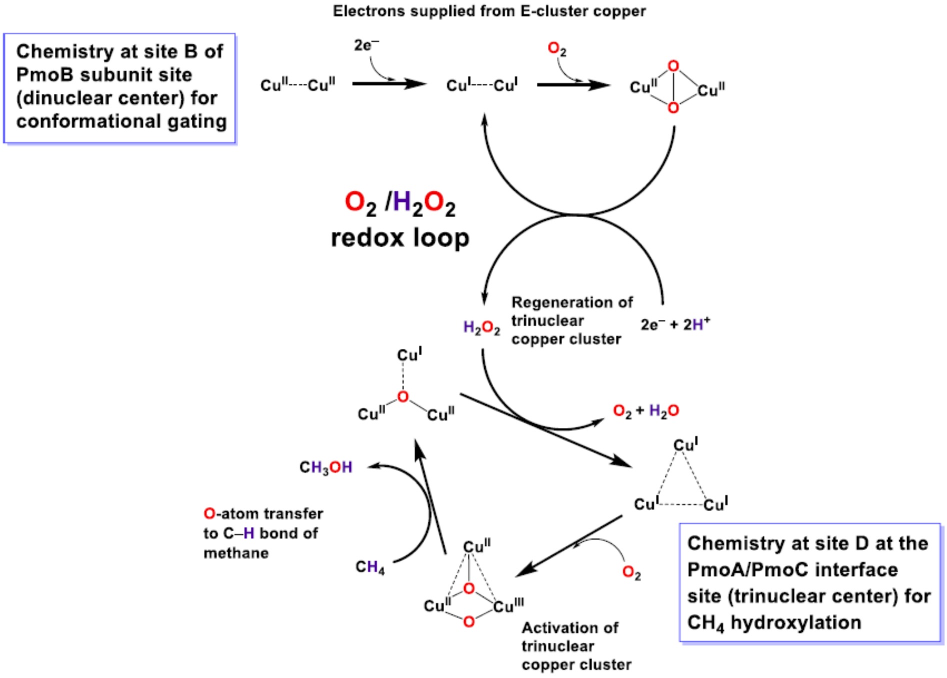

Fig. 27 Possible O_2/H_2O_2 redox loop between the dinuclear copper site (the B site) and the trinuclear copper site (the D site).

Earlier we invoked inter-cluster electron transfers between the E-cluster copper ions and the catalytic site as a way to complete the catalytic cycle during turnover of the pMMO.[6, 10] With the possibility of tuning the ligand structures of the E-cluster copper ions by the O_2 chemistry at the **B** site in the PmoB subunit, it seems that these inter-cluster electron transfers are feasible, despite the high reduction potentials of these copper ions in the resting state of the enzyme. However, another possibility in terms of mechanism is that the O_2 chemistry at the “dicopper” site is primarily intended to generate the μ–(η^2:η^2)-peroxo dicopper(II) species, as in polyphenol oxidases like tyrosinases and catechol oxidases,[108, 109] followed by release of a H_2O_2 molecule into a substrate/product channel leading to the catalytic site upon the uptake of two protons. This H_2O_2 molecule could be used to regenerate the tricopper $Cu^ICu^ICu^I$ catalytic site embedded within the transmembrane domain during turnover of the pMMO, by providing the two reducing equivalents required to reduce the $Cu^{I}Cu^{II}(O)Cu^{II}$ tricopper species formed after O-atom transfer to the organic substrate from the activated tricopper catalyst during the oxidative phase of the catalytic cycle. The two protons needed to form the H_2O_2 reductant would come from the water/proton channel(s) within the enzyme formed by the many Asp/Glu lining the interface between the PmoA and PmoB subunits. This same strategy has recently been used to regenerate the tricopper catalyst for multiple turnovers in the development of biomimetic tricopper complexes for selective oxidation of methane and other small alkanes under ambient conditions.[33, 110-112] In principle, the O_2 chemistry mediated by the dicopper species at the **B** site could lead to the formation of the bis-(μ-oxo)-dicopper(III) species, but this scenario would require two additional reducing equivalents from the E-cluster domain.

3.4 Experiments

3.4.1 *Quantification of the total membrane proteins from the E. coli cytosolic membranes*

membrane pellets obtained for the *E. coli* cells grown with the recombinant plasmid pMAL-p2X were re-suspended in TBS buffer (Tris buffer saline composed of 20 mM Tris-HCl, pH 7.4) as mentioned in section 2.5. The total amounts of membrane proteins in the sample were measured by the preconfigured method for Protein A280 of the NanoDrop™ 2000 from Thermo Scientific™.

doi:10.6342/NTU201903909

3.4.2 Raising polyclonal antibodies against the recombinant PmoB$_{55–414}$ protein

Polyclonal antibodies against the PmoB subunit were raised in rabbit by GeneTex Inc., Taipei. Polyclonal antiserum was obtained by injecting rabbits with the copper-enriched PmoB$_{55–414}$ protein**.** (Each protein contains *ca*. 5 copper ions (*vide infra*).) The first immunal injection consisted of the purified PmoB$_{55–414}$ protein (0.5 mg) and lipopolysaccharide (1:1 volume); only purified PmoB$_{55–414}$ protein was used in subsequent burst injections. Purification of the polyclonal antibodies was carried out by the affinity purification approach. Series dilution was used to determine the limits of detection in the antibody titer tests.

3.4.3 Western blotting with rabbit anti-PmoB$_{55–414}$ antibodies (polyclonal) and anti-MBP monoclonal antibody/HRP conjugates

Method 1

The pMMO in the membranes of *M. capsulatus* (Bath), the recombinant PmoB$_{55–414}$ proteins in the membrane pellets, and purified pMMO[28] were analyzed by 12% SDS-PAGE and then transferred to polyvinylidene difluoride (PVDF) membranes. The membranes were blocked with 5% skim milk for 12 h at 4°C and then incubated with rabbit *anti*-PmoB$_{55–414}$ antibodies (1:40,000) and supplemented with a second antibody, the commercial goat *anti*-rabbit immunoglobin antibody (Sigma) conjugated with alkaline phosphatase (1:20,000), to spot the MBP-PmoB$_{55–414}$ fusion-protein in the

PVDF membranes. After hybridization at room temperature for 1 h, the membranes were washed by 3 × 25 ml phosphate buffered saline (PBS, pH 7.4, 137 mM NaCl, 2.7 mM KCl, 10 mM Na_2HPO_4 and 2.0 mM KH_2PO_4), and incubated with the alkaline phosphatase substrate, nitro-blue tetrazolium chloride/5-bromo-4-chloro-3’-indolylphosphate *p*-toluidine salt (NBT/BCIP, Thermo Scientific^{TM} Pierce) for the identification of the PmoB subunit (purple-black precipitate). After separation of the pMMO subunits on SDS-PAGE, the subunit B of pMMO could be also identified in this manner without any specialized equipment for visualization. Both the PmoB subunit isolated from the *holo* pMMO and the recombinant $PmoB_{55–414}$ were readily recognized on SDS-PAGE by the rabbit anti-PmoB antibodies, with molecular weights of 45 and 98 kDa, respectively. The pre-stained protein markers used in the SDS-PAGE were obtained from EZColor II^{TM} Prestained Protein Marker (EZ BioResearch LLC).

Method 2

The proteins in the membrane pellets were separated by 10% SDS-PAGE. Proteins on the poly-acrylamide gel were transferred to 0.45 μm Hybond-P hydrophobic PVDF membranes (GE Healthcare), and the membranes were blocked by 5.0% skim milk/TBS (blocking solution) at room temperature for 2.0 h. After blocking, the PVDF membranes were washed with 1.0% skim milk/TBS and then incubated with *anti*-MBP monoclonal antibody, horseradish peroxidase (HRP) conjugates (New England Biolabs, Inc.) in 1/5000 dilution at room temperature for 1.0 h. Before enhanced chemiluminescence (ECL) analysis, the PVDF membranes were washed with TBST (TBS containing 0.10% (v/v) Tween^{TM} 20) three times. HRP substrate (Immobilon^{TM} Western, Millipore, Corp.)

doi:10.6342/NTU201903909

was then added to the PVDF membranes and the target proteins spotted by the luminescence elicited by ECL™ (Western blotting kit from GE Healthcare consisting of the membrane blocking agent, anti-rabbit and mouse IgG) using a CCD camera (BioSpectrum® AC Imaging System, UVP, Inc.).

For quantitation of the recombinant target full-length MBP-PmoB, MBP-PmoB$_{33–414}$, and MBP-PmoB$_{55–414}$ proteins expressed in the *E. coli* K12 TB1 cells, including the various mutant proteins studied, we determined the protein concentrations in the various membranes by Western blotting following the established protocol [26]. MBP5 protein (New England Bioslabs®, Inc.) was used to set up the calibration curve.

3.4.4 Determination of the copper contents in the *E. coli* membranes of the MBP-PmoB fusion proteins by ICP-OES

Aliquots (0.2 ml) of protein samples were dissolved in 4.8 ml of saturated 65% HNO_3 solution (suprapure grade, Merck). The samples were digested in a MARS5 microwave digestion system (CEM Inc.). The temperature was stepped up incrementally from room temperature to 180°C in 15 min, and maintained at 180°C for another 15 min. The process of nitrate digestion was then terminated as the temperature was gradually lowered down to room temperature.

The digested samples were then diluted with 20 ml doubly distilled water (Millipore) prior to copper analysis. The copper contents of the digested samples were determined by Inductively Coupled Plasma-Optical Emission Spectrometry (ICP-OES) on a Varian 720-ES (Agilent Technology). The copper concentrations of the samples were

doi:10.6342/NTU201903909

determined by interpolating a linear plot of a series standard solutions of $Cu(NO_3)_2$ in 0.10 N HNO_3. A solution of 0.10 N HNO_3 in distilled water was used as the copper-free control.

3.4.5 Quantification of the level of Cu^I in the *E. coli* membranes of the N-truncated MBP-$PmoB_{55\text{-}414}$ fusion protein

Cu^I concentrations were determined spectrophotometrically using bicinchoninic acid (disodium salt, Sigma Inc.) (BCA). A large amount of BCA (20 mM) was added to the protein sample in order to shift the Cu^I binding equilibrium from the expressed protein to BCA. Under these conditions, all the Cu^I bound to the protein would be stripped off and become bound to the dye. The absorbance of the Cu^I-BCA complex obtained by ascorbate reduction of copper sulfate in the presence of BCA was used as a standard and shown to follow a linear correlation with Cu^I concentration in accordance with the Beer-Lambert's law in the range 10-100 μM Cu^I at the wavelength of 562 nm (r^2 = 0.99). No chromophoric absorption was observed in the presence of Cu^{II}, or in the absence of metal ions, upon the addition of BCA.

3.4.6 Purification and characterization of the expressed MBP-$PmoB_{55–414}$ fusion protein and the target $PmoB_{55–414}$ protein

The membrane pellets obtained for the *E. coli* cells grown with the recombinant plasmid pMAL-p2X*deSPpmob2* were re-suspended in TBS buffer (Tris buffer saline composed of 20 mM Tris-HCl, pH 7.4 and 200 mM NaCl) containing 10 mM sodium

doi:10.6342/NTU201903909

ascorbate and 0.5% *n*-dodecyl-β-D-maltoside (DDM) for 30 min at 4°C. The membrane solution was ultra-centrifuged (100,000 × *g*, 60 min, 4°C) again, and then was collected and filtrated through 0.45 μm filter. The target fusion proteins were absorbed on to an amylose resin column (New England Bioslabs®, Inc.) in TBS buffer containing 10 mM sodium ascorbate and 0.05% DDM, and were subsequently eluted with the same buffer containing 10 mM maltose.

To remove the MBP tag in the MBP-PmoB$_{55–414}$ protein, a 49 μl purified recombinant protein MBP-PmoB$_{55–414}$ (1 mg/ml) was mixed with 1.0 μl Factor Xa (1 mg/ml, New England BioLab) and incubated overnight at 4°C. The obtained PmoB$_{55–414}$ was eluted through an amylose resin column (New England Bioslabs®, Inc.) by TBS buffer containing 10 mM sodium ascorbate and 0.05% DDM.

The amount of the purified recombinant MBP-PmoB$_{55–414}$ fusion protein was identified by the detergent-compatible DC Protein Assay (Bio-Rad). The copper content of the purified PmoB$_{55–414}$ protein was determined by ICP-OES in exactly the same manner as for the purified *E. coli* membranes of the various MBP-PmoB fusion proteins, as described earlier.

doi:10.6342/NTU201903909

Chapter 4 Regulation of Anaerobic Nitrate and Nitrite Respiratory by the Iron Nitrosyl Complexes in FNR

4.1 Background

FNR protein (the regulator of Fumarate Nitrate Reductase) is an oxygen sensing transcriptional factor. It exhibits [4Fe-4S]$^{2+}$ cluster in *Escherichia coli* (*E. coli*) under anaerobic condition and possesses a dimeric form. At this stage, the *E. coli* undergoes anaerobic respiratory pathways. In contrast, with the presence of molecular oxygen, its [4Fe-4S]$^{2+}$ cluster in each of the monomers will be dissociated into a [2Fe-2S]$^{2+}$ cluster. The corresponding form of FNR protein would dissociates from the downstream regulation region of *fnr* and cause significant retardation of FNR protein expression.[74, 113, 114]

FNR proteins have also been considered as a significant negative regular for *hmp* gene transcription. Hmp protein is a flavohaemoglobin protein and crucial for detoxification of high-level NO (nitric oxide) production. In aerobic environment, Hmp protein behaving like NO oxygenase convert NO to nitrate[115, 116] whereas the corresponding proteins produce nitrous oxide under anaerobic growth.[116, 117] It was believed that the nitrosylated FNR protein does not response to the anaerobic growth where the Hmp proteins could be over-produce to dissimilate the NO stress.

The FNR protein recognizes the consensus sequences of TTGAT-N4-ATCAA. For

doi:10.6342/NTU201903909

the promoter region of *hmpA*, the recognition site is located at +5.5 of TTGATatacATCAA.[79] In the region of *fnr* promoter, both the upstream site (TTAAGggttTTCAA) centered at bp +103.5 and downstream site (TTGACaaatATCAA) centered at bp +0.5 are identified to be potentially bound with regulatory proteins presumably with various forms of FNR.[113]

NO was considered as an O_2-equivalent effector in non-heme system. Both of the gases are diatomic molecules. In *E. coli*, transcriptional factors containing iron-sulfur clusters such as SoxR[118, 119] (superoxide and redox cycling compounds responsive protein) or FNR[120-122] protein are sensitive to these molecules. NO-treated and oxidized SoxR by redox recycle compounds seem revealed similar property in DNA regulation. However, it is mostly considered that FNR after nitrosylation can be just like oxidized FNR losing its function as a repressor. Nevertheless, we show that FNR can sense nitric oxide to change its DNA affinity and specificity. Poole et. Al., proposed that nitrosylated FNR may own certain function but its mechanism is still unknown.[80, 123]. Our study herein has enlightened that the FNR protein in *E. coli* after nitrosylation by the growth in anaerobic nitrate respiratory can promote the expression of FNR protein itself.

4.2 Results

4.2.1 Preparation of FNR proteins via Recombinant DNA Technology

We employed the recombinant DNA technology to obtain the full length FNR protein by inserting the corresponding encoding DNA into the NdeI/XhoI of *pET22b*

doi:10.6342/NTU201903909

(Novagen EMD Chemical Inc.) with 6 × His·tag. The validation of the recombinant FNR protein was verified by the encoded DNA sequence of the inserted oligonucleotides and its molecular weight confirmed from 1D SDS-PAGE. After the growth of FNR protein anaerobically, we purified the corresponding protein through a His Trap HP column (GE Healthcare) (1-mL) into homogeneity (purity: 98% by SDS PAGE analysis).

4.2.2 Exploration of the physiological role of FNR protein under the nitrate respiration in anaerobic growth

The core structure of FNR protein is presented as an iron-sulfur protein. It was believed that *E. coli* would dissimilate the nitrate salt to nitric oxide under the anaerobic respiration. Namely, it is possible that there would be high concentration of free nitric oxide accumulated within the anaerobic nitrosative stresses,[123] which may presumably exerting the formation of protein bound nitrosylated complexes in the proteins containing iron-sulfur clusters. On the basis of these, we would surmise that regulatory protein, FNR protein, could act as sensory protein responsive to the production of nitric oxide. Because of that, we constructed a recombinant *fnr* containing vector and transformed it into *E. coli*. The expression of recombinant FNR protein was performed to be fused with poly-histidine tag. Under the growth of anaerobic condition in the presence of nitrate salts, without the IPTG induction, we can observe both the wild type and recombinant FNR protein were significantly translated (**Fig. 28**). The recombinant FNR protein was enabled to be purified into homogeneity via a His Trap HP column (1-mL). The metal core structure of purified FNR was facilely characterized by EPR spectroscopic methods. Interestingly, as predicted in the presence of high steady state concentration of nitric oxide, the iron-sulfur cluster within

doi:10.6342/NTU201903909

the FNR protein would be converted to their protein bound nitrosylated iron complexes with paramagnetic features, $g_{av} = 2.03$ (**Fig.29**).

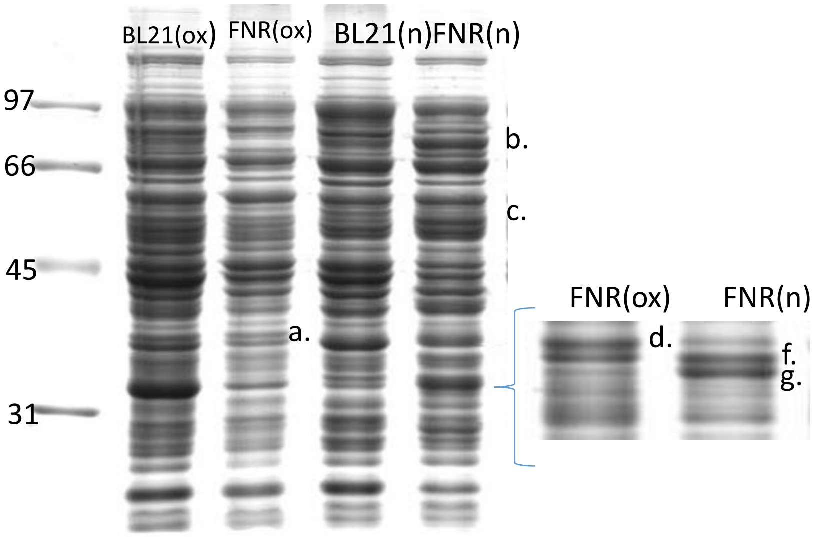

Fig. 28 The SDS Page data of the soluble protein profile in *E. coli* prepared by either the anaerobic with nitrate salt (n) or aerobic (ox) growth. The lanes of BL21 and FNR represent the *E. coli* BL21 (DE3) with and without the transformed *pET22bfnr* vector. The annotation of the referred protein bands at the 1-D gel electrophoresis in this figure is carried out by protein identification via protein mass fingerprint analysis. a. was H^+ ATPase F1 alpha subunit; b. was pyruvate formate lyase; c was pyruvate kinase ; d was MalE; e-g were FNR , which are all analyzed by TOF-MS^2 (All the mass fingerprint data provided in **Appendix**).

doi:10.6342/NTU201903909

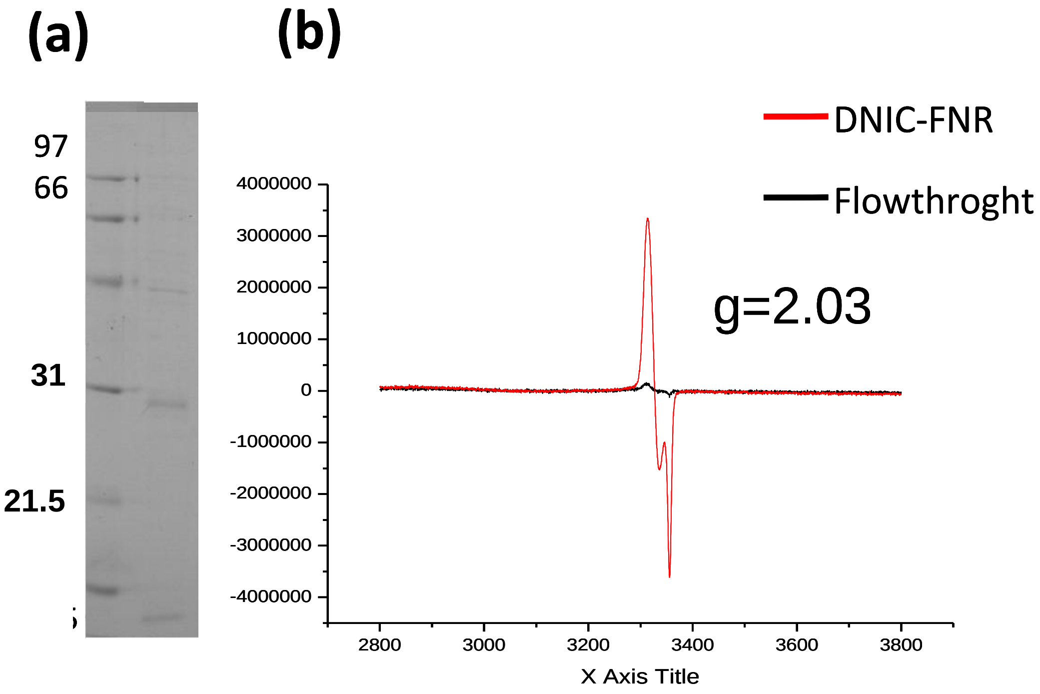

Fig. 29 The purified recombinant FNR protein (MW = 31kDa) appeared at the denatured SDS-page gel electrophoresis (a) and its EPR spectra (b) appeared at g_{av} = 2.03.

4.2.3 The determination of metal core structure in FNR

The purified FNR was subjected to determine its iron contents via ICP-OES and each of the nitrosylated monomeric FNR protein was identified to contain 2.42 irons. It means that there are two DNIC in FNR monomer by using cysteine residue as metal coordinated ligands. Then, we subsequently reduced the nitrosylated FNR protein via dithionite. From its redox titration experiments, we can observe another paramagnetic species gradually appeared at g_{av} = 1.97 that is representing the formation of anionic Roussin's red ester in **Fig. 30**. Significantly, these results inferred that the nitrosylated FNR should exhibit both dinitrosyl iron complexes (DNIC) as well as diamagnetic species (RRE) in its metal core. At least 4 eq dithionite can be capable to transform

DNICs to anionic Roussin's red ester which are consistent with the results ICP measurements.

We additionally carried out the experiments to characterize the nitrosylated iron-sulfur cluster of FNR protein from *E. coli* via determination of its X-ray absorption Near Edge Structure (XANES). The dithionite treated nitrosylated FNR was also studied here. Both of the normalized absorption coefficients, in XANES region are displayed in **Fig. 31**. By comparison with the standards of iron foil and ferrous chloride, the nitrosylated FNR spectra (green line) presented significant absorption intensity around 7113 eV in pre-edge region of the transition 1s→3d indicate the local geometry of Fe center could be in a non-centrosymmetric environment such as T_d symmetry owing to the forbidden transition with the involvement of d-p mixing. It appeared as a standard iron nitrosylated complex in tetrahedron geometry.

After we reduced the species with dithionite, the diamagnetic species would gradually be reduced to anionic Roussin's red ester. The absorption of edge jump for the nitrosylated FNR is close to the ferrous chloride standard whereas the nitrosylated FNR treated with dithionite is around the edge jump of iron foil (**Fig. 31**). The corresponding near edge data is actually consistent with the previous EPR studies.

doi:10.6342/NTU201903909

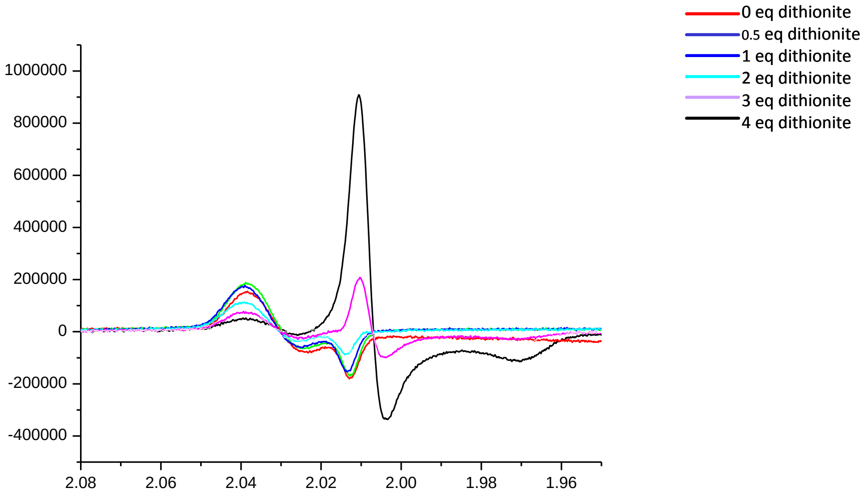

Fig. 30 The EPR studies of nitrosylated FNR protein containing [4Fe-4S]. By varying the concentration of dithionite, we can observe the incremental formation of the anionic Roussin's red ester.[124, 125]

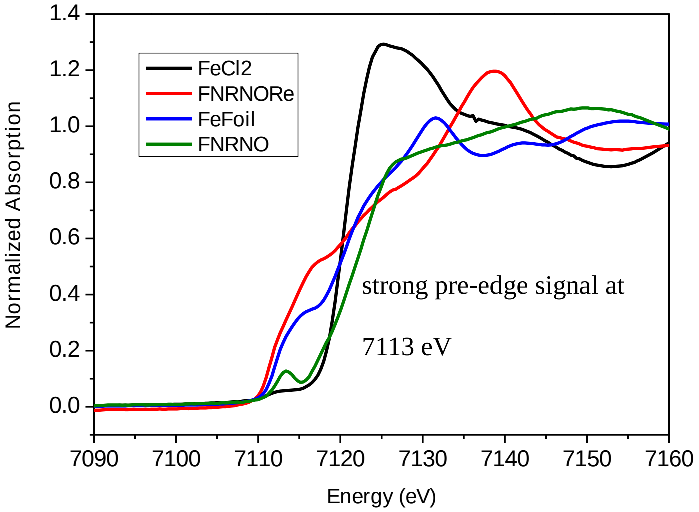

Fig. 31 The normalized X-ray absorption near edge spectra (XANES) at Fe K-edge of nitrosylated FNR (green line), nitrosylated FNR treated with sodium dithionite (red line), iron foil (blue line) and ferrous chloride (black line).

doi:10.6342/NTU201903909

4.2.4 FNR protein can bind to both the upstream and downstream regulatory domains of fnr operons

The observation of nitrosylated FNR protein under the anaerobic respiration would allow us to further examine their physiological role in *E. coli*. Nucleotides –163 to +40 relative to the transcription start site (circled) was shown in **Fig. 32**. The predicted upstream and downstream FNR binding sites are underlined, and the asterisks indicate the bases in both of the sites that were modulated. The *fnr* start codon is also underlined, and the –35, –10, and extended –10 promoter elements are boxed. We identified that the *fnr* operon region exhibits two possible binding sites for FNR protein according to the bio-informatic analysis. These two sites are designated as upstream site and downstream site, respectively. Up to date, there is not any data reported that FNR binds at the upstream site in the regulatory region.

Therefore, we designed the appropriate oligonucleotide probes to cover both the upstream and downstream binding sites shown in **Fig. 32**. From the gel retardation experiments, we can observe the nitrosylated recombinant FNR bound to both the upstream and downstream regulatory sites with the dissociation constants of 30 μM and 10 μM, respectively (**Fig. 33**). However, nitrosylated FNR protein is highly-sensitive to O_2 and electron flux which lead nitric oxide release. However, the electrophoresis of small DNIC has showed DNIC anionic complexes would be formed and be capable to ionize $[Fe(NO)_2]$ coordinated cysteine ligands.[126] It suggested that EMSA method for nitrosylated FNR indicated nitrosylated FNR can bind its own upstream operon, but the affinity might be under-esteemed. So we try to measure

doi:10.6342/NTU201903909

nitrosylated FNR protein affinity with its operon DNA by Fluorescence anisotropy further.

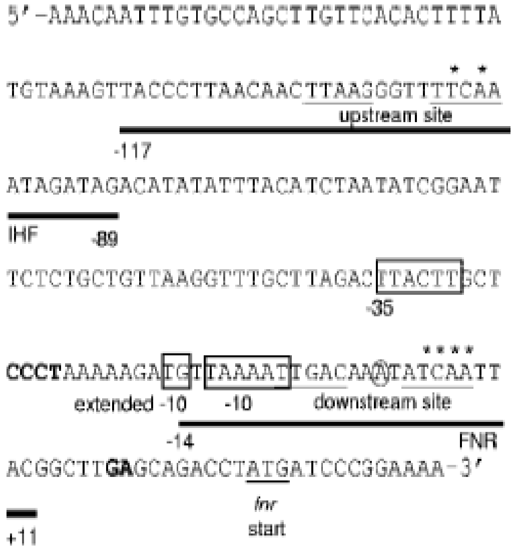

Fig. 32 The *fnr* operon region from –163 to +40.

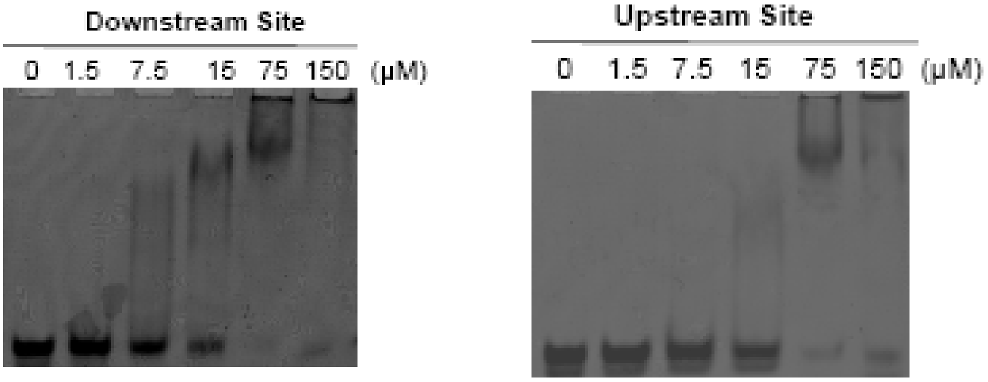

Fig. 33 The gel retardation experiments for nitrosylated FNR bound with the upstream and downstream regions of *fnr* operon.

Further experiments on fluorescence anisotropy studies were also carried out to ensure that nitrosylated FNR protein exhibits the capability to bind specifically to both 40-mer upstream and downstream consensus strands of regulatory region in *fnr* operon.

These two double-stranded DNA fragments are labeled with fluorescein isothiocyanate at 5’-end. Aliquots of anaerobic nitrosylated FNR protein solutions were titrating into a series of 2 nM duplex 40-mer DNA (*filled circles*) solutions in **Fig. 34**. We followed the changes in fluorescence anisotropy due to the protein-DNA interaction. An increase in anisotropy was observed with the incremental FNR concentration. The data would be capable to be fitted into one-site binding curves that allow us to estimate that the nitrosylated FNR protein exhibits affinity for both upstream and downstream consensus sequences in the regulatory region of *fnr* operon with the equilibrium dissociate constants (K_d) of ca. 40 nM.

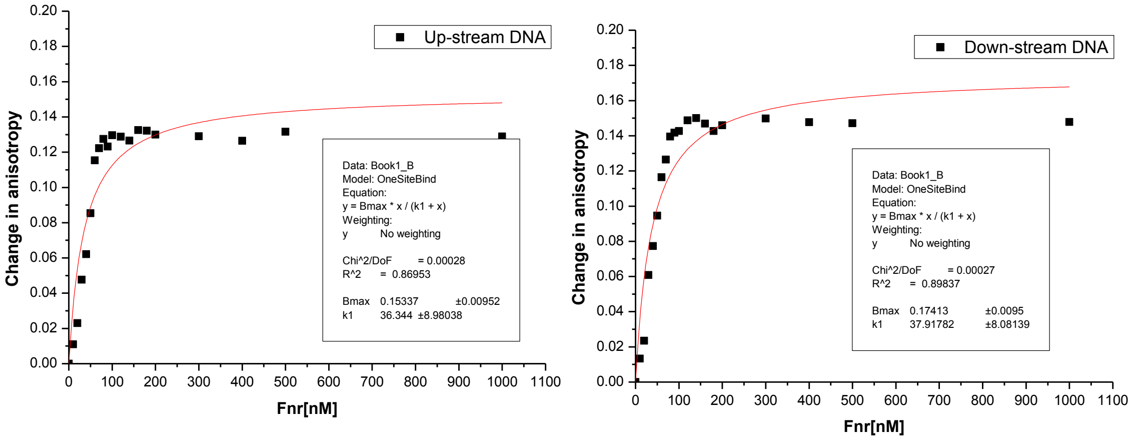

Fig. 34 Binding studies of fluorescence anisotropy for nitrosylated FNR to the promotor regions (upstream *versus* downstream) of *fnr* operon.

The appropriate probes of oligonucleotides were also designed to examine the mRNA transcriptions for the expression of the native FNR protein transcribed mediated by *E. coli* chromosomal DNA and its recombinant protein transcribed by *pET22bfnr* plasmid DNA. (**Fig. 35**) The data in **Fig. 36** showed that the native *fnr* mRNA transcripts under anaerobic nitrate respiratory is 23 times higher than the corresponding transcripts under aerobic respiratory (in the presence of the dioxygen). Our results indicated that the recombinant FNR under nitrosylation by the formation of DNIC-FNR would be capable to activate the *fnr* operon.

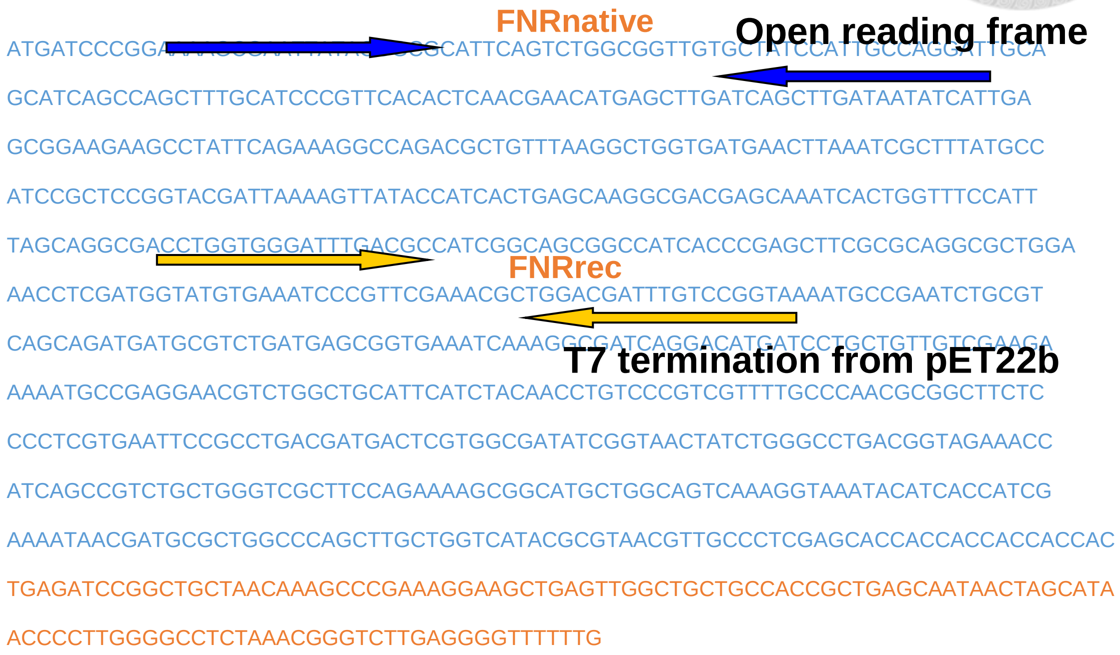

Fig. 35 The probe design for the real time PCR studies to quantify the mRNA expression of the native FNR *versus* the recombinant FNR proteins.

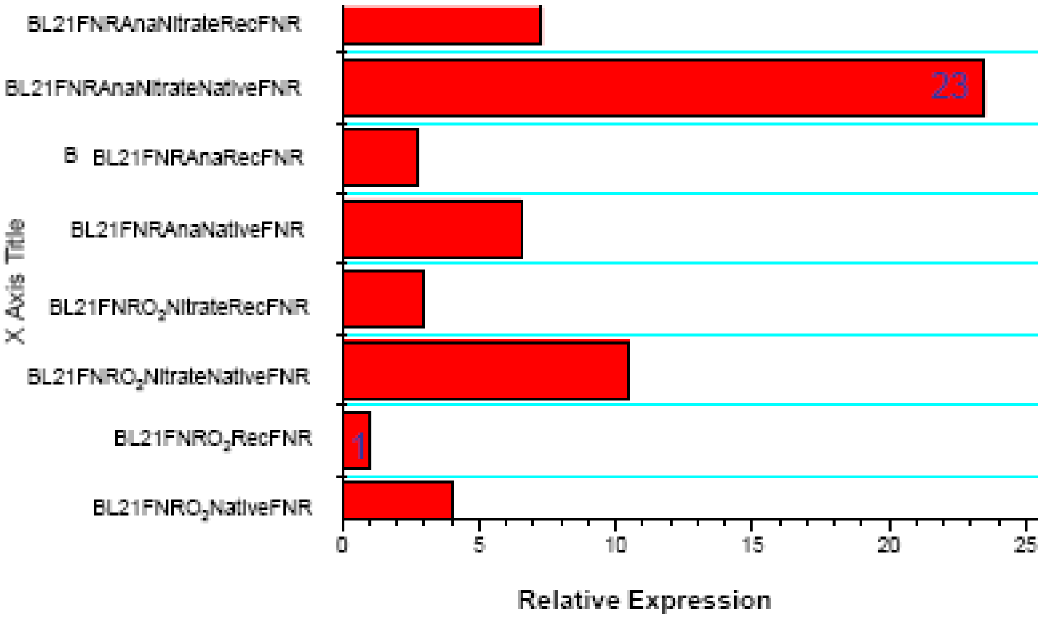

doi:10.6342/NTU201903909

Fig. 36 The quantification of relative mRNA transcription levels of the native and recombinant FNR proteins.

4.3 Conclusions

The observation of nitrosylated FNR protein under the anaerobic respiration allows us to further examine their physiological role in *E. coli*. From the gel retardation experiments, we examined that the nitrosylated FNR protein can both bind to the upstream and downstream regulation area of *fnr* operon. Their association constants are presented at ca. 30 and 10 μM, respectively. Considering the sensitive iron core of nitrosylated FNR, an additional evidence from fluorescence anisotropic studies is provided that the nitrosylated FNR protein indeed exhibits the capability to bind to both of the consensus sequences in K_d = ~40 nM. Besides, the mRNA expression level of *fnr* gene was also determined via quantitative PCR techniques and indicated that *fnr* gene can be up-regulated in nitrate respiratory. All these biochemical characterizations we have shown here suggest that the iron-sulfur cluster of FNR protein can be chemically modulated via nitric oxide stress in anaerobic environment to actively regulate the protein expression for nitrate dissimilation and anaerobic respiratory.

However, is there any different between nitric oxide titration that we showed in this study and the physiological anaerobic nitrate respiratory in bacteria? Recently, ESI-MS analysis on nitrosylated [4Fe4S] has provide remarkable insight into the nitrosylation reactions, permitting identification, for the first time, of protein-bound

doi:10.6342/NTU201903909

mono-, di- and tetranitrosyl [4Fe–4S] cluster complexes ([4Fe–4S](NO), [4Fe–4S])(NO)$_2$ and [4Fe–4S](NO)$_4$) as intermediates along pathways to formation of product Roussin's red ester (RRE) and Roussin's black salt (RBS)-like species. It means that [4Fe–4S] proteins have delicated way to react with nitric oxide, and to form many intermediate to fine-tune their functions. In FNR a possible DNIC number might be 3 under anaerobic nitrate respiratory. If no oxygen, the three DNICs will change AR1 conformation of FNR to bind fnr operon well. To combine our data that we demonstrate here, the outcome gives a light to understand how FNR play multiple roles on nitrate metabolism. In addition, it suggest that we can further try to screen nitrosylated fnr's downstream genes to know more details about nitrate respiratory. For most of the cases, people thought nitric oxide always kill the function of [4Fe–4S] proteins. But here we showed the first case of nitrosylated [4Fe–4S] proteins is functional and behaved in the way of the positive autoregulation. As the dinitrosyl complexes, forming the (likely) tri- and tetranitrosyl complexes within the [4Fe4S] protein FNR may vary their functions of [4Fe–4S] proteins, like Fnr leave a fantastic space for the future investigation.

4.4 Experiments

4.4.1 Cloning of transcription factor, fumarate-nitrate reduction (FNR)

The polymerase chain reactions were carried out using 2 pairs of primers, FNRForward1(5'-TATGATCCCGGAAAAGCGAATTATAC-3'), FNRReverse1(5'-GGGCAACGTTACGCGTATGACTA-3'), FNRForward2(5'-TGATCCCGGAAAAGCGAATTATAC-3'), FNRReverse2(5'-TCGAGGGCAACGTTACGCGTAT- 3').

doi:10.6342/NTU201903909

E. coli K12 genomic DNA was served as the template. The final products carrying with the two flanking ends of restriction enzymes, NdeI and XhoI, –linearized pET22b fragment that was double digested by NdeI and XhoI. The obtained plasmid, pET22bfnr, was confirmed by sequence of *fnr* gene. The alignment of the experimental sequence data with the *fnr* sequence from the NCBI nucleotide collection database reveal no mutation in the recombinant fnr gene.

4.4.2 Strains, Media, and Culture Conditions

Anaerobic cultures of *E. coli* were grown at 37 °C in Luria-Bertani (LB) media containing potassium nitrate (KNO_3) at a final concentration of 100 mM and supplemented with ampicillin (100 μg/ml). Anaerobic cultures for EPR experiments and 1D SDS PAGE were grown in 15-ml screw-cap centrifuge tubes filled to the brim with media. Cultures were incubated overnight in LB containing 100 mM NO_3^- (two tubes for each strain). Cells were harvested by centrifugation (10 min, 5500 rpm, 4 °C) and washed with phosphate-buffered saline (PBS), pH 7.4, and then suspended in PBS to a final volume of 1.0 ml. The bacterial cells for EPR experiment were re-suspended to 10.0 OD.

4.4.3 Recombinant FNR protein over-expression and purification

4.4.4 Nitrosylated FNR protein

The nitrosylated FNR protein appeared with a brown-yellow color. The nitrosylated FNR was transferred to EPR tube in an anaerobic chamber and flash frozen for analysis. The EPR absorption of the nitrosylated FNR protein appeared at $g_{av} = 2.03$.

4.4.5 Quantification of mRNA for fnr expression by real-time quantitative Polymerase Chain Reaction (RT-qPCR)

To distinguish and quantify mRNAs of *fnr* from *E. coli* chromosome genome and recombinant pET22b-FNR vector, total RNA was isolated from 3-ml culture of grown to mid-log phase by using Viogene RNA Kit. The isolate of intact RNA was intermediately treated with DNase I (Ambion, Austin, TX), phenol extract, and stored at -80^{o}C. The obtained RNA was served as templates for cDNA synthesis using random primers and reverse transcriptase, Supertranscript III (invitrogen). PCR was performed using iQ SYBRgreen supermix, with fluorescence measured in Real-Time PCR by using ABI step one machine (ABI). Relative expression was standardized by determining the ratio of the transcript value in each gene to the 16S RNA transcription value. Control reactions were performed in parallel mock DNA reactions generated without reverse transcriptase to verify specific amplification. The presence of single product of correct approximate size was verified by RT-PCR melting curve, agarose gel electrophoresis and ethidium bromide staining. The relative levels of expression of genes of interest, compared with the untreated controls, were calculated following the protocol for the comparative CT method in User Bulletin #2 supplied by Applied Biosystems.

4.4.6 UV-vis spectroscopy

The UV-vis spectrum of nitrosylated FNR protein was determined on HP 8453 (HP). The UV-vis spectrum of the sample was record in 1-cm cell from 190-1100 cm^{-1}, respectively, at room temperature.

4.4.7 Circular Dichroism (CD) spectroscopy

The CD spectrum of nitrosylated FNR protein was determined on π* CD spectrometer (AP). The CD spectrum of the sample was record in 1-mm cell from 190-600 cm^{-1}, respectively, at room temperature. A scan interval of 1 nm with an integration of 100,000 points was employed. The spectrum of Buffer A was also collected and subtracted automatically.

4.4.8 X-ray absorption near edge spectra (XANES)

X-ray absorption near edge spectra (XANES) were carried out at beamline 17C in the National Synchrotron Radiation Research Center (NSRRC), Hsinchu, Taiwan. BL17C is a wiggler beamline, and photo flux is around 5×10^{10} at 4mm(H) × 2mm(V) beam size. The sample was sealed in a cell with Mylar windows and the experimental beam size was 4 mm(H) × 2 mm(V). The spectra were collected in a fluorescence mode with either a 13-element solid state detector or a Lytle detector, and the photon energy was scanned from 6.912 to 7.160 keV. A reference Fe foil was always measured simultaneously with the sample and the first inflection point at 7112.0 eV of the Fe foil spectrum was used for energy calibration.

4.4.9 Quantification of the metal contents by inductively coupled plasma optical emission spectroscopy (ICP-OES).

The protein samples were dissolved in saturated 65% HNO_3 solution (5.0 mL) (suprapure grade, Merck). The samples were digested at 180°C 800W in a MARS5 microwave digestion system (CEM Inc.). The temperature was altered from room

doi:10.6342/NTU201903909

temperature to 180°C in 15 min, and maintained at 180°C for another 15 min. The digested samples were then diluted with the addition of 20 ml doubly distilled water (Millipore) prior to iron analysis. The iron concentrations of the samples were determined by a standard linear plot of series concentrations of standard $Fe(NO_3)_2$ solution in 0.10 N HNO_3. A solution of 0.10 N HNO_3 in distilled water was used as the iron-free control. The digested samples were measured by the Agilent technologies ICP-OES 720S.

4.4.10 Electrophoretic mobility shift assay (EMSA)

Standard EMSA method was used to investigate protein-DNA interactions. The experiment showed that the predicted DNA binding sites were resided at the upstream and downstream regions of the *fnr* promoter, which were selected to synthesize 5’-FAM labelled DNA. Proteins were supplied as a concentration gradient against a constant concentration of dsDNA. The amount of DNA was mixed in 10 μl EMSA reaction buffer (400 mM NaCl; 50 mM sodium phosphate; PH 8.0; 10% gycerol). The mixture was incubated at 25 ^{o}C for 1 h, after which the reaction products were loaded onto 12 % polyacrylamide TBE gel (BioRad, Hercules CA).

4.4.11 Fluorescence Anisotropy

Fluorescence anisotropy was used to measure FNR binding to the predicted binding site. The FNR consensus binding sites for upstream and downstream regulation regions were located centrally within a pair of complementary 40-bp oligonucleotides. The two upstream complementary oligonucleotides are *fnr*-UP forward strand: 5’-AAAGTTACCCTTAACAACTTAAGGGTTTTCAAATAGATAG-3’ and *fnr*-UP reverse strand: 5’-CTATCTATTTGAAAACCCTTAAGTTGTTAAGGGTAACTTT-3’ whereas the two downstream complementary oligonucleotides are *fnr*-Down forward strand: 5’-AAGATGTTAAAATTGACAAATATCAATTACGGCTTGAGCA-3’ and the *fnr*-Down reverse strand: 5’-TGCTCAAGCCGTAATTGATATTTGTCAATTTTAACATCTT-3’. The forward strands were 5’-labeled with fluorescein isothiocyanate. The double-stranded 40-mer DNA fragments were suspended in filtered distilled H_2O for the subsequent fluorescence study.

Sealed florescence cuvettes (Hellma) were prepared anaerobically. Fluorescence anisotropy was measured in a HITACHI F-4500 fluorescence spectrophotometer at 27.4°C using an excitation of 483 nm and detecting emission at 517 nm. Both forms of FNR proteins ($[4Fe\text{-}4S]^{2+}$ and nitrosylated) were titrated into concentrations up to 1000 nM, respectively. Fluorescence anisotropy was calculated in triplicate for each [FNR], and the experiments were carried out using the *fnr* consensus sequences represented for both the upstream and downstream regulatory regions.

Chapter 5 Summary and Conclusions

Part I.

PmoB is Copper Sponge

Although crystal structures of the pMMO from several species have been known for some years, we have, at this juncture, only the protein structures folded with 2 or 3 copper ions in the PmoB subunit and a Zn^{II} or Cu^{II} site in the PmoC subunit. Here, we gave another evidence to indicate the PmoB was Cu^{I}-rich protein. In the respect of copper insertion, we have proved that copper ion incorporation into PmoB recombinant protein in *E. coli* spontaneously. In the past, extracellular Cu-complexing agent is the Cu-binding compound (i.e. methanobactin, analogous to iron siderophores) first identified in association with pMMO of *M. capsulatus* Bath.[127] Furthermore, it has been discovered that methanobactin accumulates in the growth medium of *M. trichosporium* OB3b grown in the presence of <0.7 μM Cu. Cu-containing methanobactin (Cu-mb) would rapidly be internalized into the cell when Cu was provided at concentrations between 0.7 and 1.0 μM, which coincides with supression of sMMO expression and induction of higher levels of pMMO expression. However, in our case of copper-PmoB, the apparatus in *E.coli* was sufieciently incorporate copper into PmoB. It suggested that methanobactin may not be completely crucial but other chaperone proteins and cofactors in *E.coli* can be essential for PmoB copper ion accommodation. As a copper tolerant strain, the *E. coli* K12 TB1 cells might be equipped with the copper trafficking protein Cop A to sequester Cu^{I} ions into a membrane-bound protein subunit.[96] It was worth to notice that most of copper ions were not observed in crystallization and X-ray analysis because the multiple copper ions were lost during the purification of the protein.

In the membrane-bound PmoB subunit, the N-terminal and C-terminal sub-domains are anchored in the membrane and the **A** and **B** site copper ions are constrained to facilitate ligation of the Cu^I at the A site with Gln404 from the C-terminal sub-domain. A site bears one copper while B site shows dicopper center in XANES analysis. A site and B site in spmoB perhaps can function together as a “tricopper cluster” and harness an “oxene” for O-atom transfer to a hydrocarbon substrate. However, there is no specific activity toward methane oxidation or propene epoxidation has been observed for any of the MBP-PmoB proteins in the present study. In the case of copper-rich PmoB, it functions for H_2O_2 production for methane oxidation. Recently NADH-dependent activity studies show that the partial removal of copper ion may disrupt the electron transfer from NADH to the electron entrance of pMMO via endogenous quinone derivative.[128] And copper ions outside the catalytic site may mediate electron transfer from endogenous hydroquinone-derivative to the catalytic site of pMMO or/and may enhance proton release from hydroquinone-derivative. Also, the copper ions may stabilize the binding of endogenous hydroquinone-derivative to pMMO.

A site in PmoB

We have no data that bears on the role of the mononuclear Cu^I at the A site in the overall function of the enzyme. The ligands of this Cu^I ion are associated with amino acid residues from both the N- and C-terminal water soluble sub-domains (His48, His72 , and Gln404) of the PmoB subunit. We observed that $PmoB_{33-414}$ shows the

doi:10.6342/NTU201903909

activity of H_2O_2 production. The presence of N-terminal signal peptide would affect the corresponding oxidase activity. Possibly, the Site A plays role in the interaction between PmoAC and PmoB. However, this hypothesis needs to be verified by further studies.

B site in PmoB

MBP that we have heterologously over-expressed in the *E. coli* membranes can serve as a functional model for the study of the PmoB subunit in pMMO. The dinuclear copper site (the B site) are verified by EXAFS. There is an apparent correlation between these two observables in the EXAFS data. The Cu···Cu distance varies from 2.64 Å to 2.95 Å, which is significantly longer than that for Cu^0 nanoparticles (2.56 Å to 2.58 Å) and Cu foil (2.54 Å (EXAFS) and 2.556 Å (X-ray diffraction)). The dicopper center in our MBP-$PmoB_{33–414}$ protein is presumably formed by His137 and His139 ligated to one of the Cu^I ions and His33 with the other Cu^I (Tyr374 might be also involved here. And this dicopper function as the production of H_2O_2. The copper ions that form the B site in the $MBPPmoB_{33–414}$ protein can be oxidized to Cu^{II} and produce H_2O_2 after exposure of these purified membranes to air overnight at 4 °C. After the oxidation of these copper ions, we detect Cu···Cu back-scattering in the Cu EXAFS of the MBP-$PmoB_{33–414}$ protein just as has been reported for the spmoB protein by the Northwestern group. Almost all the E-cluster copper ions are also oxidized by this treatment, releasing 2.8 molecules of H_2O_2 per PmoB protein. Here, in a scenario in which the copper ions associated with the **B** site can react with O_2, as in the case of the membranes of the $MBPPmoB_{33–414}$ protein, it is evident that these reducing equivalents can be gradually drained away from the E-cluster Cu^I ions. It is possible

doi:10.6342/NTU201903909

that the reaction of O_2 with the dicopper site can gate the flow of reducing equivalents from these Cu^I ions to produce the H_2O_2 observed. The B site in PmoB subunit can behave as the catalytic center of O_2 chemistry, augmented by interactions of the PmoB subunit with the PmoA/PmoC subunits.

E cluster in PmoB

The remaining Cu^I ions of the PmoB subunit, ca. 6 or 7 in number, have very high redox potentials and cannot be oxidized directly by O_2 normally. However, in the oxidation of $PmoB_{33\text{-}414}$ with O_2, these highly reduced Cu^I can be oxidized. And the reducing equivalents can be drained away from the E-cluster Cu^I ions also. These copper play the role as E cluster for electron transfer.

The PmoB subunit can also be mechanically changeable. Examination of the PmoB amino acid sequence shows that the subunit is extremely rich in Met, Asp, and Glu (Table S2 in APPENDIX), with many of these related residues even only one or two residues apart. With these hard ligands and the spatial distribution of these amino acids within the protein fold, it is allowable to vary the ligand structures of the 6 or 7 copper ions with a small expenditure of conformational energy. The “fully oxidized” MBP-$PmoB_{33–414}$ protein indicates that this scenario is plausible.

In this whole study, PmoB is consist of site A, site B and E cluster which together conform a redox-drive molecule machine. Only MBP-$PmoB_{33–414}$ protein bears O_2 Chemistry. It shows the N-terminal sequence also a plays role in HoloPmmo. It is waiting for the future work to elucidate How PmoA and PmoC interact with N-terminal

doi:10.6342/NTU201903909

sequence of PmoB. We might express the holoPmmo with different N-terminal length PmoB to examine its activity and turnover rate of Cu^{I}/ Cu^{II}.

In conclusion, the present study has led to further understanding the role of the membrane-bound PmoB subunit and its copper ions in their functions of biological methane activation in electron transfer and dioxygen activation.

Part II

Nitrosylated FNR behave as positive autoregulation in Nitrate Respiratory in *E. coli*

In this work, we proved the nitrosylated FNR protein can be *in vivo* formed under the anaerobic respiration with nitrate medium and the findings allow us to further examine their physiological role in *E. coli*. From the ICP, and titration experiments with dithionite, there are 2 or 3 iron which binds with possible 5 cysteines residue support the DNIC formation. EPR shows the g_{av}=2.03 (DNIC feature) and g_{av}=1.97 (reduced RRE) after reduction. In the previous studies, DNIC • FNR only decrease the FNR-DNA binding but we found nitrosylated FNR which were formed under the nitrate respiratory in *E. coli* seems to behave as a positive autoregulation transcription factor on protein expression level (showed in 1-D SDS-PAGE). This hypothesis was directly proved by gel retardation experiments, fluorescence anisotropy, and quantitative PCR.

In DNA binding experiments, nitrosylated FNR protein can both bind to the upstream and downstream regulation area of *fnr* operon. It is plausible for explaining why nitrosylated FNR protein can serve as an activator in its operon. Their association constants are presented at ca. 30 and 10 μM, respectively in EMSA. K_d = ~40 nM in fluorescence anisotropy. Besides, the mRNA expression level of *fnr* gene was also determined via quantitative PCR techniques and indicated that *fnr* gene can be up-regulated in nitrate respiratory. In comparison with aerobic respiratory, around 20 times *fnr* mRNA observed under nitrate respiratory. All these biochemical characterizations we have shown here suggest that the iron-sulfur cluster of FNR protein can be chemically modulated *via* nitric oxide stress in an anaerobic environment to actively regulate the protein expression for nitrate dissimilation and anaerobic respiratory.

In this study, we have identified two possible functional form of nitrosylated FNR in nitrate respiratory. One is the RRE-FNR which form the similar metallic core of Fe-Cysteines to own tight DNA affinity (**Fig. 15**). The other candidate is specific DNIC-Cys assembly **(Fig. 15**). However, our data cannot exclude either of the possibilities. Another few methods such as protein crystallography or Double Electron Electron Resonance (DEER) can be deployed in the further research. If there were multiple DNICs in FNR, the hypothesis can be directly verified by DEER method because of its multiple papamagnetic systems. It is possible to directly resolve the puzzle of nitrosylated core by using X-ray protein crystallography also if we can get its protein crystal.

In the past, nitric oxide was thought as the killer or inhibit of iron-sulfur containing transcription factors. In my thesis, I have showed nitrosylated FNR gained its function under nitrate respiratory in *E.coli*. According to previous reports, biological nitric oxide evolved under nitrate respiratory in *E.coli* and highly dependent on the autoregulation of FNR protein *versus* the transcription of *fnr mRNA*. Our results of qPCR have provided an alternative explanation on how *E.coli* adapt nitirc oxide toxicity. On the other hand, DNIC is very sensitive to O_2. Or, the nitrosylated FNR can be quickly tuned and inhibited by O_2. On the contrary, when nitrate concentration decrease in anaerobic condition, the active nitrosylated FNR can be transformed to [4Fe4S] by iron-sulfur repair system. In any case, both recent studies and our research have indicated FNR protein can be modulated by nitrate respiration to form nitrosylated FNR that are very likely to be physiologically important.

In fact, it has already been found that αCTD of nitrosylated FNR can bind the upstream operon despite not enough structural information can support the controls are presumably exerted between its core and DNA binding domain. If we want to verify this idea, DNA walking or *in vitro* full-length operon DNA can be designed as a fluorescence probe for Fluorescence Resonance Energy Transfer, FRET. On the basis of different forms of FNR modulated by nitrate and aerobic respiration can either bind the upstream and downstream operon of *fnr*. CryoEM should be considered as a great technique to provide structural evidence unraveling the conformational changes of variable nitrosylated FNRs that can form several other macromolecular peorin-DNA complexes structures.

Furthermore, FNR governs many downstream genes expression among aerobic, anaerobic and nitrate respiratory in *E. coli*. We open a new window to investigate nitrosylated FNR under nitrate respiratory. For future studies, to identify DNA binding motif(s) of nitrosylated FNR(s) and its/their downstream mRNA regulations/expressions can be one of the future directions.

In conclusion, we find that a new nitrosylated FNR own its function on positive

doi:10.6342/NTU201903909

autoregulation while the redox states of FNR may play significant rules under nitrate respiratory. The new nitrosylated FNR is distinguishingly different from the ones in nitric oxide titration experiments, where the anionic RRE can be observed after reducing nitrosylated FNR. And this the present study has led to further understanding of the role of FNR and nitric oxide in the nitrate respiratory and its global regulation in *E. coli*.

doi:10.6342/NTU201903909

REFERENCES

1. Oda, A., et al., *Room-Temperature Activation of the C-H Bond in Methane over Terminal Zn(II)-Oxyl Species in an MFI Zeolite: A Combined Spectroscopic and Computational Study of the Reactive Frontier Molecular Orbitals and Their Origins.* Inorganic Chemistry, 2019. **58**(1): p. 327-338.
2. Baek, J., et al., *Bioinspired Metal-Organic Framework Catalysts for Selective Methane Oxidation to Methanol.* Journal of the American Chemical Society, 2018. **140**(51): p. 18208-18216.
3. Tang, P., et al., *Methane activation: the past and future.* Energy & Environmental Science, 2014. **7**(8): p. 2580-2591.
4. Bard, A.J., et al., *Holy Grails of Chemistry.* Accounts of Chemical Research, 1995. **28**(3): p. 91-91.
5. Lipscomb, J.D., *Biochemistry of the soluble methane monooxygenase.* Annual Review of Microbiology, 1994. **48**(1): p. 371-399.
6. Chan, S.I. and S.S.F. Yu, *Controlled Oxidation of Hydrocarbons by the Membrane-Bound Methane Monooxygenase: The Case for a Tricopper Cluster.* Accounts of Chemical Research, 2008. **41**(8): p. 969-979.
7. Friedle, S., E. Reisner, and S.J. Lippard, *Current challenges of modeling diiron enzyme active sites for dioxygen activation by biomimetic synthetic complexes.* Chemical Society Reviews, 2010. **39**(8): p. 2768-2779.
8. Lieberman, R.L. and A.C. Rosenzweig, *Biological Methane Oxidation: Regulation, Biochemistry, and Active Site Structure of Particulate Methane Monooxygenase.* Critical Reviews in Biochemistry and Molecular Biology, 2004.

doi:10.6342/NTU201903909

39(3): p. 147-164.

9. Jiang, H.-L., N. Tsumori, and Q. Xu, *A Series of (6,6)-Connected Porous Lanthanide−Organic Framework Enantiomers with High Thermostability and Exposed Metal Sites: Scalable Syntheses, Structures, and Sorption Properties.* Inorganic Chemistry, 2010. **49**(21): p. 10001-10006.
10. Culpepper, M.A. and A.C. Rosenzweig, *Architecture and active site of particulate methane monooxygenase.* Critical Reviews in Biochemistry and Molecular Biology, 2012. **47**(6): p. 483-492.
11. Chen, C.-L., et al., *The Copper Clusters in the Particulate Methane Monooxygenase (pMMO) from Methylococcus Capsulatus (Bath).* Journal of the Chinese Chemical Society, 2004. **51**. p. 1081-1098.
12. Smith, T.J. and H. Dalton, *Chapter 6 Biocatalysis by methane monooxygenase and its implications for the petroleum industry*, in *Studies in Surface Science and Catalysis*, R. Vazquez-Duhalt and R. Quintero-Ramirez, Editors. 2004, Elsevier. p. 177-192.
13. Lee, S.J., et al., *Control of substrate access to the active site in methane monooxygenase.* Nature, 2013. **494**: p. 380.
14. Martinho, M., et al., *Mössbauer Studies of the Membrane-Associated Methane Monooxygenase from Methylococcus capsulatus Bath: Evidence for a Diiron Center.* Journal of the American Chemical Society, 2007. **129**(51): p. 15783-15785.
15. Balasubramanian, R., et al., *Oxidation of methane by a biological dicopper centre.* Nature, 2010. **465**: p. 115.
16. Hanson, R.S. and T.E. Hanson, *Methanotrophic bacteria.* Annual Review of Biochemistry, 1996. **60**(2): p. 439-471.

doi:10.6342/NTU201903909

17. Murrell, J.C., I.R. McDonald, and B. Gilbert, *Regulation of expression of methane monooxygenases by copper ions.* Trends in Microbiology, 2000. **8**(5): p. 221-225.

18. Prior, S.D. and H. Dalton, *The Effect of Copper Ions on Membrane Content and Methane Monooxygenase Activity in Methanol-Grown Cells of Methylococcus-Capsulatus (Bath).* Journal of General Microbiology, 1985. **131**(Jan): p. 155-163.

19. Semrau, J.D., et al., *Particulate methane monooxygenase genes in methanotrophs.* Journal of Bacteriology, 1995. **177**(11): p. 3071-3079.

20. Ward, N., et al., *Genomic insights into methanotrophy: the complete genome sequence of Methylococcus capsulatus (Bath).* PLoS biology, 2004. **2**(10): p. e303-e303.

21. Gilbert, B., et al., *Molecular analysis of the pmo (particulate methane monooxygenase) operons from two type II methanotrophs.* Applied and Environmental Microbiology, 2000. **66**(3): p. 966-975.

22. Stolyar, S., et al., *Role of multiple gene copies in particulate methane monooxygenase activity in the methane-oxidizing bacterium Methylococcus capsulatus Bath.* Microbiology, 1999. **145 (Pt 5)**(5): p. 1235-44.

23. Holmes, A.J., et al., *Evidence that participate methane monooxygenase and ammonia monooxygenase may be evolutionarily related.* FEMS Microbiology Letters, 1995. **132**(3): p. 203-208.

24. Lieberman, R.L. and A.C. Rosenzweig, *Crystal structure of a membrane-bound metalloenzyme that catalyses the biological oxidation of methane.* Nature, 2005. **434**(7030): p. 177-182.

25. Hakemian, A.S., et al., *The Metal Centers of Particulate Methane*

Monooxygenase from Methylosinus trichosporium OB3b. Biochemistry, 2008. **47**(26): p. 6793-6801.

26. Smith, S.M., et al., *Crystal Structure and Characterization of Particulate Methane Monooxygenase from Methylocystis species Strain M.* Biochemistry, 2011. **50**(47): p. 10231-10240.

27. Hakemian, A.S. and A.C. Rosenzweig, *The biochemistry of methane oxidation.* Annual Review of Biochemistry, 2007. **76**(1): p. 223-241.

28. Nguyen, H.H., et al., *The particulate methane monooxygenase from methylococcus capsulatus (Bath) is a novel copper-containing three-subunit enzyme. Isolation and characterization.* Journal of Biological Chemistry, 1998. **273**(14): p. 7957-7966.

29. Yu, S.S.-F., et al., *Production of High-Quality Particulate Methane Monooxygenase in High Yields from Methylococcus capsulatus (Bath) with a Hollow-Fiber Membrane Bioreactor.* J Bacteriol, 2003. **185**(20): p. 5915-5924.

30. Zahn, J.A. and A.A. DiSpirito, *Membrane-associated methane monooxygenase from Methylococcus capsulatus (Bath).* Journal of Bacteriology, 1996. **178**(4): p. 1018-1029.

31. Choi, D.-W., et al., *The Membrane-Associated Methane Monooxygenase (pMMO) and pMMO-NADH:Quinone Oxidoreductase Complex from Methylococcus capsulatus Bath.* Journal of Bacteriology, 2003. **185**(19): p. 5755-5764.

32. Nagababu, P., et al., *Efficient Room-Temperature Oxidation of Hydrocarbons Mediated by Tricopper Cluster Complexes with Different Ligands.* Advanced Synthesis & Catalysis, 2012. **354**(17): p. 3275-3282.

33. Chan, S.I., et al., *Efficient oxidation of methane to methanol by dioxygen*

doi:10.6342/NTU201903909

mediated by tricopper clusters. Angewandte Chemie International Edition, 2013. **52**(13): p. 3731-3735.

34. Chan, S.I., et al., *Efficient catalytic oxidation of hydrocarbons mediated by tricopper clusters under mild conditions.* Journal of Catalysis, 2012. **293**: p. 186-194.
35. Chen, P.P.Y., et al., *Development of the Tricopper Cluster as a Catalyst for the Efficient Conversion of Methane into MeOH.* ChemCatChem, 2014. **6**(2): p. 429-437.
36. Nguyen, H.-H.T., et al., *X-ray Absorption and EPR Studies on the Copper Ions Associated with the Particulate Methane Monooxygenase from Methylococcus capsulatus (Bath). Cu(I) Ions and Their Implications.* Journal of the American Chemical Society, 1996. **118**(50): p. 12766-12776.
37. Chan, S.I., et al., *Redox potentiometry studies of particulate methane monooxygenase: support for a trinuclear copper cluster active site.* Angewandte Chemie International Edition, 2007. **46**(12): p. 1992-1994.
38. Chen, P.P.Y., et al., *Facile O-atom insertion into C-C and C-H bonds by a trinuclear copper complex designed to harness a singlet oxene.* Proceedings of the National Academy of Sciences, 2007. **104**(37): p. 14570.
39. Yu, S.S.F., et al., *The C-Terminal Aqueous-Exposed Domain of the 45 kDa Subunit of the Particulate Methane Monooxygenase in Methylococcus capsulatus (Bath) Is a Cu(I) Sponge.* Biochemistry, 2007. **46**(48): p. 13762-13774.
40. Nguyen, H., et al., *The nature of copper ions in the membranes containing the particulate methane monooxygenase from Methylococcus capsulatus (Bath).* Journal of Biological Chemistry, 1994. **269**: p. 14995-5005.

41. Ng, K.Y., et al., *Probing the hydrophobic pocket of the active site in the particulate methane monooxygenase (pMMO) from Methylococcus capsulatus (Bath) by variable stereoselective alkane hydroxylation and olefin epoxidation.* ChemBioChem, 2008. **9**(7): p. 1116-1123.

42. Baik, M.-H., et al., *Mechanistic Studies on the Hydroxylation of Methane by Methane Monooxygenase.* Chemical Reviews, 2003. **103**(6): p. 2385-2420.

43. Yu, S.S., et al., *The stereospecific hydroxylation of [2,2-2H_2]butane and chiral dideuteriobutanes by the particulate methane monooxygenase from Methylococcus capsulatus (Bath).* Journal of Biological Chemistry, 2003. **278**(42): p. 40658-40669.

44. Wilkinson, B., et al., *A Concerted Mechanism for Ethane Hydroxylation by the Particulate Methane Monooxygenase from Methylococcus capsulatus (Bath).* Journal of the American Chemical Society, 1996. **118**(4): p. 921-922.

45. Elliott, S.J., et al., *Regio- and Stereoselectivity of Particulate Methane Monooxygenase from Methylococcus capsulatus (Bath).* Journal of the American Chemical Society, 1997. **119**(42): p. 9949-9955.

46. Koshland, D.E., Jr., *The molecule of the year.* Science, 1992. **258**(5090): p. 1861.

47. Lepoivre, M., et al., *Inactivation of ribonucleotide reductase by nitric oxide.* Biochemical and Biophysical Research Communications, 1991. **179**(1): p. 442-448.

48. Marshall, H.E. and J.S. Stamler, *Inhibition of NF-κB by S-Nitrosylation.* Biochemistry, 2001. **40**(6): p. 1688-1693.

49. Gross, S.S. and M.S. Wolin, *Nitric oxide: pathophysiological mechanisms.* Annual Review of Physiology, 1995. **57**(1): p. 737-769.

50. Bogdan, C., *Nitric oxide and the immune response.* Nature Immunology, 2001.

2(10): p. 907-916.

51. Radi, R., *Reactions of Nitric Oxide with Metalloproteins.* Chemical Research in Toxicology, 1996. **9**(5): p. 828-835.

52. Tsai, M.-L., C.-C. Tsou, and W.-F. Liaw, *Dinitrosyl Iron Complexes (DNICs): From Biomimetic Synthesis and Spectroscopic Characterization toward Unveiling the Biological and Catalytic Roles of DNICs.* Accounts of Chemical Research, 2015. **48**(4): p. 1184-1193.

53. McCleverty, J.A., *Chemistry of Nitric Oxide Relevant to Biology.* Chemical Reviews, 2004. **104**(2): p. 403-418.

54. Alderton, W.K., C.E. Cooper, and R.G. Knowles, *Nitric oxide synthases: structure, function and inhibition.* Biochemical Journal, 2001. **357**(Pt 3): p. 593-615.

55. Dejam, A., et al., *Emerging role of nitrite in human biology.* Blood Cells, Molecules, and Diseases, 2004. **32**(3): p. 423-429.

56. Millar, T.M., C.R. Stevens, and D.R. Blake, *Xanthine oxidase can generate nitric oxide from nitrate in ischaemia.* Biochemical Society Transactions, 1997. **25**(3): p. 528S.

57. Bryan, N.S., et al., *Nitrite is a signaling molecule and regulator of gene expression in mammalian tissues.* Nature Chemical Biology, 2005. **1**(5): p. 290-297.

58. Bronte, V. and P. Zanovello, *Regulation of immune responses by L-arginine metabolism.* Nature Reviews Immunology, 2005. **5**(8): p. 641-654.

59. Wink, D.A. and J.B. Mitchell, *Chemical biology of nitric oxide: insights into regulatory, cytotoxic, and cytoprotective mechanisms of nitric oxide.* Free Radical Biology and Medicine, 1998. **25**(4): p. 434-456.

60. Mikkelsen, R.B. and P. Wardman, *Biological chemistry of reactive oxygen and nitrogen and radiation-induced signal transduction mechanisms.* Oncogene, 2003. **22**(37): p. 5734-5754.

61. Bouton, C. and J.-C. Drapier, *Iron Regulatory Proteins as NO Signal Transducers.* Science's STKE : signal transduction knowledge environment, 2003. **2003**: p. pe17.

62. Hess, D.T., et al., *Protein S-nitrosylation: purview and parameters.* Nature Reviews Molecular Cell Biology, 2005. **6**(2): p. 150-166.

63. Nilius, B., T. Voets, and J. Peters, *TRP channels in disease.* Science's STKE, : signal transduction knowledge environment, 2005. **2005**(295): p. re8.

64. Ding, K., et al., *Copper-dependent autocleavage of glypican-1 heparan sulfate by nitric oxide derived from intrinsic nitrosothiols.* Journal of Biological Chemistry, 2002. **277**(36): p. 33353-33360.

65. Benoff, B., et al., *Structural basis of transcription activation: The CAP-αCTD-DNA complex.* Science (New York, N.Y.), 2002. **297**: p. 1562-1566.

66. Busby, S. and R.H. Ebright, *Transcription activation by catabolite activator protein (CAP).* Journal of Molecular Biology, 1999. **293**(2): p. 199-213.

67. Lee, D.J., S.D. Minchin, and S.J. Busby, *Activating transcription in bacteria.* Annual Review of Microbiology, 2012. **66**(1): p. 125-152.

68. Lee, D.J., et al., *Analysis of interactions between Activating Region 1 of Escherichia coli FNR protein and the C-terminal domain of the RNA polymerase alpha subunit: use of alanine scanning and suppression genetics.* Molecular Microbiology, 2000. **37**(5): p. 1032-1040.

69. Weber, K.D., O. Vincent, and P. Kiley, *Additional determinants within Escherichia coli FNR activating region 1 and RNA polymerase alpha subunit*

doi:10.6342/NTU201903909

required for transcription activation. Journal of Bacteriology, 2005. **187**: p. 1724-1731.

70. Williams, S.M., et al., *Transcription activation at Class I FNR-dependent promoters: identification of the activating surface of FNR and the corresponding contact site in the C-terminal domain of the RNA polymerase α subunit.* Nucleic Acids Research, 1997. **25**(20): p. 4028-4034.

71. Wing, H.J., S.M. Williams, and S.J. Busby, *Spacing requirements for transcription activation by Escherichia coli FNR protein.* Journal of Bacteriology, 1995. **177**(23): p. 6704-6710.

72. E Lamberg, K., et al., *Characterization of activating region 3 from Escherichia coli FNR.* Journal of Molecular Biology, 2002. **315**: p. 275-283.

73. Wing, H.J., et al., *Role of activating region 1 of Escherichia coli FNR protein in transcription activation at class II promoters.* Journal of Biological Chemistry, 2000. **275**(37): p. 29061-29065.

74. Kiley, P.J. and H. Beinert, *The role of Fe–S proteins in sensing and regulation in bacteria.* Current Opinion in Microbiology, 2003. **6**(2): p. 181-185.

75. Kiley, P.J. and H. Beinert, *Oxygen sensing by the global regulator, FNR: the role of the iron-sulfur cluster.* FEMS Microbiol Rev, 1998. **22**(5): p. 341-352.

76. Korner, H., H.J. Sofia, and W.G. Zumft, *Phylogeny of the bacterial superfamily of Crp-Fnr transcription regulators: exploiting the metabolic spectrum by controlling alternative gene programs.* FEMS Microbiology Reviews, 2003. **27**(5): p. 559-592.

77. Lazazzera, B.A., et al., *DNA binding and dimerization of the Fe-S-containing FNR protein from Escherichia coli are regulated by oxygen.* Journal of Biological Chemistry, 1996. **271**(5): p. 2762-2768.

doi:10.6342/NTU201903909

78. Green, J., et al., *Reconstitution of the [4Fe-4S] cluster in FNR and demonstration of the aerobic-anaerobic transcription switch in vitro.* The Biochemical Journal, 1996. **316 (Pt 3)**: p. 887-892.

79. Crack, J., et al., *Superoxide-mediated amplification of the oxygen-induced switch from [4Fe-4S] to [2Fe-2S] clusters in the transcriptional regulator FNR.* Proceedings of the National Academy of Sciences of the United States of America, 2007. **104**: p. 2092-2097.

80. Scott, C. and J. Green, *Miscoordination of the iron-sulfur clusters of the anaerobic transcription factor, FNR, allows simple repression but not activation.* Journal of Biological Chemistry, 2002. **277**(3): p. 1749-1754.

81. Sutton, V.R., et al., *Superoxide Destroys the [2Fe-2S]*$^{2+}$ *Cluster of FNR from Escherichia coli.* Biochemistry, 2004. **43**(3): p. 791-798.

82. Lazazzera, B., M. Bates, and P. Kiley, *The activity of the Escherichia coli transcription factor FNR is regulated by a change in oligomeric state.* Genes & Development, 1993. **7**: p. 1993-2005.

83. Green, J., M. Rolfe, and L. Smith, *Transcriptional regulation of bacterial virulence gene expression by molecular oxygen and nitric oxide.* Virulence, 2014. **5**:p. 794-809.

84. Crack, J., et al., *Iron-Sulfur Clusters as Biological Sensors: The Chemistry of Reactions with Molecular Oxygen and Nitric Oxide.* Accounts of Chemical Research, 2014. **47**: p. 3196-3205.

85. McKay, D. and T. A. Steitz, *Structure of catabolite gene activator protein at 2.9 A resolution suggests binding to left-handed B-DNA.* Nature, 1981. **290**: p. 744-749.

86. N Septer, A., et al., *FNR-mediated regulation of bioluminescence and anaerobic*

respiration in the light-organ symbiont Vibrio fischeri. FEMS Microbiology Letters, 2010. **306**: p. 72-81.

87. Volbeda, A., et al., *The crystal structure of the global anaerobic transcriptional regulator FNR explains its extremely fine-tuned monomer-dimer equilibrium.* Science advances, 2015. **1**(11): p. e1501086-e1501086.

88. Rodionov, D., et al., *Dissimilatory Metabolism of Nitrogen Oxides in Bacteria: Comparative Reconstruction of Transcriptional Networks.* PLoS Computational Biology, 2005. **1**: p. 0415-0431.

89. Koningsberger, D.C., *X-ray absorption: principles, applications, techniques of EXAFS, SEXAFS, and XANES.* 1988, United States: John Wiley and Sons.

90. N. M. Ravel, B. and M. Newville, *Data analysis for X-ray absorption spectroscopy using IFEFFIT.* Journal of Synchrotron Radiation, 2005. **12**: p. 537-541.

91. Newville, M., *IFEFFIT: interactive XAFS analysis and FEFF fitting.* Journal of Synchrotron Radiation, 2001. **8**: p. 322-324.

92. Espírito Santo, C., et al., *Contribution of Copper Ion Resistance to Survival of Escherichia coli on Metallic Copper Surfaces.* Applied and Environmental Microbiology, 2008. **74**: p. 977-986.

93. Robinson, N.J. and D.R. Winge, *Copper metallochaperones.* Annual Review of Biochemistry, 2010. **79**: p. 537-562.

94. Osman, D. and J.S. Cavet, *Chapter 8 - Copper Homeostasis in Bacteria*, in *Advances in Applied Microbiology*, A.I. Laskin, S. Sariaslani, and G.M. Gadd, Editors. 2008, Academic Press. p. 217-247.

95. Pham, M.D., et al., *Inactivation of the particulate methane monooxygenase (pMMO) in Methylococcus capsulatus (Bath) by acetylene.* Biochimica et

doi:10.6342/NTU201903909

Biophysica Acta (BBA) - Proteins and Proteomics, 2015. **1854**(12): p. 1842-1852.

96. Ridge, P.G., Y. Zhang, and V.N. Gladyshev, *Comparative genomic analyses of copper transporters and cuproproteomes reveal evolutionary dynamics of copper utilization and its link to oxygen.* PloS one, 2008. **3**(1): p. e1378-e1378.

97. Li, G.-W., et al., *Quantifying Absolute Protein Synthesis Rates Reveals Principles Underlying Allocation of Cellular Resources.* Cell, 2014. **157**(3): p. 624-635.

98. Shiota, Y., G. Juhász, and K. Yoshizawa, *Role of Tyrosine Residue in Methane Activation at the Dicopper Site of Particulate Methane Monooxygenase: A Density Functional Theory Study.* Inorganic Chemistry, 2013. **52**(14): p. 7907-7917.

99. Smith, P.K., et al., *Measurement of protein using bicinchoninic acid.* Analytical Biochemistry, 1985. **150**(1): p. 76-85.

100. Lieberman, R.L., et al., *Characterization of the Particulate Methane Monooxygenase Metal Centers in Multiple Redox States by X-ray Absorption Spectroscopy.* Inorganic Chemistry, 2006. **45**(20): p. 8372-8381.

101. Culpepper, M.A., et al., *Identification of the Valence and Coordination Environment of the Particulate Methane Monooxygenase Copper Centers by Advanced EPR Characterization.* Journal of the American Chemical Society, 2014. **136**(33): p. 11767-11775.

102. Ottenwaelder, X., et al., *Reversible O−O Bond Cleavage in Copper−Dioxygen Isomers: Impact of Anion Basicity.* Journal of the American Chemical Society, 2006. **128**(29): p. 9268-9269.

103. Lewis, E.A. and W.B. Tolman, *Reactivity of Dioxygen−Copper Systems.*

doi:10.6342/NTU201903909

Chemical Reviews, 2004. **104**(2): p. 1047-1076.

104. Itoh, S. and S. Fukuzumi, *Monooxygenase Activity of Type 3 Copper Proteins.* Accounts of Chemical Research, 2007. **40**(7): p. 592-600.

105. Lai, N.-C., et al., *Efficient selective oxidation of propylene by dioxygen on mesoporous-silica-nanoparticle-supported nanosized copper.* Journal of Catalysis, 2018. **365**: p. 411-419.

106. Cao, L., et al., *Quantum Refinement Does Not Support Dinuclear Copper Sites in Crystal Structures of Particulate Methane Monooxygenase.* Angewandte Chemie International Edition, 2017. **130**: p. 162-166.

107. Waldron, K.J. and N.J. Robinson, *How do bacterial cells ensure that metalloproteins get the correct metal?* Nature Reviews Microbiology, 2009. **7**: p. 25-35.

108. Decker, H. and F. Tuczek, *Tyrosinase/catecholoxidase activity of hemocyanins: structural basis and molecular mechanism.* Trends in Biochemical Sciences, 2000. **25**(8): p. 392-397.

109. Monzani, E., et al., *Tyrosinase Models. Synthesis, Structure, Catechol Oxidase Activity, and Phenol Monooxygenase Activity of a Dinuclear Copper Complex Derived from a Triamino Pentabenzimidazole Ligand.* Inorganic Chemistry, 1998. **37**(3): p. 553-562.

110. Nagababu, P., et al., *Developing an efficient catalyst for controlled oxidation of small alkanes under ambient conditions.* Catalysis Science & Technology, 2014. **4**(4): p. 930-935.

111. Liu, C.-C., et al., *Heterogeneous formulation of the tricopper complex for efficient catalytic conversion of methane into methanol at ambient temperature and pressure.* Energy & Environmental Science, 2016. **9**(4): p. 1361-1374.

doi:10.6342/NTU201903909

112. Wang, V.C.C., et al., *Alkane Oxidation: Methane Monooxygenases, Related Enzymes, and Their Biomimetics.* Chemical Reviews, 2017. **117**(13): p. 8574-8621.

113. Mettert, E. and P. Kiley, *Contributions of [4Fe-4S]-FNR and Integration Host Factor to fnr Transcriptional Regulation.* Journal of Bacteriology, 2007. **189**: p. 3036-3043.

114. Johnson, D.C., et al., *Structure, function, and formation of biological iron-sulfur clusters.* Annual Review of Biochemistry, 2005. **74**(1): p. 247-281.

115. Gardner, P.R., et al., *Nitric oxide dioxygenase: an enzymic function for flavohemoglobin.* Proceedings of the National Academy of Sciences of the United States of America, 1998. **95**(18): p. 10378-10383.

116. Hausladen, A., A.J. Gow, and J.S. Stamler, *Nitrosative stress: metabolic pathway involving the flavohemoglobin.* Proceedings of the National Academy of Sciences of the United States of America, 1998. **95**(24): p. 14100-14105.

117. Kim, S.O., et al., *Anoxic function for the Escherichia coli flavohaemoglobin (Hmp): reversible binding of nitric oxide and reduction to nitrous oxide.* FEBS Letters, 1999. **445**(2): p. 389-394.

118. Lo, F.-C., et al., *The Metal Core Structures in the Recombinant Escherichia coli Transcriptional Factor SoxR.* Chemistry (Weinheim an der Bergstrasse, Germany), 2012. **18**: p. 2565-2577.

119. Ding, H. and B. Demple, *Direct nitric oxide signal transduction via nitrosylation of iron-sulfur centers in the SoxR transcription activator.* Proceedings of the National Academy of Sciences of the United States of America, 2000. **97**: p. 5146-5150.

120. Crack, J.C., et al., *Mechanism of [4Fe-4S](Cys)4 cluster nitrosylation is*

doi:10.6342/NTU201903909

conserved among NO-responsive regulators. Journal of Biological Chemistry, 2013. **288**(16): p. 11492-11502.

121. Crack, J., et al., *Iron-sulfur cluster sensor-regulators.* Current Opinion in Chemical Biology, 2012. **16**: p. 35-44.

122. Zhang, B., et al., *Reversible cycling between cysteine persulfide-ligated [2Fe-2S] and cysteine-ligated [4Fe-4S] clusters in the FNR regulatory protein.* Proceedings of the National Academy of Sciences of the United States of America, 2012. **109**: p. 15734-15739.

123. Corker, H. and R.K. Poole, *Nitric oxide formation by Escherichia coli. Dependence on nitrite reductase, the NO-sensing regulator Fnr, and flavohemoglobin Hmp.* Journal of Biological Chemistry, 2003. **278**(34): p. 31584-31592.

124. Tsou, C.-C., T.-T. Lu, and W.-F. Liaw, *EPR, UV−Vis, IR, and X-ray Demonstration of the Anionic Dimeric Dinitrosyl Iron Complex [(NO)$_2$Fe(μ-StBu)$_2$Fe(NO)$_2$]$^-$: Relevance to the Products of Nitrosylation of Cytosolic and Mitochondrial Aconitases, and High-Potential Iron Proteins.* Journal of the American Chemical Society, 2007. **129**(42): p. 12626-12627.

125. Lu, T.-T., et al., *Anionic Roussin's Red Esters (RREs) syn-/anti-[Fe(μ-SEt)(NO)$_2$]$^{2-}$: the Critical Role of Thiolate Ligands in Regulating the Transformation of RREs into Dinitrosyl Iron Complexes and the Anionic RREs.* Inorganic Chemistry, 2008. **47**(13): p. 6040-6050.

126. Boese, M., et al., *S-nitrosation of serum albumin by dinitrosyl-iron complex.* Journal of Biological Chemistry, 1995. **270**(49): p. 29244-29249.

127. Helland, R., et al., *An Oxidized Tryptophan Facilitates Copper Binding in Methylococcus capsulatus-secreted Protein MopE.* Journal of Biological

doi:10.6342/NTU201903909

Chemistry, 2008. **283**(20): p. 13897-13904.

128. Miyaji, A., M. Nitta, and T. Baba, *Influence of copper ions removal from membrane-bound form of particulate methane monooxygenase from Methylosinus trichosporium OB3b on its activity for methane hydroxylation.* Journal of Biotechnology: X, 2019. **1**: p. 100001.

doi:10.6342/NTU201903909

APPENDIX

Tables

Table S1. Cu^{II} EPR intensities measured for the full-length MBP-PmoB and the *N*-truncated MBPPmoB$_{33\text{-}414}$ and MBP-PmoB$_{55\text{-}414}$ proteins.

Sample	**MBP-PmoB**	**MBP-PmoB$_{33\text{-}414}$**	**MBP-PmoB$_{55\text{-}414}$**
Total coppers	**15 µmoles** **(10.95 coppers/protein)**	**10 µmoles** **(9.54 coppers/protein)**	**10 µmoles** **(9.03 coppers/protein)**
Effects of titration with $Fe(CN)_6^{3-}$			
0 equiv.	0.025 Cu^{II} (0.23%)	4.48 Cu^{II} (47%)	n.d.
1 equiv.	0.027 Cu^{II} (0.25%)	3.62 Cu^{II} (38%)	n.d.
3 equiv.	n.d.	--	9.9×10^{-3} Cu^{II} (0.11%)
5 equiv.	0.049 Cu^{II} (0.45%)	5.44 Cu^{II} (57%)	0.018 Cu^{II} (0.2%)
10 equiv.	0.022 Cu^{II} (0.2%)	5.72 Cu^{II} (60%)	n.d.

n.d.: not detected.

Table S2. The distribution of His, Met, Asp, and Glu in the different subunits of pMMO.

	PmoA	**PmoB**	**PmoC**
Histidine	H 11, 38, 40, 168, 232	H 33, 48, 72, 137, 139, 192, 307	H 105, 131, 144, 202, 216
Methionine	M 1, 24, 42, 45, 136, 150, 176, 178, 199, 223, 239	M 1, 42, 44, 93, 141, 142, 163, 218, 237, 249, 251, 269, 272, 298, 300, 414	M 1, 61, 190, 207, 230
Aspartate	D 22, 47, 49, 53, 56, 132, 182, 211	D 6, 51, 82, 85, 123, 135, 179, 220, 225, 232, 288, 326, 328, 332, 339, 344, 350, 363, 368, 378, 382, 384, 394, 406	D 18, 50, 87, 127, 137, 139, 254
Glutamate	E 13, 81, 100, 172, 195, 201, 241	E 35, 57, 63, 75, 79, 83, 102, 117, 160, 165, 181, 185, 226, 276, 287, 316, 338, 343, 358, 372	E 13, 40, 55, 57, 67, 71, 97, 98, 125, 147, 199, 208, 209, 251, 255

[a] Residues are color-coded according their locations *vis a vis* the membrane: *N*-terminal sub-domain (*blue*); transmembrane domain (*red*); and *C*-terminal sub-domain (*green*).

Table S3. Fitting of the k^3-weighted EXAFS data for the fully reduced MBP-PmoB$_{1\text{-}414}$, PmoB$_{33\text{-}414}$, PmoB$_{55\text{-}414}$ and PmoB$_{55\text{-}414}$ Y374F proteins enriched in the cytoplasmic membranes of *E. coli* K12 TB1 cells. Errors are estimated to be 25% for coordination numbers and 0.01–0.03 Å for distances. Parameters used in the fitting include: *C.N.*, the coordination number; *R* (Å), the distance relative to Cu; σ^2 (Å^2), the Debye-Waller factor; and R_{fit} (%), the goodness-of-fit parameter. Fitting ranges for *k* space (Å^{-1}) and *R* space (Å) are indicated by Δk and ΔR, respectively.

	Fits		Cu–O/N	Cu–S	Cu–Cu	Δk (Å^{-1})	ΔR (Å)	R_{fit} (%)
PmoB$_{1\text{-}414}$	Fit 1	*C.N.* × *R* (Å) σ^2 (Å^2)	3 ×2.10 Å 0.003			2.0–11.5 Å^{-1}	1.38–3.27 Å	4.5
	Fit 2	*C.N.* × *R* (Å) σ^2 (Å^2)	3 ×2.03 Å 0.004	1 ×2.35 Å 0.004		2.0–11.5 Å^{-1}	1.83–2.58 Å	0.15
	Fit 3	*C.N.* × *R* (Å) σ^2 (Å^2)	2 ×2.08 Å 0.005	1 ×2.30 Å 0.001	0.3 ×2.70 Å 0.0007	2.0–10.7 Å^{-1}	1.34–3.19 Å	0.11
PmoB$_{33\text{-}414}$	Fit 4	*C.N.* × *R* (Å) σ^2 (Å^2)	3 ×2.11 Å 0.002			1.70–11.9 Å^{-1}	1.57–3.05 Å	3.53
	Fit 5	*C.N.* × *R* (Å) σ^2 (Å^2)	3 ×2.05 Å 0.006	1 ×2.31 Å 0.002		1.69–12.2 Å^{-1}	1.64–3.03 Å	1.42
	Fit 6	*C.N.* × *R* (Å) σ^2 (Å^2)	3 ×2.06 Å 0.009	1 ×2.30 Å 0.003	0.4 ×2.64 Å 0.008	1.69–12.2 Å^{-1}	1.64–3.05 Å	0.99
PmoB$_{55\text{-}414}$	Fit 7	*C.N.* × *R* (Å) σ^2 (Å^2)	3 ×2.11 Å 0.004			1.67–10.7 Å^{-1}	1.13–3.18 Å	1.52
	Fit 8	*C.N.* × *R* (Å) σ^2 (Å^2)	3 ×2.03 Å 0.005	1 ×2.37 Å 0.001		1.67–10.7 Å^{-1}	1.13–3.18 Å	1.64
	Fit 9	*C.N.* × *R* (Å) σ^2 (Å^2)	2 ×2.05 Å 0.002	1 ×2.37 Å 0.007		2.0–10.7 Å^{-1}	1.11–3.58 Å	0.29
	Fit 10	C.N. × *R* (Å) σ^2 (Å^2)	2 ×2.04 Å 0.003	1 ×2.37 Å 0.006	0.15 ×2.73 Å 0.005	2.0–10.7 Å^{-1}	1.11–3.58 Å	0.25
	Fit 11	*C.N.* × *R* (Å) σ^2 (Å^2)	3 ×2.09 Å 0.001			1.97–10.9 Å^{-1}	1.74–2.56 Å	1.99

doi:10.6342/NTU201903909

PmoB$_{33\text{-}414}$ Y374F	Fit 12	*C.N.* × *R* (Å) σ^2 (Å^2)	2 ×2.05 Å 0.001	1 ×2.37 Å 0.007		2.0–10.7 Å^{-1}	1.27–3.05 Å	1.20
	Fit 13	*C.N.* × *R* (Å) σ^2 (Å^2)	2 ×2.05 Å 0.003	1 ×2.36 Å 0.005	0.3 ×2.95 Å 0.003	2.1–10.9 Å^{-1}	1.27–3.05 Å	2.14

Table S4. Fitting of the k^3-weighted EXAFS data with the mononuclear copper site (**A** site) and dinuclear copper center (**B** site) from the crystal structure included as a structural model for the MBP-PmoB$_{33\text{-}414}$ proteins enriched in the cytoplasmic membranes of *E. coli* K12 TB1 cells after exposure to the air for 24 h at 4°C. Errors are estimated to be 25% for coordination numbers and 0.01–0.03 Å for distances. Parameters used in the fitting include: *C.N.*, the coordination number; *R* (Å), the distance relative to Cu; σ^2 (Å^2), the Debye-Waller factor; and R_{fit} (%), the goodness-of-fit parameter. Fitting ranges for *k* space (Å^{-1}) and *R* space (Å) are indicated by Δk and ΔR, respectively.

	Fits		Cu–O/N	Cu–S	Cu-C	Cu–Cu	Cu–C/N	Δk (Å^{-1})	ΔR (Å)	R_{fit} (%)
PmoB $_{33\text{-}414}$ oxidiz-ed form	Fit 14	*C.N.* × *R*(Å) σ^2 (Å^2)	3.0 ×1.97 Å 0.004	1.0 ×2.26 Å 0.012		0.8 ×2.79 Å 0.010		2.9–12.2 Å^{-1}	1.24–3.65 Å	0.48
	Fit 15	*C.N.* × *R*(Å) σ^2 (Å^2)	3.0 ×1.96 Å 0.004	1.0 ×2.28 Å 0.020	3.0×3.21 Å 0.001	1.0×2.86 Å 0.008	3.0×3.93 Å 0.003	2.9–12.2 Å^{-1}	1.24–4.65 Å	0.18
	Fit 16	*C.N.* × *R*(Å) σ^2 (Å^2)	3.0 ×1.95 Å 0.002	1.0 ×2.49 Å 0.009	3.0×2.91 Å 0.006			2.9–12.2 Å^{-1}	1.17–3.71 Å	0.52
	Fit 17	*C.N.* × *R*(Å) σ^2 (Å^2)	3.0×1.97 Å 0.003	1.0 ×2.29 Å 0.004	2.0×2.41 Å 0.003	1.0×2.92 Å 0.012	3.0×3.92 Å 0.003	2.9–12.2 Å^{-1}	1.17–4.74 Å	0.12
	Fit 18	*C.N.* × *R*(Å) σ^2 (Å^2)	4.0×1.97 Å 0.009		3.0×2.30 Å 0.009	1.0×3.13 Å 0.010	3.0×3.91 Å 0.003	2.9–12.2 Å^{-1}	1.17–4.74 Å	0.33

doi:10.6342/NTU201903909

Table S5. Specific activities of the *E. coli* membranes with the various expressed MBP-PmoB proteins toward methane and propene oxidation at 45 °C using duroquinol as the reductant.

	Methanol[a]	Propylene Oxide[b]	Acrolein[c]
MBP-PmoB$_{33-414}$ (0 mM[d])	n.d.[f]	n.d.	269±218
MBP-PmoB$_{33-414}$ (1 mM[e])	n.d.	n.d.	133±79
MBP-PmoB$_{55-414}$ (0 mM)	n.d.	n.d.	1001±125
MBP-PmoB$_{55-414}$ (1 mM)	n.d.	n.d.	956±164

[a,b,c] The specific activities (μmol/μmol protein·min) measured for the conversion of methane into methanol, propylene into propylene oxide and propylene into acrolein, respectively. [d,e] The recombinant PmoB variants were grown in *E. coli* K12 TB1 cells with either 0 or 1 mM CuCl$_2$. [f] n.d.: not detected.

ft corrected Fourier transforms of the Cu EXAFS (*red* circles) and the corresponding best fits (*black* solid lines) All the parameters used in the data fitting are provided in Table S4.

doi:10.6342/NTU201903909

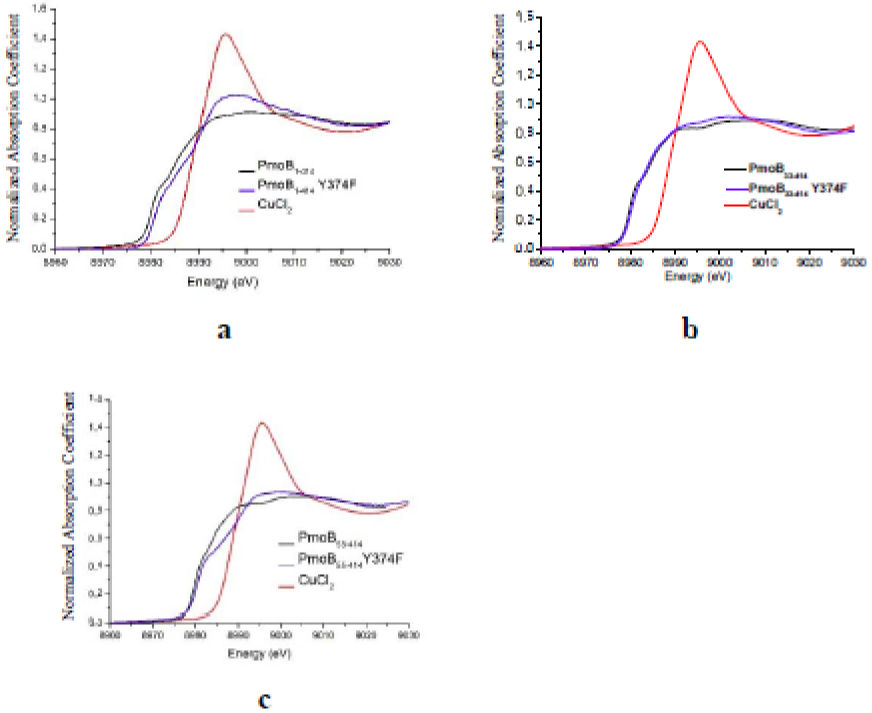

a

b

c

Fig. S2. Comparison of the X-ray absorption spectra of the Cu ions in the membranes of the *E. coil* cells with the various expressed MBP-PmoB proteins and their Y374F mutants: a, the full-length MBP-PmoB; b, the MBP-PmoB$_{33\text{-}414}$ protein; c, the MBP-PmoB$_{55\text{-}414}$ protein.

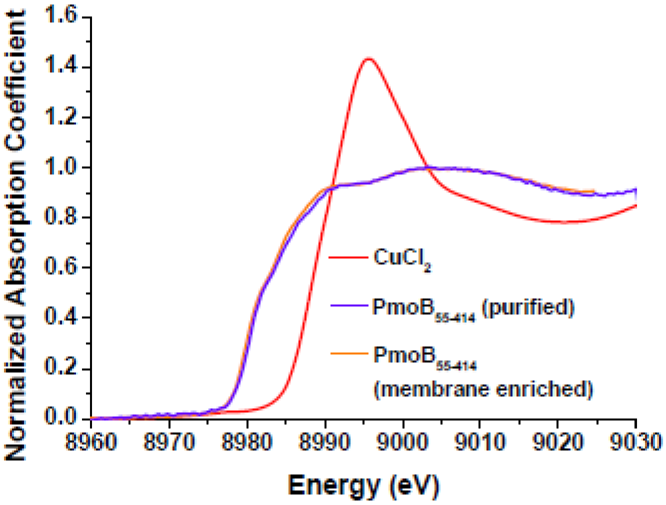

Fig. S3. The effects of purification by detergent solubilization and affinity chromatography on the Cu K-edge of the MBP-PmoB$_{55\text{-}414}$ protein.

(a) EXAFS Fit 1, MBP-PmoB$_{1\text{-}414}$

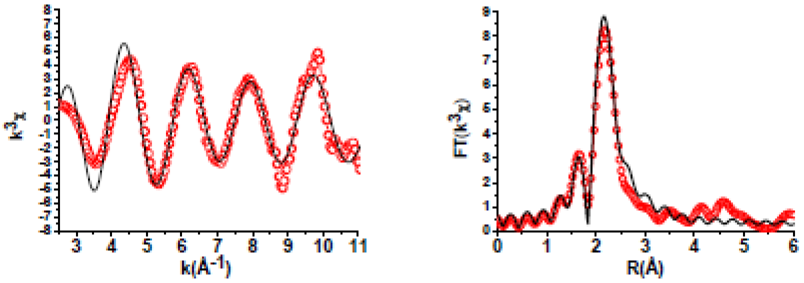

(b) EXAFS Fit 2, MBP-PmoB$_{1\text{-}414}$

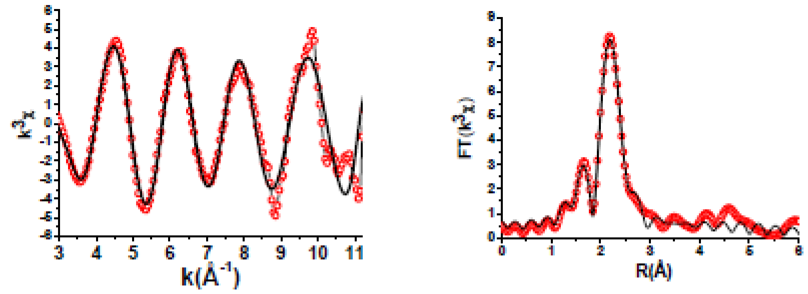

(c) EXAFS Fit 4, MBP-PmoB$_{33\text{-}414}$

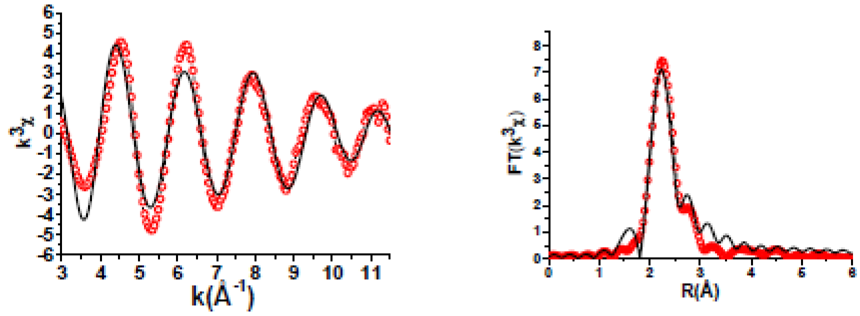

(a) EXAFS Fit 14

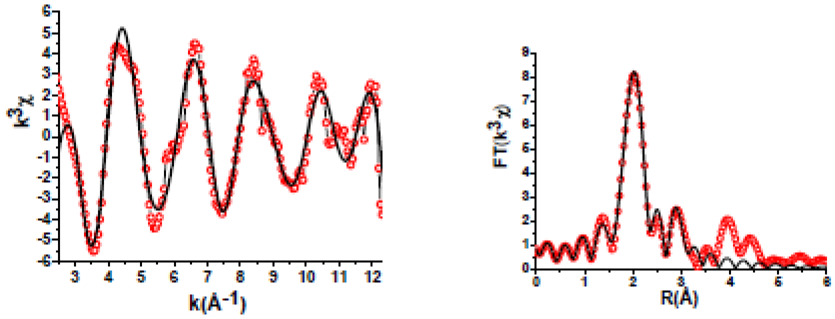

(b) EXAFS Fit 16

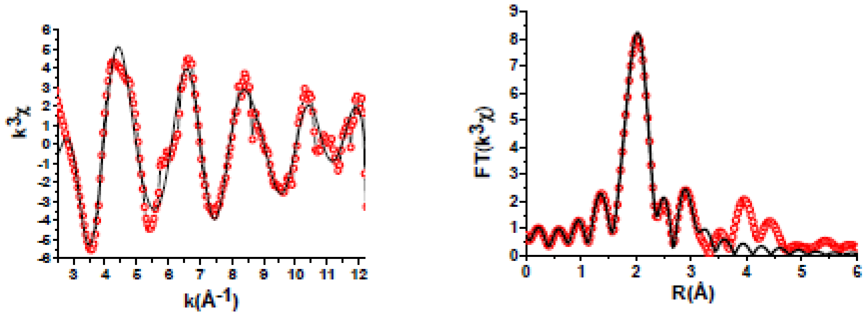

Fig. S5. (a) and (b): Two additional fits to the Cu EXAFS for the oxidized MBP-PmoB$_{33\text{-}414}$ protein enriched in the cytoplasmic membranes of *E. coli* K12 TB1 cells with the mononuclear copper site (A site) and the dicopper center (B site) from the X-ray crystal structure of pMMO included as a structural model. Cu–S (Met), Cu–C$_\alpha$ (His) and/or Cu–Cu back-scatterings are also included. *Left*: Cu EXAFS (*red* circles) and the corresponding best fits (*black* solid lines); *Right*: Phase shift corrected Fourier transforms of the Cu EXAFS (*red* circles) and the corresponding best fits (*black* solid lines) All the parameters used in the data fitting are provided in Table S4.

doi:10.6342/NTU201903909

(g) EXAFS Fit 9, MBP-PmoB$_{55\text{-}414}$

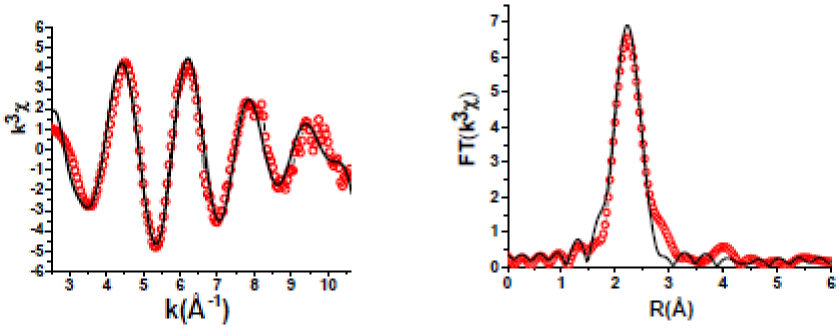

(h) EXAFS Fit 11, MBP-PmoB$_{33\text{-}414}$ Y374F

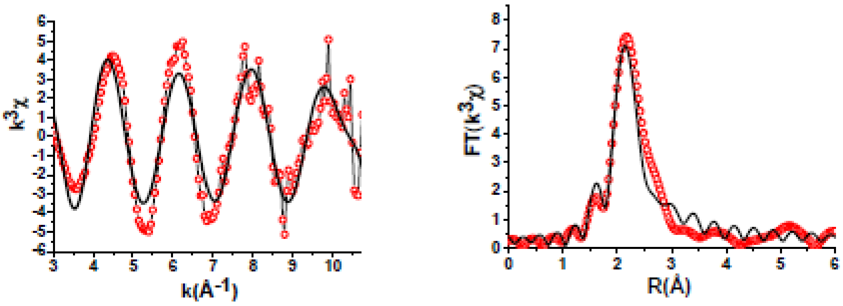

(i) EXAFS Fit 12, MBP-PmoB$_{33\text{-}414}$ Y374F

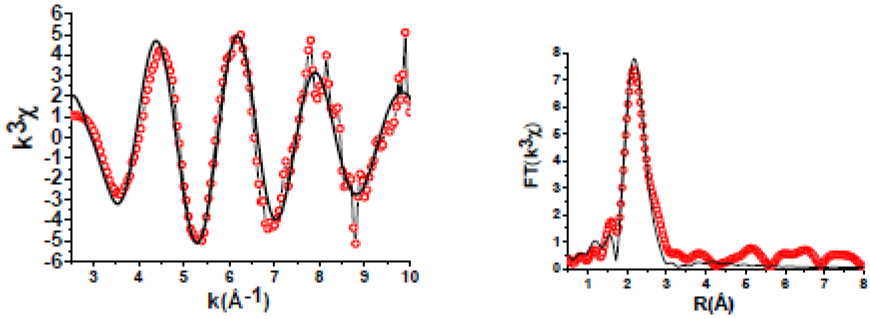

Fig. S4. (a)-(i): The Cu EXAFS and their Fourier transforms of the fully reduced MBP-PmoB$_{1\text{-}414}$, PmoB$_{33\text{-}414}$, PmoB$_{55\text{-}414}$ and PmoB$_{55\text{-}414}$ Y374F enriched in the cytoplasmic membranes of *E. coli* K12 TB1 cells. *Left*: Cu EXAFS (*red* circles) and the corresponding best fits (*black* solid lines); *Right*: Phase shift corrected Fourier transforms of Cu EXAFS (*red* circles) and the corresponding best fits (*black* solid lines). All the parameters used in the data fitting are provided in Table S3.

(d) EXAFS Fit 5, MBP-PmoB$_{33\text{-}414}$

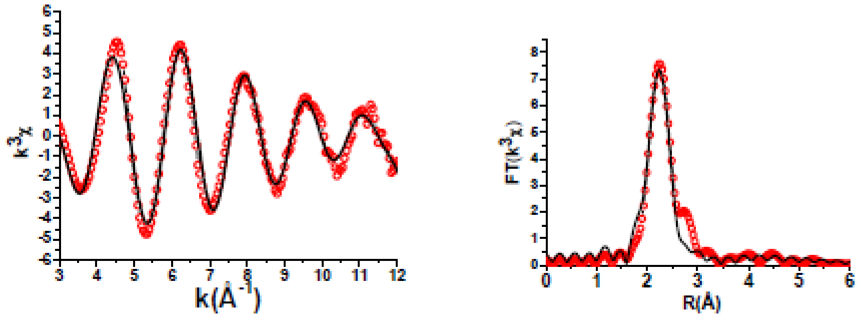

(e) EXAFS Fit 7, MBP-PmoB$_{55\text{-}414}$

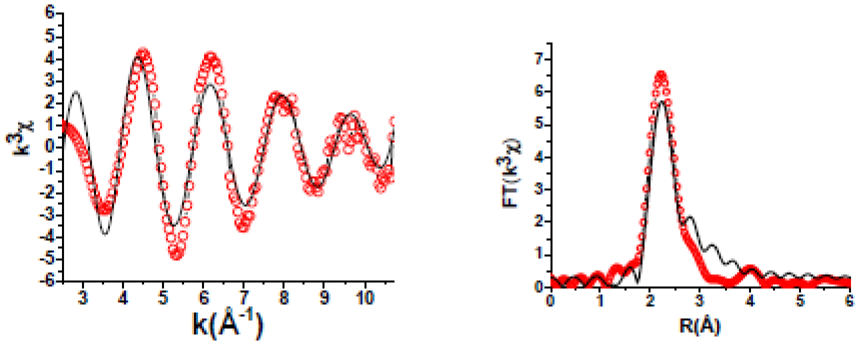

(f) EXAFS Fit 8, MBP-PmoB$_{55\text{-}414}$

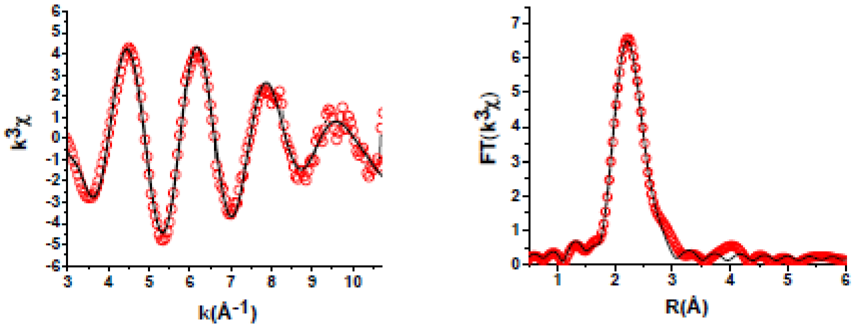

Mascot Search Results of pyruvate formate lyase

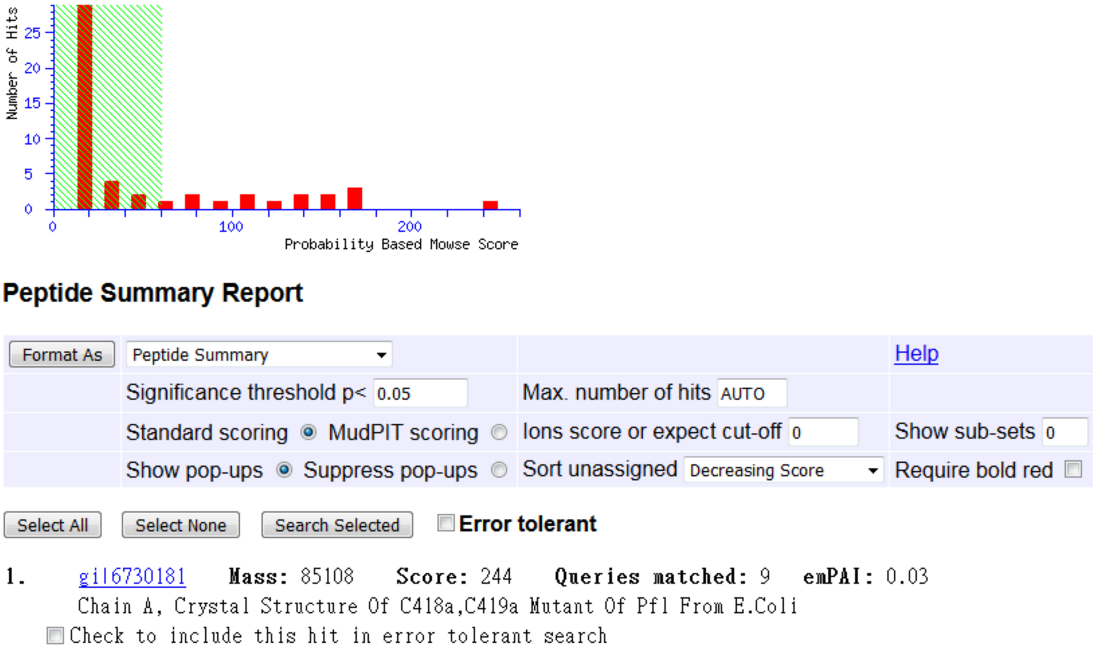

Peptide Summary Report

Format As: Peptide Summary
Significance threshold p< 0.05
Max. number of hits AUTO
Standard scoring ● MudPIT scoring ○
Ions score or expect cut-off 0
Show sub-sets 0
Show pop-ups ● Suppress pop-ups ○
Sort unassigned Decreasing Score
Require bold red ☐

☐ **Error tolerant**

1. gi|6730181 **Mass:** 85108 **Score:** 244 **Queries matched:** 9 **emPAI:** 0.03
Chain A, Crystal Structure Of C418a,C419a Mutant Of Pfl From E.Coli
☐ Check to include this hit in error tolerant search

Mascot Search Results of pyruvate kinase II

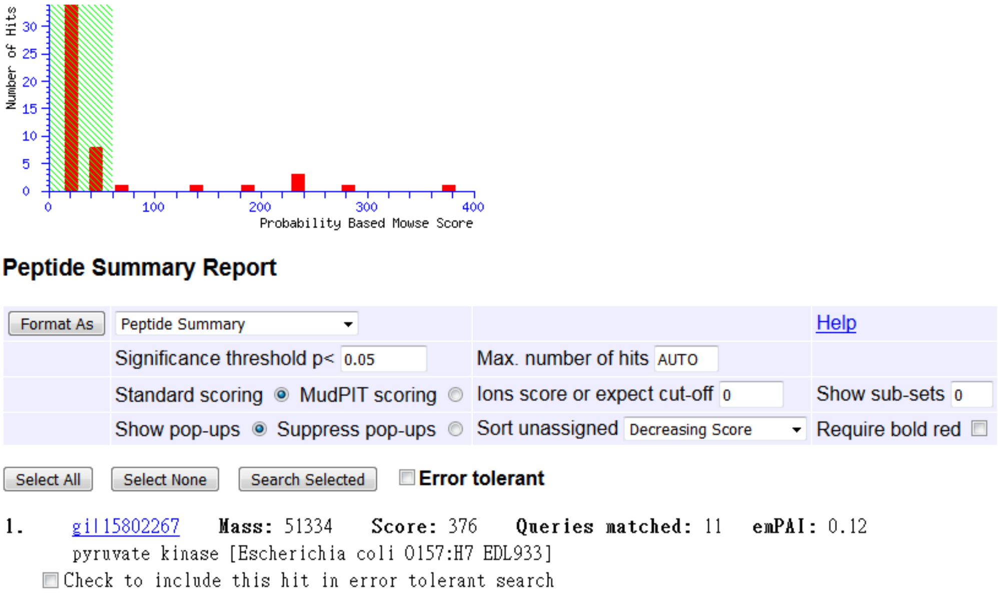

Peptide Summary Report

Format As: Peptide Summary
Significance threshold p< 0.05
Max. number of hits AUTO
Standard scoring ● MudPIT scoring ○
Ions score or expect cut-off 0
Show sub-sets 0
Show pop-ups ● Suppress pop-ups ○
Sort unassigned Decreasing Score
Require bold red ☐

☐ **Error tolerant**

1. gi|15802267 **Mass:** 51334 **Score:** 376 **Queries matched:** 11 **emPAI:** 0.12
pyruvate kinase [Escherichia coli O157:H7 EDL933]
☐ Check to include this hit in error tolerant search

doi:10.6342/NTU201903909

Mascot Search Results of H+ ATPase F1 alpha subunit

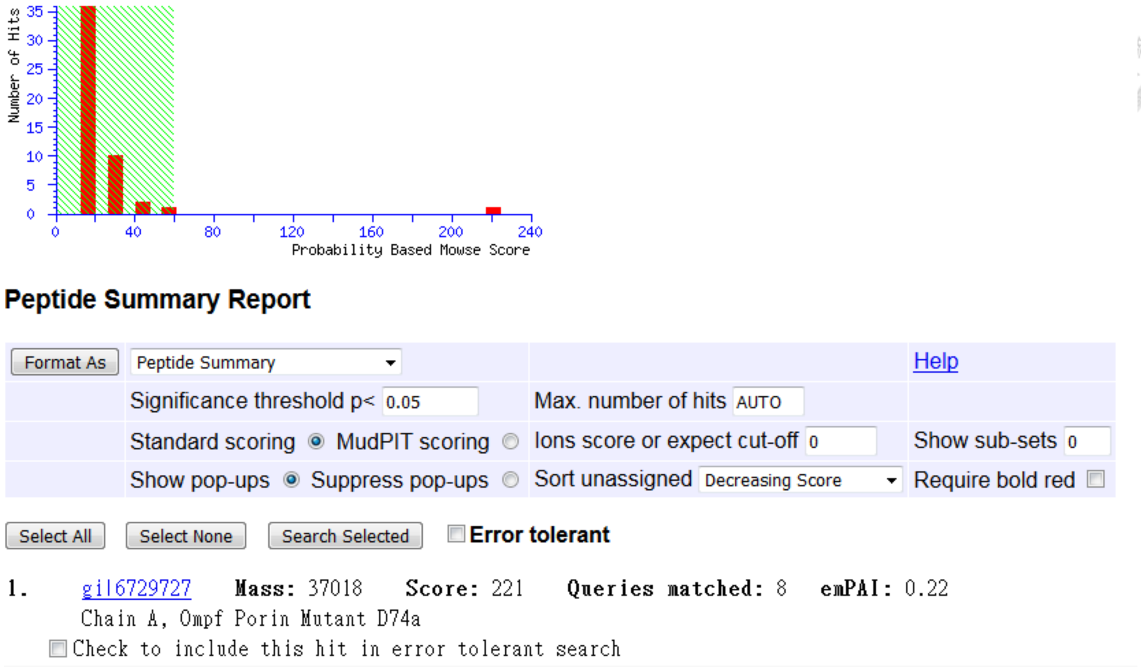

Peptide Summary Report

Format As: Peptide Summary

Significance threshold p< 0.05

Max. number of hits AUTO

● Standard scoring ○ MudPIT scoring

Ions score or expect cut-off 0

Show sub-sets 0

● Show pop-ups ○ Suppress pop-ups

Sort unassigned Decreasing Score

Require bold red ☐

☐ **Error tolerant**

1. gi|6729727 **Mass:** 37018 **Score:** 221 **Queries matched:** 8 **emPAI:** 0.22
Chain A, Ompf Porin Mutant D74a
☐ Check to include this hit in error tolerant search

Mascot Search Results of MalE

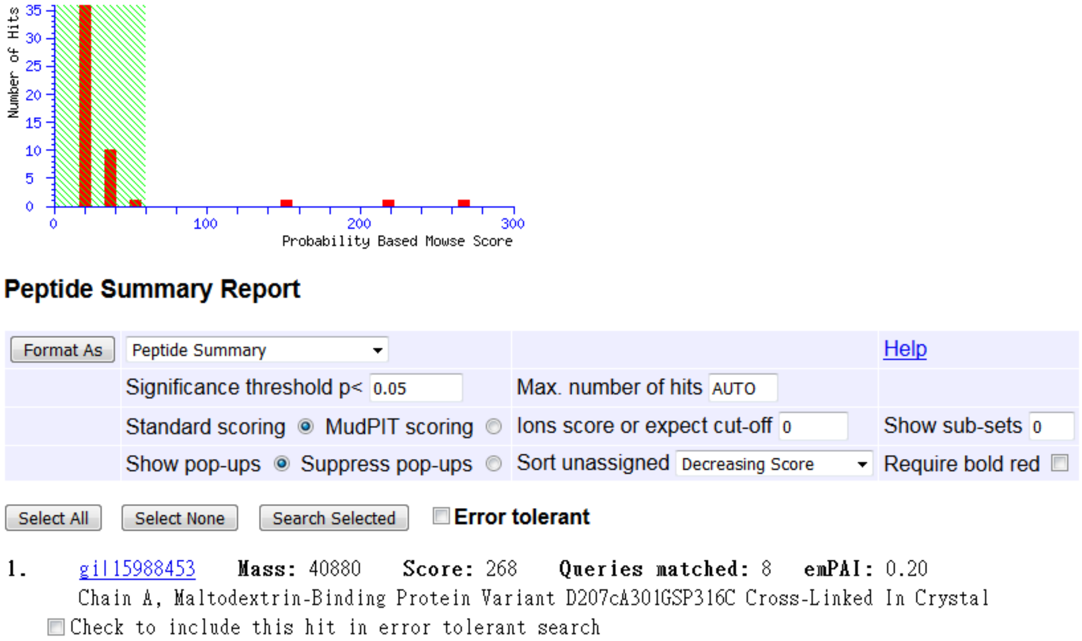

Peptide Summary Report

Format As: Peptide Summary

Significance threshold p< 0.05

Max. number of hits AUTO

● Standard scoring ○ MudPIT scoring

Ions score or expect cut-off 0

Show sub-sets 0

● Show pop-ups ○ Suppress pop-ups

Sort unassigned Decreasing Score

Require bold red ☐

☐ **Error tolerant**

1. gi|15988453 **Mass:** 40880 **Score:** 268 **Queries matched:** 8 **emPAI:** 0.20
Chain A, Maltodextrin-Binding Protein Variant D207cA301GSP316C Cross-Linked In Crystal
☐ Check to include this hit in error tolerant search

doi:10.6342/NTU201903909

Mascot Search Results of FNR(ox), FNRhistag(nitrate), FNR(nitrate)

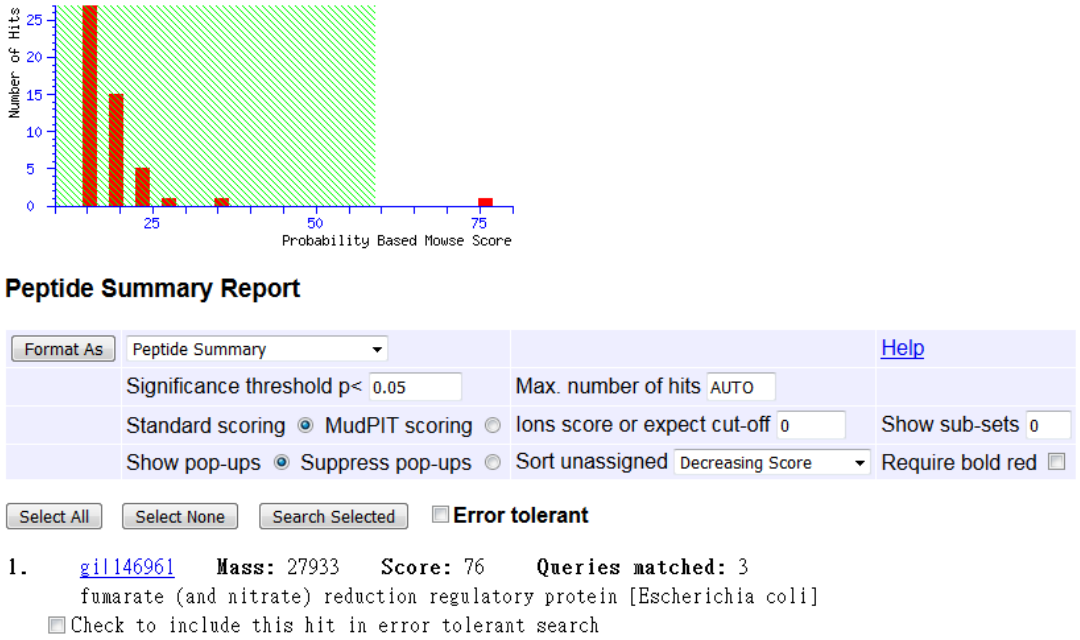

Peptide Summary Report

Format As: Peptide Summary

Help

Significance threshold p< 0.05

Max. number of hits AUTO

Standard scoring ● MudPIT scoring ○

Ions score or expect cut-off 0

Show sub-sets 0

Show pop-ups ● Suppress pop-ups ○

Sort unassigned Decreasing Score

Require bold red ☐

☐ **Error tolerant**

1. gi|146961 **Mass:** 27933 **Score:** 76 **Queries matched:** 3
fumarate (and nitrate) reduction regulatory protein [Escherichia coli]
☐ Check to include this hit in error tolerant search

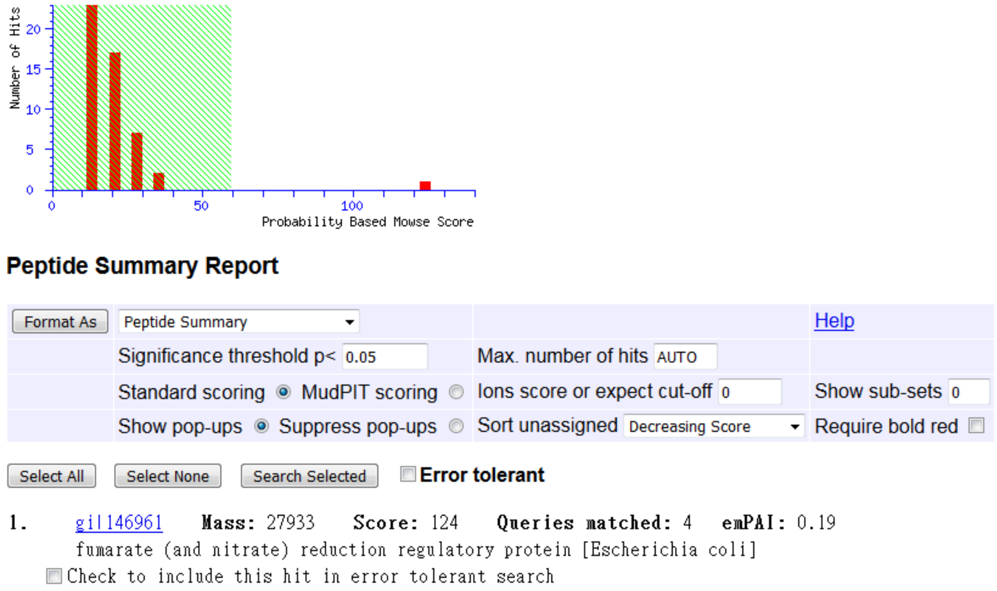

Peptide Summary Report

Format As: Peptide Summary

Help

Significance threshold p< 0.05

Max. number of hits AUTO

Standard scoring ● MudPIT scoring ○

Ions score or expect cut-off 0

Show sub-sets 0

Show pop-ups ● Suppress pop-ups ○

Sort unassigned Decreasing Score

Require bold red ☐

☐ **Error tolerant**

1. gi|146961 **Mass:** 27933 **Score:** 124 **Queries matched:** 4 **emPAI:** 0.19
fumarate (and nitrate) reduction regulatory protein [Escherichia coli]
☐ Check to include this hit in error tolerant search

doi:10.6342/NTU201903909

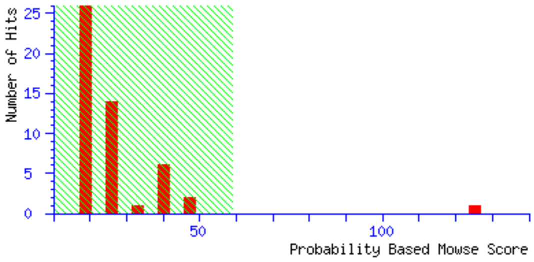

Peptide Summary Report

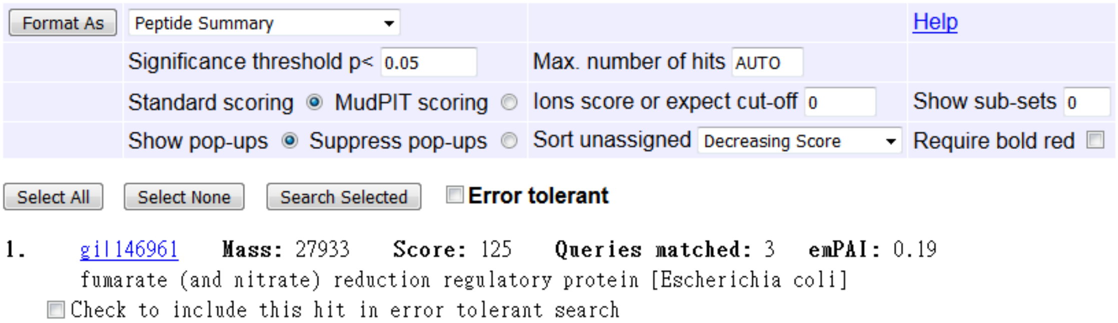

Format As: Peptide Summary

Significance threshold p< 0.05

Max. number of hits AUTO

Standard scoring ● MudPIT scoring ○

Ions score or expect cut-off 0

Show sub-sets 0

Show pop-ups ● Suppress pop-ups ○

Sort unassigned Decreasing Score

Require bold red ☐

☐ **Error tolerant**

1. gi|146961 **Mass:** 27933 **Score:** 125 **Queries matched:** 3 **emPAI:** 0.19
fumarate (and nitrate) reduction regulatory protein [Escherichia coli]
☐ Check to include this hit in error tolerant search

doi:10.6342/NTU201903909